Doctoral Dissertation
博士論文

Study of solar chromospheric heating mechanism with numerical simulation
(太陽彩層加熱メカニズムの数値的研究)

A Dissertation Submitted for the Degree of Doctor of Philosophy

December 2020

令和 2 年 12 月博士(理学)申請

Department of Earth and Planetary Science, Graduate School of Science,

The University of Tokyo

東京大学大学院理学系研究科

地球惑星科学専攻

Wang Yikang

王怡康

Contents

Abstract

The chromosphere is the intermediate layer between the photosphere and the corona, characterized by a drastic change of pressure, density, and plasma beta. Magnetic field protruded from the network region forms flux tubes. As the height increases, the flux tube expands and merges with adjacent tubes in the chromosphere, separating the chromosphere into two regions, which are the low-beta region in the flux tube and the high-beta region below the magnetic canopy.

The energy balance in the chromosphere is dominated by mechanical heating and radiative loss. What is the heating source is still under debate, especially in the low-beta chromosphere. Waves, reconnection, and dissipation of small structures are the main candidates for the chromospheric heating problem. We mainly focus on the wave heating mechanism since there is plenty of observational supporting evidence.

Previous researches provide different wave heating scenarios and comparison among them is necessary. However, it is difficult as the previous theoretical works usually use the artificial model that can include only one or a few mechanisms. On the other hand, previous studies using realistic simulations usually focus on synthesized observation without investigating the detailed physics about the heating mechanisms or the propagation of waves.

This study aims to investigate the propagation of MHD waves in realistic simulations and quantitatively determine the role of different wave modes in chromospheric heating.

We perform two-dimensional and three-dimensional realistic MHD simulations from the convection zone to the corona with local thermodynamic equilibrium radiative transfer in the photosphere and approximated chromospheric and coronal radiative loss. From the simulation results, we identify the shocks by filtering the regions with large negative divergence of velocity. After identification of shocks, we separate fast and slow MHD waves by identifying the relation between magnetic pressure and gas pressure in the upstream and the downstream regions. We further calculate the contribution to chromospheric heating through the measurement of entropy jump. The methods including basic equations of the simulation, shock identification, and heating rate calculation are introduced in detail in Chapter 2.

In Chapter 3, we show the results of the two-dimensional simulation. It is found that the shock heating rate is consistent with the radiative cooling rate. Fast magnetic waves play an important role in heating the low-beta chromosphere. Low-beta fast magnetic waves are generated by mode conversion from fast acoustic waves in the high-beta region. We also estimate the potential heating rate from ambipolar diffusion. The result shows that, on average, ambipolar diffusion does not considerably heat the chromosphere.

In Chapter 4, we validate our main conclusion that the fast magnetic wave is significant in heating the low-beta chromosphere by three-dimensional simulation. It is expected that the percentage of the heating contributed from fast magnetic waves could be overestimated in the two-dimensional simulation since Alfvén wave vanishes. We confirm that fast magnetic wave heating is significant in a substantial range of the chromosphere even in the three-dimensional geometry. On the other hand, the difference from the two-dimensional simulation is that the slow wave becomes dominant in heating at a higher position. This is interpreted as a consequence of the magnetic structure.

The most important new results of our study are that (1) we study the propagation of waves in detail by identification of different modes of waves and calculate the shock

heating rate in realistic simulation, and (2) we propose that the fast magnetic wave makes a significant contribution to chromospheric heating.

Acknowledgments

I would express my deepest gratitude to my supervisor Dr. Yokoyama, T. for his careful instruction and kindly encouragement. I admire his characteristics as an extraordinary researcher and educator.

Many thanks to all the members of solar and astronomical plasma laboratory. Iijima, H., Kaneko, T., Wang, S., Kono, S., Shoda, M., Oi, Y., Ichimura, C., Bekki, Y., Mineta, R., Kai, T., Zhou, X., and Kuniyoshi, H.. It is my honor to join this laboratory. Wish you all the best for your future. Special thanks to Iijima, H.. I have benefited a lot from discussing with him.

My study in Japan has been supported by Japanese Government (Monbukagakusho: MEXT) Scholarship. Numerical computations were carried out on Cray XC50 at Center for Computational Astrophysics, National Astronomical Observatory of Japan, and Oakforest-PACS Supercomputer System at The University of Tokyo.

I shall not forget my friends, Wan, L., Luo, T., to name but a few. Thanks all of you for your support.

Thanks to my beloved partner Jiang, Y.. Words fail at the moment but I may express by action for the rest of the time.

Finally, thanks to my parents, for everything you did for me. I am so lucky to be your child.

Chapter 1

Introduction

1.1 The solar atmosphere and the chromosphere

The solar outer atmosphere is divided into three layers. Starting from the bottom, they are the photosphere, the chromosphere (Figure 1.1), and the corona. Observation of different layers is shown in Figure 1.2. Most of the visible light originates from the photosphere. It is the densest part of the solar atmosphere characterized by ubiquitous convection motion with a scale length of 1 Mm that could be observed by white light continuum (upper-left panel in Figure 1.2). The corona is the highest part of the solar atmosphere, characterized by the hot plasma where the temperature could reach 1 MK (lower-right panel in Figure 1.2). The chromosphere is the intermediate layer between the photosphere and the corona. There is another thin region between the chromosphere and the corona. This thin region is called the transition region where the density and temperature change drastically.

The chromosphere cannot be seen in the white light of the visible band due to a strong backlight from the bright photosphere. Without assists of instruments, it could only be observed during a total solar eclipse as a spherical layer of reddish color resulted from Hα emission. The reddish color is also the origin of the word “chromosphere”, which means

"sphere of color" literally.

The thickness of the chromosphere is only a few Mm which is two orders thinner than the solar radius. The pressure scale height is around 150 km, which is one order thinner than the thickness of the chromosphere. The VALC model (model C in Vernazza et al., 1981) is one of the standard semi-empirical models of the solar atmosphere obtained by solving the radiative transfer equation in hydrostatic equilibrium atmosphere. This model is built by adjusting the distribution of physical parameters to minimize the difference between the observed extreme ultraviolet (EUV) spectra and the synthesized one. The VALC model thus provides the distribution of physical parameters in the one-dimensional plane-parallel atmosphere. It shows that the density and gas pressure have more than 5 orders difference between the bottom and the top of the chromosphere, leading to the drastic change of plasma beta and the increase of non-linearity of the waves. Moreover, the treating of chromospheric radiation is also complicated due to the non-local thermodynamic equilibrium (NLTE) effect. The radiative loss is the dominant term in energy loss (Withbroe & Noyes, 1977, also see section 1.2) process of the chromosphere.

The chromosphere is highly dynamic. Photospheric convection provides kinetic and magnetic energy, generating waves that propagate ubiquitously in the chromosphere (Lighthill, 1952). Waves could be observed by the Doppler shift of the chromospheric lines (e.g. Morton et al., 2012) and swing motions of the chromospheric plasma (e.g. McIntosh et al., 2011). Waves could also be indicated by the dynamic jet structures (see the review paper by Sterling, 2000). Figure 1.3 shows an example of observations of chromospheric waves. The N-shape perturbation of the spectra profiles is interpreted as a train of shock waves. Waves in the chromosphere also drive the up and down motion of the transition region, which relates to the generation of spicules (Roberts, 1945; Osterbrock, 1961).

The structure of the magnetic field in the chromosphere is inhomogeneous which is

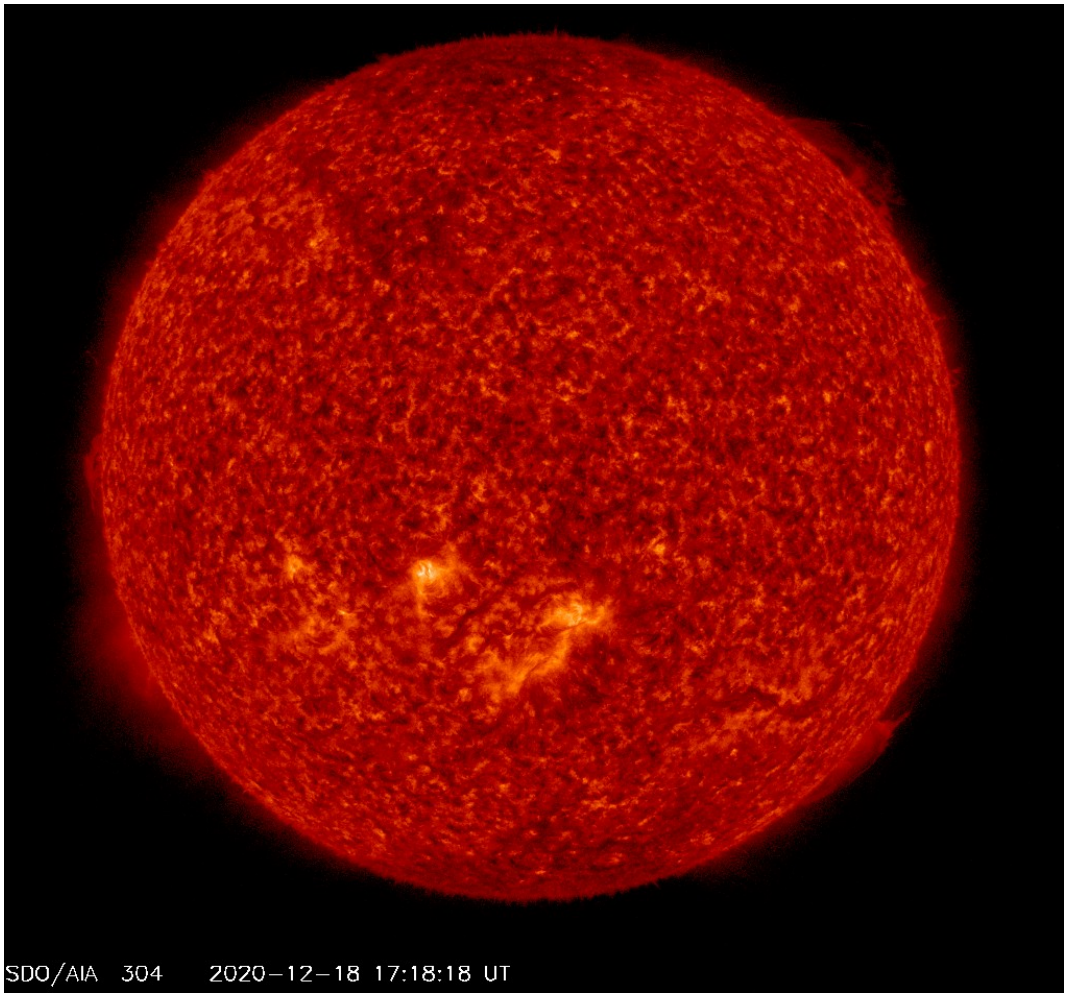

Figure 1.1: Full disk observation of the band 304 Å of the Atmospheric Imaging Assembly (AIA; Lemen et al., 2012) on board Solar Dynamics Observatory (SDO; Pesnell et al., 2012). Credit: NASA.

characterized by the expansion of the magnetic flux tubes. Photospheric convection motion accumulates magnetic flux. Figure 1.4 shows that strong magnetic field appears at the boundary of the supergranulation patterns. The accumulated enhanced magnetic fields become the foot point of flux tubes where the magnetic field intensity could reach more than 1000 G. The structure of a network can also be seen by the increased intensity in chromospheric lines (see the lower-left panel of Figure 1.2). Figure 1.5 shows the cartoon that demonstrates the structure of the magnetic field in the solar atmosphere. As the height increases, the flux tube also expands and merges with adjacent tubes in the chromosphere (Bellot Rubio & Orozco Suárez, 2019), providing a link from the photosphere

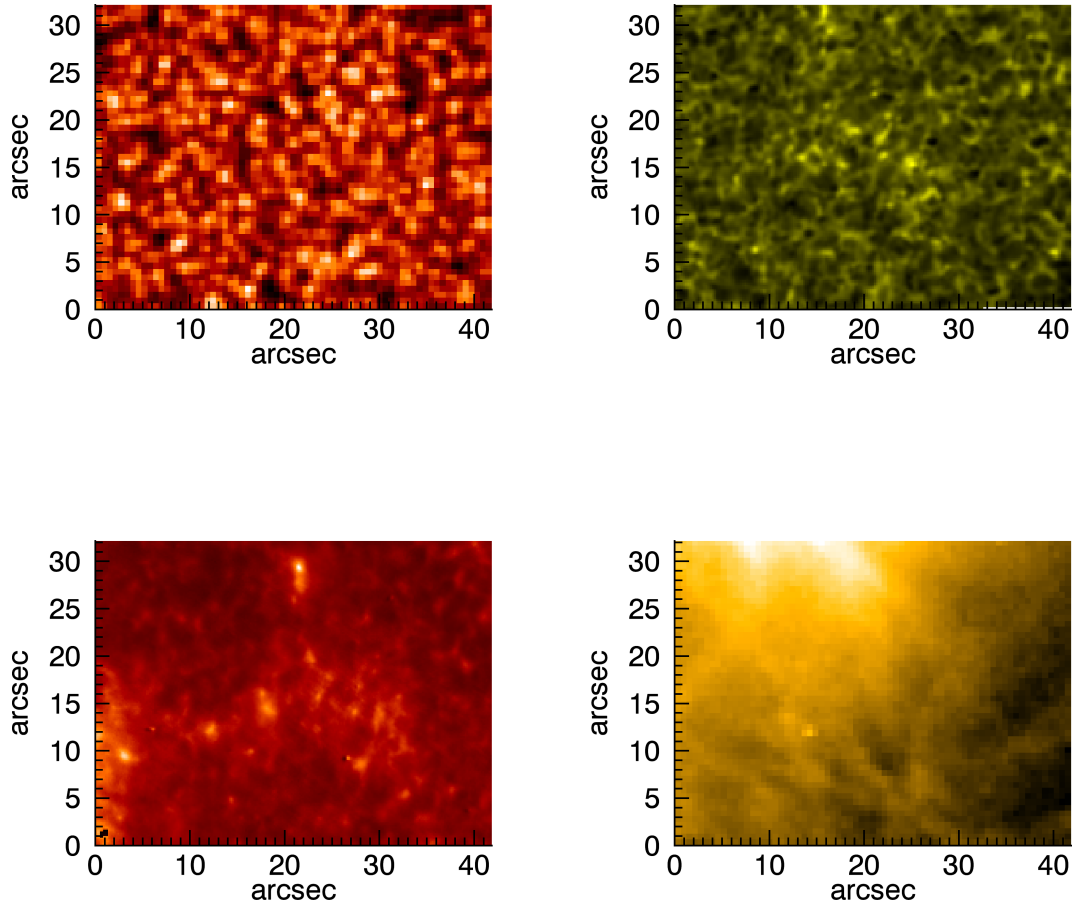

Figure 1.2: Observation of a quiet sun region near disk center on Sep 25, 2013, from different wavelengths. Upper-left: White light continuum observation of the photosphere observed by Helioseismic and Magnetic Imager (HMI; Scherrer et al., 2012). The photosphere is characterized by convection motion which has a typical scale of 1 Mm. Upper-right: Ca II H line observation of the lower chromosphere by Solar Optical Telescope (SOT; Tsuneta et al., 2008) onboard Hinode (Kosugi et al., 2007). Lower-left: Mg h line observation of the higher chromosphere and the transition region by Interface Region Imaging Spectrograph (IRIS; De Pontieu et al., 2014). Bright structures in the upper-right and this panel indicate the network region. Lower-right: EUV Observation of high-temperature plasma in the corona by AIA 171 Å on board SDO. Note that strong radiation from the top of this panel comes from a nearby active region.

to the chromosphere and the corona. The space that is not occupied by expanded flux tubes located at the lower part of the chromosphere below the closed magnetic field lines is called canopy regions (Gabriel, 1976).

The semi-empirical model (Vernazza et al., 1981) shows the temperature distribution in Figure 1.6, together with the approximated formation height of characteristic lines.

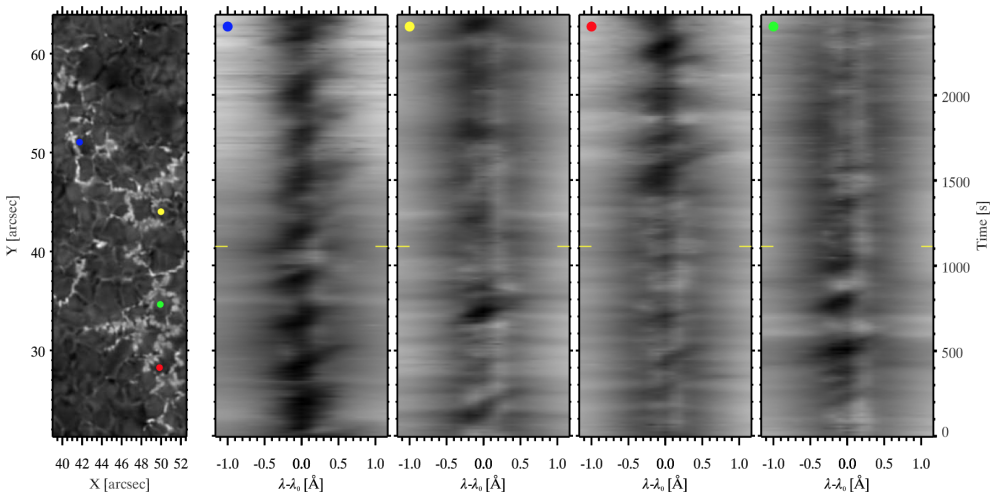

Figure 1.3: The temporal evolution of Ca 854.2 nm profiles at locations indicated with color markers in the left most panel. The second panel from the left corresponds to a typical absorption profile showing a shock-induced temporal pattern. The last three panels correspond to the time evolution of three raised-core profiles. The time of the image in the left panel is indicated in the time slices with short yellow lines. Modified from de la Cruz Rodríguez et al. (2013).

This temperature distribution can not be explained by a pure thermodynamic process which indicates that mechanical heating is required in the chromosphere. Without mechanical heating, the temperature will drop down to a level that is well below the semi-empirical model (Figure 1.7). It is known that the energy balance in the chromosphere is dominated by the balance between radiative loss and mechanical heating (Ulmschneider & Kalkofen, 2003). However, what is the source of heating in the chromosphere remains unclear. The chromospheric heating problem is one of the most important problems in solar physics.

1.2 Chromospheric radiative loss

The well-known VALC model shows that the radiative loss rate in the chromosphere is around 4.9×10^9 erg s^{-1} g^{-1} (Anderson & Athay, 1989b). This value is usually used as a simplification of the chromospheric radiative loss rate (e.g. Matsumoto & Shibata, 2010).

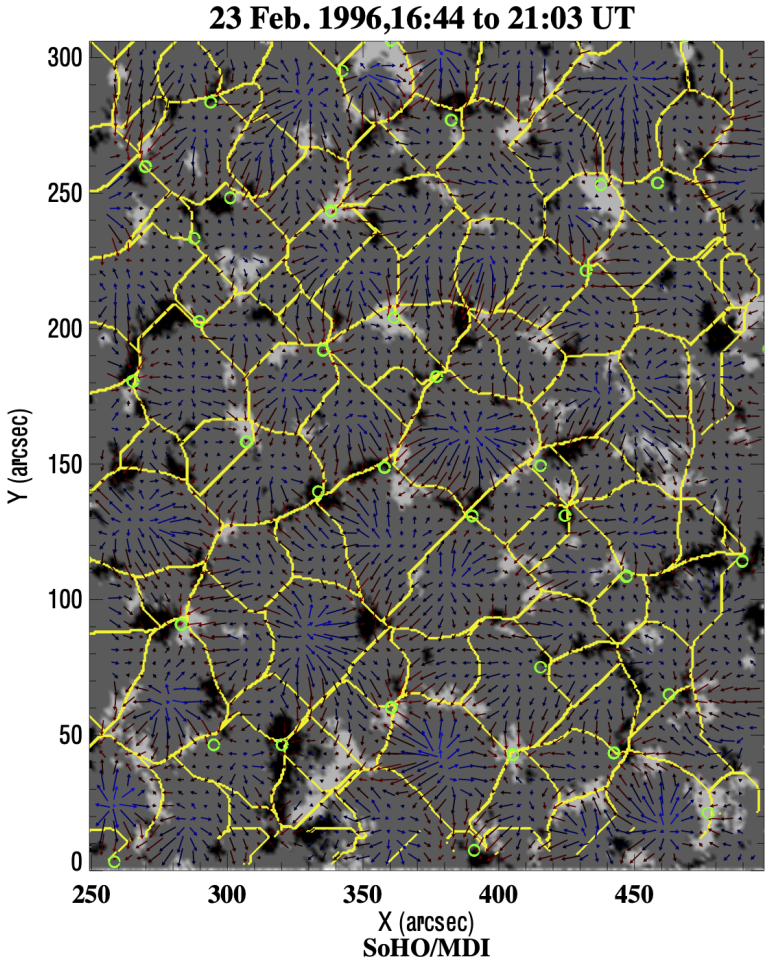

Figure 1.4: Magnetogram observed by the Michelson Doppler Imager (MDI; Scherrer et al., 1995) on board Solar and Heliospheric Observatory (SOHO; Domingo et al., 1995). The boundary of the supergranule cells is marked in yellow lines. Arrows indicate the supergranular flow pattern. Modified from Figure 1 of Tsiropoula et al. (2012).

We estimate the timescale of the radiative loss by $t_{\rm loss} = e_{\rm m}/Q_{\rm E}$, where $e_{\rm m}$ is the internal energy per unit mass. $Q_{\rm E}$ is the empirical value of chromospheric radiative loss rate mentioned above, $Q_{\rm E} = 4.9 \times 10^9$ erg s^{-1} g^{-1}. By taking $e_{\rm m} = \frac{1}{\rho}\frac{3}{2}nk_{\rm B}T$, we obtain the result that $t_{\rm loss} \sim 100$ s where n is number density per unit volume. $n = \rho/m_{\rm p}$. $m_{\rm p}$ is the mass of proton. $k_{\rm B}$ is the Boltzmann constant. T is the temperature. $T = 5000$ K is assumed. On the other hand, under the same assumption, the sound speed is 8.3 km/s. According to the VALC model, the height of the chromosphere is around 2 Mm. As a result, the dynamic timescale is estimated to be 240 s. This estimation shows that the dynamic timescale is in the same order as the radiative loss time scale. Consequently,

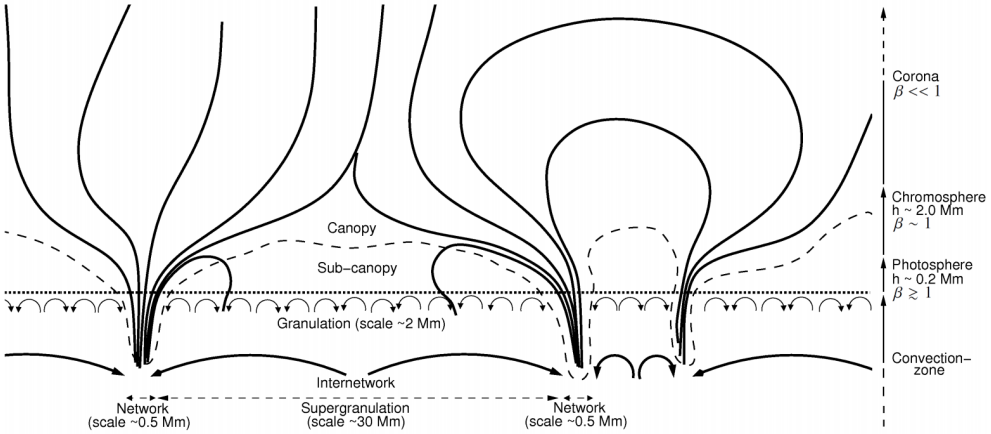

Figure 1.5: Sketch of the magnetic field structure of the quiet-sun atmosphere. Extracted from Figure 6 of Wiegelmann et al. (2014).

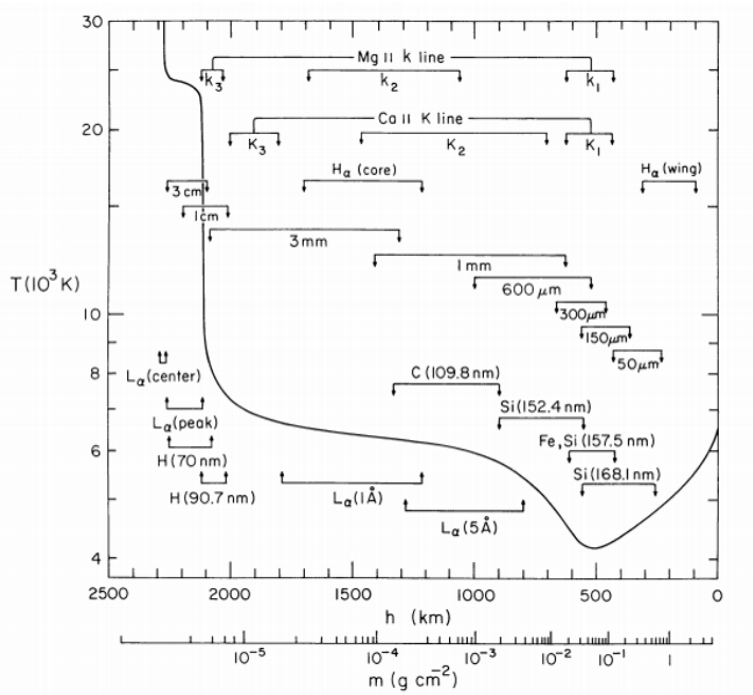

Figure 1.6: Temperature distribution of solar atmosphere derived from EUV spectra (Vernazza et al., 1981). Short bars indicate the approximated formation height of corresponding lines.

radiative loss has a significant effect on chromospheric dynamics.

The traditional treatment of radiative loss is by calculating the intensity I_ν by solving

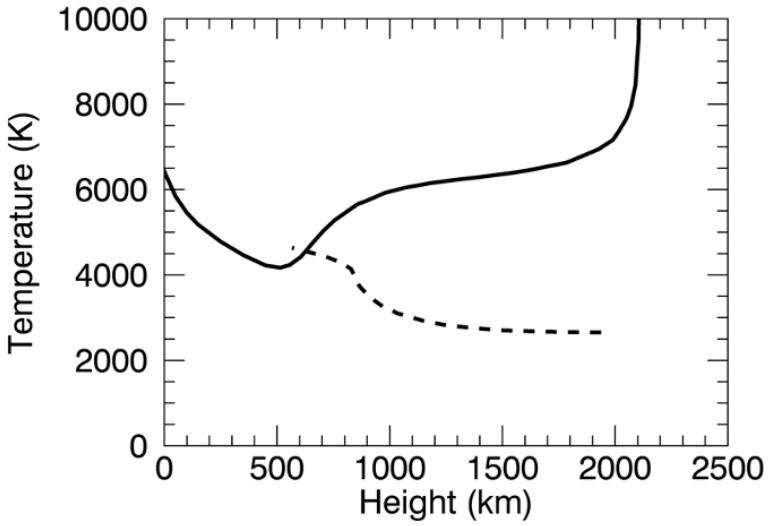

Figure 1.7: Comparison between the temperature distribution of the solar atmospheric model between the semi-empirical model VALC (solid line) and the radiative equilibrium atmosphere (dashed line). Modified from Figure 1 in Anderson & Athay (1989a).

the radiative transfer equation

$$\mathbf{n} \cdot \nabla I_\nu = j_\nu - \alpha_\nu I_\nu, \tag{1.1}$$

or

$$\mathbf{n} \cdot \nabla I_\nu = \alpha_\nu (S_\nu - I_\nu), \tag{1.2}$$

where $\mathbf{n}$ is the unit vector of direction. j_ν is the emission rate. α_ν is the absorption coefficient. S_ν is the source function which is defined as $S_\nu = j_\nu/\alpha_\nu$. I_ν, S_ν, j_ν, and α_ν are all functions of position, frequency, and direction. Subscript ν indicates the monochromatic radiation with frequency ν. The radiative energy flux $\mathbf{F}_\nu$ is

$$\mathbf{F}_\nu = \int_{4\pi} \mathbf{n} I_\nu \mathrm{d}\mathbf{\Omega}, \tag{1.3}$$

where $\mathbf{\Omega}$ is the solid angle. After the radiative energy flux is obtained, the radiative heating rate is

$$Q_{\mathrm{rad},\nu} = -\nabla \cdot \mathbf{F}_\nu. \tag{1.4}$$

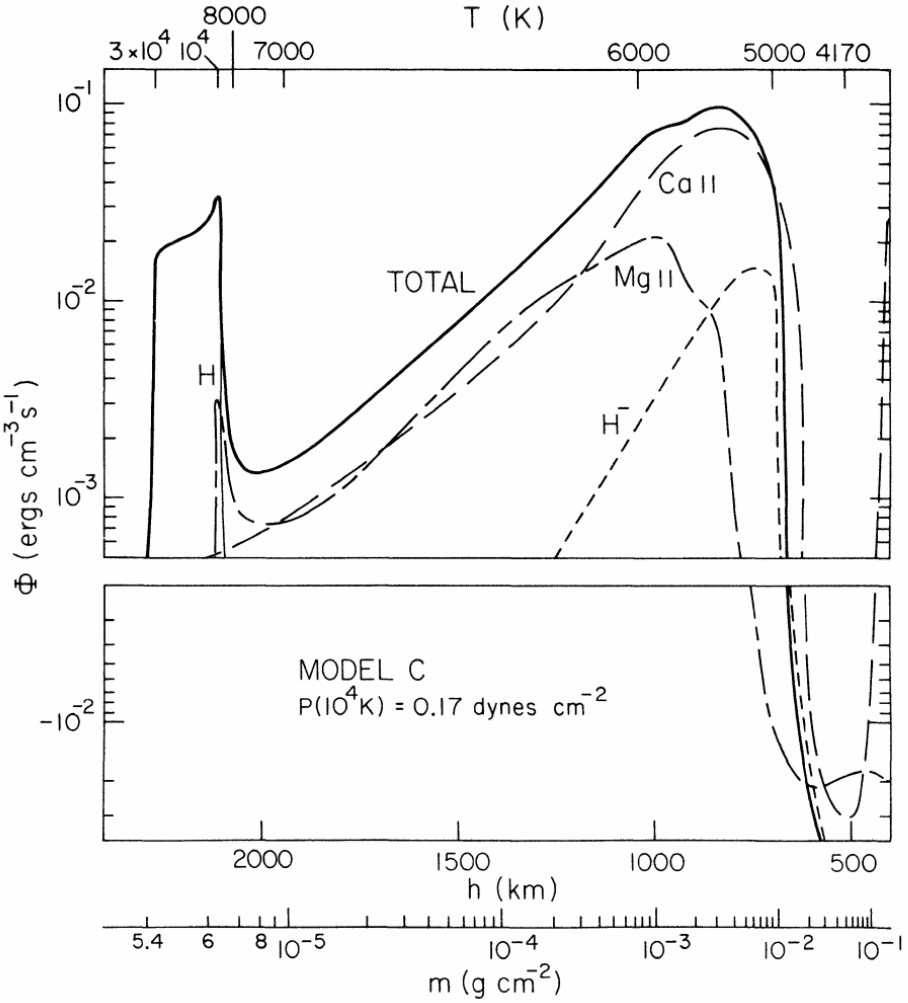

Figure 1.8: Distribution of radiative loss of Mg II lines, Ca II lines, and Hydrogen. Extracted from Figure 12 in Avrett (1981).

Further calculation shows that,

$$
\begin{aligned}
Q_{\text{rad},\nu} &= -\nabla \cdot \mathbf{F}_\nu \\
&= -\nabla \cdot \int_{4\pi} \mathbf{n} I_\nu \mathrm{d}\mathbf{\Omega} \\
&= -\int_{4\pi} \mathbf{n} \cdot \nabla I_\nu \mathrm{d}\mathbf{\Omega} \\
&= -\int_{4\pi} (j_\nu - \alpha_\nu I_\nu) \mathrm{d}\mathbf{\Omega} \\
&= 4\pi\alpha_\nu (J_\nu - S_\nu),
\end{aligned}
\tag{1.5}
$$

where J_ν is the direction-averaged intensity that

$$J_\nu = \frac{1}{4\pi}\int_{4\pi} I_\nu \mathrm{d}\mathbf{\Omega}. \tag{1.6}$$

In practice, the radiative loss rate for a specific emission line is required and an integral on frequency that covers the line profile is necessary. If we consider a specific transition of frequency ν_0 and assuming a simple two-level atom model then the emission rate and absorption rate are

$$j_\nu = \frac{h\nu}{4\pi}(N_U A_{\mathrm{UL}}\psi), \tag{1.7}$$

$$\alpha_\nu = \frac{h\nu}{4\pi}(N_L B_{\mathrm{LU}}\phi - N_U B_{\mathrm{UL}}\chi), \tag{1.8}$$

where N_U is the number density of electrons in the upper level. N_L is the number density of electrons in the lower level. A and B are the Einstein coefficients. L is the lower energy lever. U is the upper energy level. The subscribe UL stands for de-excitation process and LU stands for the excitation process. h is Planck constant. ψ, χ, and ϕ are functions of frequency and direction. They relate with frequency and angular distribution of photons, which reflect a combination of multiple effects such as Doppler shift and macroturbulence. For simplicity, we apply the assumption of complete redistribution (CRD) that $\psi = \chi = \phi$ in this section.

For solving the radiative transfer equation, the number density on each energy level is necessary. This is determined by statistical equilibrium. In this two-level atom model, the number of downwards transitions is identical to the number of upwards transitions in unit time. As a result, we have

$$N_U A_{\mathrm{UL}} + N_U B_{\mathrm{UL}} J + N_U C_{\mathrm{UL}} = N_L B_{\mathrm{LU}} J + N_L C_{\mathrm{LU}}, \tag{1.9}$$

where C_{LU} and C_{UL} denote the collisional coefficient. J is the direction-averaged intensity

(Equation 1.6) integrated on frequency that covers the line profile.

Combining Equation (1.7), (1.8) and (1.2), as well as the following standard relation between Einstein coefficients and collisional coefficients,

$$A_{\mathrm{UL}}/B_{\mathrm{UL}} = \frac{2h\nu_0^3}{c^2}, \tag{1.10}$$

$$B_{\mathrm{LU}}/B_{\mathrm{UL}} = g_{\mathrm{U}}/g_{\mathrm{L}}, \tag{1.11}$$

$$C_{\mathrm{LU}}/C_{\mathrm{UL}} = \frac{g_{\mathrm{U}}}{g_{\mathrm{L}}} \exp^{\frac{-h\nu_0}{k_{\mathrm{B}}T}}, \tag{1.12}$$

leads to

$$S = (1-\epsilon_{\mathrm{p}})J + \epsilon_{\mathrm{p}} B_{\nu_0}(T), \tag{1.13}$$

where

$$\epsilon_{\mathrm{p}} = \frac{C_{\mathrm{UL}}}{A_{\mathrm{UL}} + B_{\mathrm{UL}} B_{\nu_0}(T) + C_{\mathrm{UL}}} \tag{1.14}$$

is the collisional destruction probability. $B_{\nu_0}(T)$ is the blackbody radiation at frequency ν_0 and temperature T,

$$B_{\nu_0}(T) = \frac{2h\nu_0^3}{c^2} \frac{1}{e^{\frac{h\nu_0}{k_{\mathrm{B}}T}} - 1}. \tag{1.15}$$

In the standard relation between Einstein coefficients and collisional coefficients, g is the degeneracy for specific state. c is the speed of light. It is obvious that if ϵ_{p} is close to 1 where collision dominates the transition of electrons, the Local Thermodynamic Equilibrium (LTE) approximation could be applied and under this approximation,

$$S = B_{\nu_0}(T). \tag{1.16}$$

The source function could be used to further solve the radiative transfer equation and calculate the radiative loss rate. This approximation is valid in the dense photosphere. If we consider another extreme situation in the corona, ignoring the absorption, substitute Equation (1.7) into Equation (1.1) and integral on frequency in the emission profile, then

we get the expression of radiative loss for a specific line in corona condition

$$Q_{\text{rad,cor}} = \frac{h\nu_0}{4\pi}(N_U A_{\text{UL}}). \tag{1.17}$$

N_{U} could be expressed as functions of abundance, temperature, and number density of hydrogen and electron for each transition. Moreover, the abundance is a constant for a specific element and the frequency ν_0 is also known for a specific transition. As a result, we usually sum up all the radiative loss for multiple corona lines and use the following term as the total radiative loss rate in the corona

$$L_{\text{rad,cor}} = \Lambda(T, n_{\text{e}}) n_{\text{e}} n_{\text{H}}. \tag{1.18}$$

It is also shown that Λ is not sensitive to electron density (Landi & Landini, 1999) that Λ could be treated as a function of only temperature.

Things become much complicated in the case of the chromosphere because neither the LTE approximation nor the optically thin corona condition could be applied. Typical value of ϵ_{p} could reach to less than 10^{-2} in the chromosphere (Avrett, 1965). Detailed calculation requires solving the full radiative transfer equation and the statistical balance of the number density on each energy level. This treatment is sophisticated and time-consuming but necessary for synthesizing the emerging spectral lines.

For estimation of chromospheric radiative loss, Carlsson & Leenaarts (2012) propose the method by using a similar form of Equation (1.17) but adding an extra term representing the possibility of the photon that is not re-absorbed in the chromosphere. We also use Carlsson & Leenaarts (2012) treatment as the radiative loss term in our study. Detailed information will be given in Chapter 2.

1.3 Chromospheric heating problem

1.3.1 Evaluation of chromospheric heating models

The key to answer the chromospheric heating problem is to figure out the heating mechanism. When evaluating whether a theoretical model could succeed in explaining chromospheric heating, the temperature is widely used as a criterion. However, we should be careful to compare the time-averaged temperature in the simulation with a semi-empirical model, such as the VALC model. This is because the semi-empirical VALC model is based on a hydrostatic atmosphere where the velocity is assumed to be zero. On the contrary, the actual chromosphere is highly dynamic. As pointed out by Carlsson & Stein (1994, 1995) that the averaged gas temperature in the dynamic model is lower than that in the hydrostatic equilibrium model despite that both models have similar emerging intensities. This is because high-temperature shocks make a more significant contribution to the emerging intensity. Moreover, in the dynamic chromosphere, non-equilibrium ionization also affects the distribution of temperature profile (Leenaarts et al., 2007). The most direct way to evaluate the model is to compare the synthesized emerging spectral line with the observation, such as that was done in Carlsson & Stein (1997). The line profile could provide information that comes from the formation region only. We are still a step further to explain all the emission line profiles spontaneously while sticking to a single line will lose the overall view in the energy balance between heating and cooling. To summarize, although it is difficult to validate a model comprehensively, practically, models are evaluated from at least one of the following aspects: total energy balance, temperature, heating rate, radiative loss rate, and synthesized observation. The models described in the following sections use at least one of these for evaluation.

1.3.2 Observational validation on heating mechanism

Wave heating, reconnection heating, and dissipation of small structures are the main proposed mechanisms to explain the chromospheric heating problem. Reconnection is characterized by brightening in intensity map and cancellation of magnetic flux. However, under current limitation of observational instrument, the number density of reconnection events is one order of magnitude lower to explain the global chromospheric heating (Gošić et al., 2018). Small structures could be generated by turbulence (van Ballegooijen et al., 2011) or phase mixing (Soler et al., 2019) but can not be directly observed under current conditions.

On the other hand, the propagation of waves in the chromosphere could be detected indirectly from the dynamic spicules (Tsiropoula et al., 2012; Tian et al., 2014; De Pontieu et al., 2007) or directly from spectral observation where the "N-shape" structure appears in the wavelength-time plot (see Figure 1.3).

Whether the power of waves in the chromosphere is enough for heating is still under debate. There are researches pointed out that wave power is not enough for heating the chromosphere. Fossum & Carlsson (2005) use Transition Region and Coronal Explorer (TRACE; Handy et al., 1999) observation of 1700 Å and 1600 Å bands which sample around 360 km and 430 km above the bottom of the photosphere respectively. Their observations combining with simulations suggest that the acoustic flux is only 440 W m^{-2} (or 4.4×10^5 erg s^{-1} cm^{-2} in c.g.s. unit that is commonly used in the dissertation) which is far from supporting chromospheric radiative loss (i.e. 4300 W m^{-2} or 4.3×10^6 erg s^{-1} cm^{-2}, Vernazza et al., 1981). However, this discrepancy could be due to the insufficient resolution of the instruments. Bello González et al. (2010) analyze observations by Imaging Magnetograph eXperiment (IMaX; Martínez Pillet et al., 2011) onboard Sunrise balloon-borne solar observatory of Fe I 525.02 nm line which forms around 200–300 km above the bottom of the photosphere. In their analysis, acoustic flux of around 6.5×10^6

erg s^{-1} cm^{-2} is detected which is enough for supporting chromospheric radiative loss. Sobotka et al. (2016) and Abbasvand et al. (2020a) use Interferometric Bidimensional Spectrometer (IBIS; Cavallini, 2006) observation of Ca II 854.2 nm line (covering a range of 900–1500 km) and show that radiative losses and deposited acoustic flux are spatially correlated. The ratio between deposited acoustic energy flux to radiative losses is around 30% to 50%, which increases with activity. Although the answer for whether the chromospheric heating could be solely compensated by the dissipation of waves remains an open question, a consensus that wave is a significant candidate for chromospheric heating has been reached.

Observational works are usually done by measuring the Doppler shift of spectral profiles, which corresponds to longitudinal perturbations. The waves observed are interpreted as acoustic waves. Magnetic waves are more difficult to be observed. This is partly because the direct measurement of the magnetic field perturbation in the chromosphere is difficult due to the relatively weak magnetic field intensity and the requirement of short exposure time. Therefore, it is difficult for determining the mode of waves, especially for fast magnetic waves in the low-beta region. Effort has been done in observing Alfvén waves. De Pontieu et al. (2007) detect the swing motion of chromospheric plasma with energy flux of 100 W m^{-2} (1.0×10^5 erg s^{-1} cm^{-2}). Jess et al. (2009) detect torsional motion without corresponding intensity fluctuation in the Hα band, which is interpreted as torsional Alfvén wave. The energy flux locally is 15000 W m^{-2} (1.5×10^7 erg s^{-1} cm^{-2}) or 240 W m^{-2} (2.4×10^5 erg s^{-1} cm^{-2}) globally if assuming the filling factor to be 1.6 %. The measured amplitude is 2.6 km/s at a height of around 1 Mm.

The chromosphere becomes one of the most important targets of the next generation solar observatories. Among them include European Solar Telescope (EST; Matthews et al., 2016), Daniel K. Inouye Solar Telescope (DKIST; Tritschler et al., 2015), and Chinese Giant Solar Telescope (CGST; Deng et al., 2012). Next generation solar telescopes are designed to have unprecedented time and spatial resolution to catch fine structure and

short-period dynamic process as well as equipped with high sensitivity detectors for measuring full stokes profile for detecting weak magnetic field in the chromosphere. It is hopeful that more information, especially that related to high-frequency waves and magnetic waves, could be available soon.

1.3.3 Theoretical studies on wave heating models

Acoustic wave heating models in the high-beta region

The dissipation of acoustic shocks is considered to be a candidate for chromospheric heating in the non-magnetic chromosphere from a long time ago (Schwarzschild, 1948; Anderson & Athay, 1989b; Jordan, 1993). The acoustic waves are generated by the photospheric convective motion (Lighthill, 1952). They propagate upwards and steepen to shocks due to the increase of non-linearity and finally dissipate their energy into the chromosphere. Carlsson & Stein (1995, 1997) study the dynamics of acoustic wave propagation by hydrodynamic simulations with non-local thermodynamic equilibrium (non-LTE) radiative transfer. The result shows that the synthesized emerging Ca II H line spectra are consistent with the observation (see Figure 1.9). This study is very successful in explaining the observed spectral line profile. However, it is limited by the hydrodynamic simulation that can only model the high-beta region. Moreover, it is difficult for sound waves to supply energy in a higher position of the chromosphere (Ulmschneider & Stein, 1982; Jordan, 1993), as they dissipate energy fast at a lower position. In addition, in the low-beta region, it is necessary to consider the role of the magnetic field.

Magnetohydrodynamic wave heating models

At a higher position of the chromosphere above the equipartition layer, the magnetic field plays an important role in affecting the propagation of waves. The equipartition layer

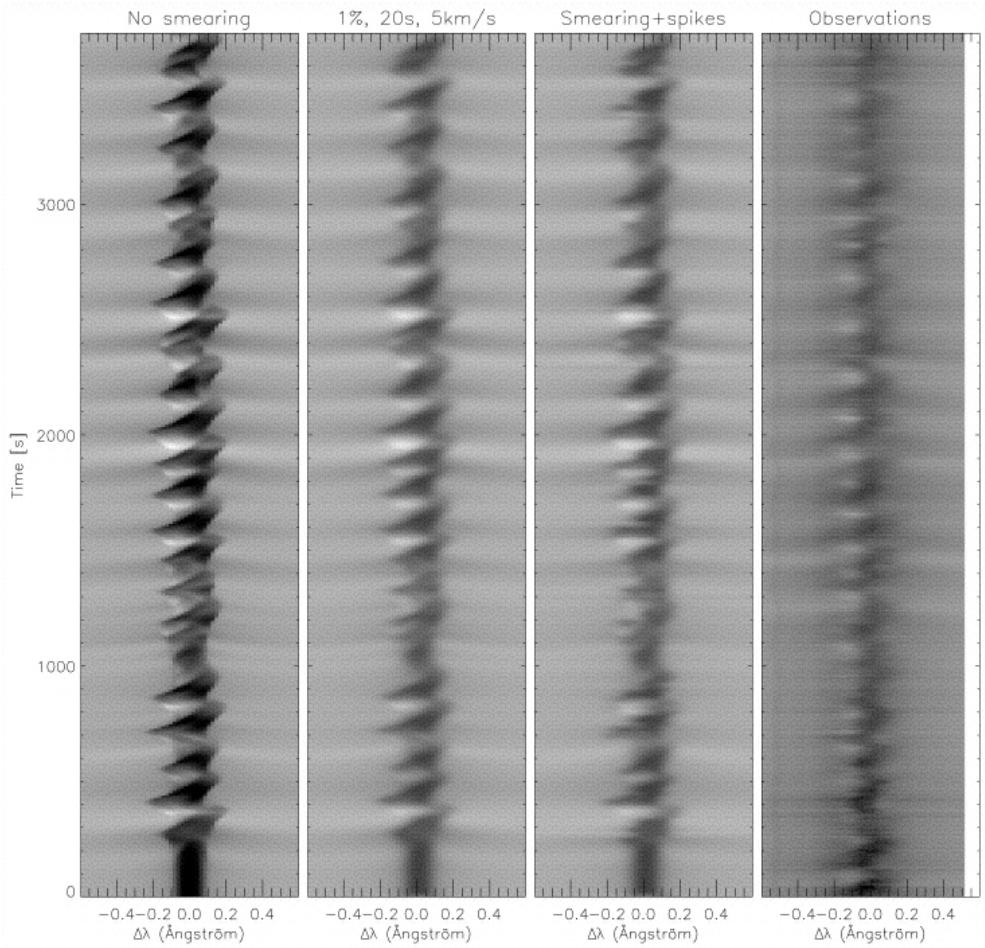

Figure 1.9: Computed Ca II H line intensity as a function of wavelength and time compared with observations. The leftmost panel shows the unsmeared results from the simulation. In the second panel, the simulation has been convolved with a Gaussian point-spread function with FWHM of 20 s in the time domain and 0.066 Å (corresponding to 5 km s^{-1}) in the wavelength domain. Scattered light amounting to 1% of the continuum intensity has been added. In the third panel, image motion has been simulated by shifting the sequence in time with a random function. The same smearing and scattered light as in the second panel are also added. The rightmost panel shows the result from observation. Extracted from Figure 18 in Carlsson & Stein (1997).

is the layer where the sound speed ($C_{\rm s}$) is identical to Alfvén speed ($C_{\rm A}$). The height of the equipartition layer in the quiet region is 0.8–1.6 Mm (Wiegelmann et al., 2014). As a comparison, the VALC model shows that the height of the top boundary of the chromosphere is 2.25 Mm. A large part of the chromosphere belongs to the low-beta region.

There are three types of magnetohydrodynamic (MHD) waves, Alfvén wave, fast

magnetoacoustic wave (hereinafter fast wave), and slow magnetoacoustic waves (hereinafter slow wave). One of the difficulties in the MHD wave study is that the mode of waves changes during its propagation. Linear mode conversion (Cally, 2006; Pennicott & Cally, 2019) occurs at the equipartition layer, leading to the conversion of wave modes, which changes its nature between acoustic and magnetic but preserves the character as fast or slow wave. For example, fast acoustic waves in the high-beta region could convert to fast magnetic wave in the low-beta region. The mode conversion coefficient (Cally, 2006, 2009) is

$$C = 1 - \exp(-\pi k h_s \sin^2 \alpha), \tag{1.19}$$

where k is the wave vector, $k = |\mathbf{k}|$; α is the attacking angle, which is the angle between the wave vector and the magnetic field; h_s is the width of the equipartition layer, $h_s = (\mathrm{d}(C_\mathrm{A}^2/C_\mathrm{s}^2)/\mathrm{d}l)^{-1}$ with C_A the Alfvén speed, C_s the sound speed, and l the distance along the direction of the wave vector. If $\alpha = 0$ then the conversion rate is zero. On the other hand, a larger attacking angle will result in efficient mode conversion. If the wave propagates in the direction perpendicular to the magnetic field (or large attacking angle), the simultaneous compression of plasma together with magnetic field leads to the generation of fast wave. A demonstration by using a toy model is shown in Figure 1.10. It is shown that conversion from fast acoustic wave to fast magnetic wave occurs at a large attacking angle while the transmission from fast acoustic wave to slow acoustic wave occurs at a smaller attacking angle. In case of non-linear waves, Pennicott & Cally (2019) point out that incident fast acoustic shocks should be constructed from high-order Fourier modes that essentially perfectly converted to fast magnetic waves for a larger attacking angle (i.e. 60 degrees). The slow acoustic waves generated from mode transmission are considered to be a candidate for heating the low-beta chromosphere (Hasan & van Ballegooijen, 2008). However, the role of fast magnetic wave in heating the low-beta chromosphere has not been investigated yet.

The non-linear mode coupling effect could generate acoustic wave from Alfvén wave

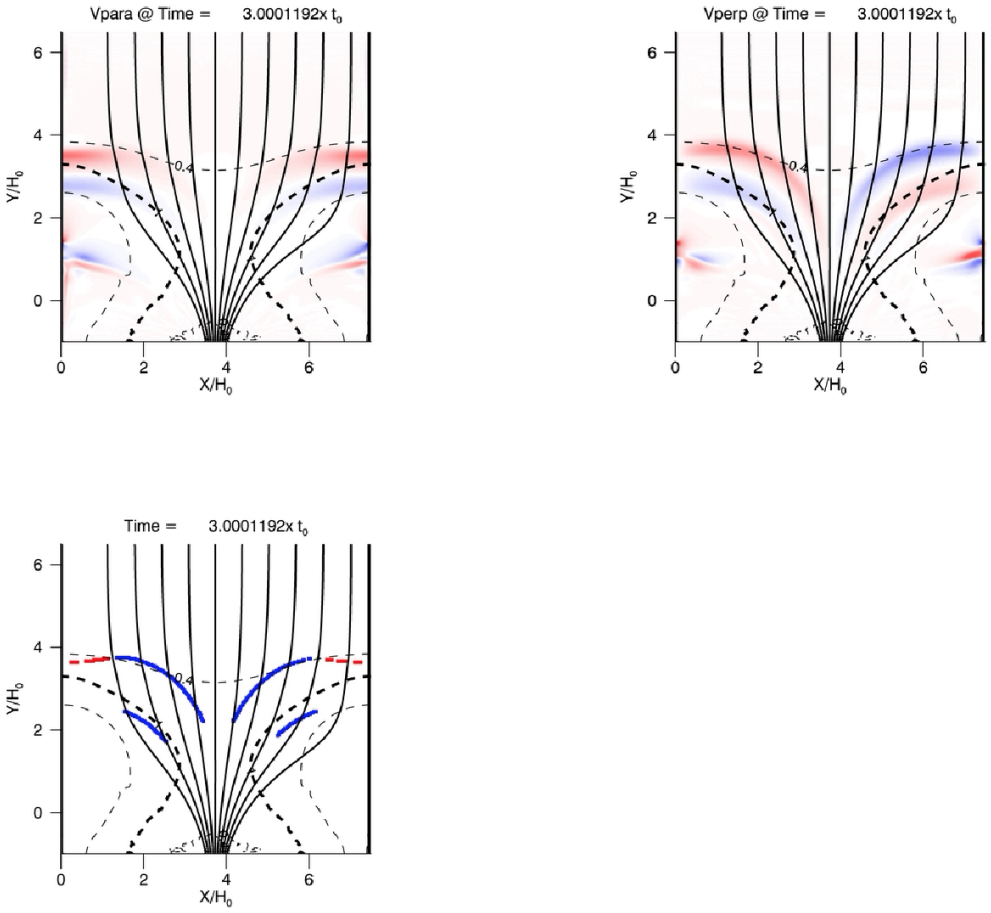

Figure 1.10: Results of a toy model simulation for demonstration of mode conversion. Upper-left: color shows the velocity that is parallel to the magnetic field, which demonstrates slow waves in the low-beta region. Upper-right: color shows the velocity that is perpendicular to the magnetic field, which demonstrates fast waves in the low-beta region. Lower-left: identification of fast shock (blue) and slow shock (red). In all the panels, solid lines are magnetic field lines. Dashed lines are contours for the distribution of plasma beta. The beta equals unity is marked by the thick dashed line.

(Hollweg et al., 1982; Ulmschneider et al., 1991; McAteer et al., 2003). The acoustic wave generated from mode coupling could steepen to shocks and contribute to chromospheric heating. Under this scenario, the energy balance in the flux tube is investigated (Brady & Arber, 2016; Arber et al., 2016; Wang & Yokoyama, 2020). The results show that the acoustic wave generated from mode coupling could provide enough energy that is consistent or larger than the required energy for chromospheric heating.

Carlsson et al. (2019) review previous studies and conclude that magnetoacoustic slow-mode shock waves are considered to play a key role in the energy balance of the chromosphere while transverse magnetic waves carrying a large energy flux upward into the outer atmosphere, with their role in the local energy balance still unclear.

1.3.4 Ambipolar diffusion

Ambipolar diffusion is caused by the collision between neutrals and ions. The dissipation of ambipolar diffusion becomes effective at regions with lower ionization degrees and stronger magnetic fields. The dissipation of ambipolar diffusion could lead to substantial heating locally (Khomenko & Collados, 2012; Martínez-Sykora et al., 2017; Soler et al., 2019). Martínez-Sykora et al. (2017) also show an example of how ambipolar diffusion affects the chromospheric dynamics by generation of jets.

However, because the ambipolar diffusion is sensitive to the local magnetic field and ionization degree, it is unclear whether the ambipolar diffusion plays an important role in chromospheric heating ubiquitously. Arber et al. (2016) compare the incompressible and compressible simulations and conclude that in the compressible simulation, considering the mode coupling between Alfvén wave and acoustic wave scenario, the acoustic shock heating dominates over the heating resulted from ambipolar diffusion.

As a result, the role of ambipolar diffusion in chromospheric heating can vary dras-

tically in different conditions. It is important to treat ambipolar diffusion carefully especially in the regions where the diffusivity is large. Such regions are characterized by lower ionization degrees and stronger magnetic fields.

1.4 Artificial model and realistic model

Numerical studies introduced in section 1.3.3 are all artificial in that they are carried on with artificial settings of geometry and initial conditions. They are used for studying the propagation of specific mode of waves in the chromosphere. The advantage of such model is that physics is clear. We can study the propagation, dissipation, transmission, or conversion of wave modes in detail. However, the result is dependent on the artificial choice of the settings and parameters. For example, Fawzy et al. (1998) and Fawzy (2010) claim that the shock formation and heating are dependent on the shape of the flux tube which is set in the initial condition. The artificial model usually considers the simulation region only inside the flux tube, thus waves that come from outside the flux tube are ignored. On the other hand, there are realistic simulations that aim to reproduce realistic environment and activity in the solar atmosphere. Examples are the simulation in Iijima & Yokoyama (2017), Gudiksen et al. (2011), and Sadykov et al. (2020). Realistic models include both flux tubes and canopy regions naturally with multiple modes of waves. However, the superposition of waves, together with conversion of wave modes, makes the physics in the model quite complicated. Therefore, realistic models are usually used for synthesized observation (Leenaarts et al., 2013; Rathore et al., 2015; Lin & Carlsson, 2015) without detailed analysis of propagation of waves in the chromosphere.

1.5 Motivation of this study

Chromospheric heating problem is one of the most important problems in solar physics. Different heating mechanisms are proposed by previous researches. However, a basic question is still left to be answered. Which heating mechanism is dominant? For answering this question, our study focuses on the averaged heating rate by different heating mechanisms. On the other hand, most of the areas (around 90 percent) of the sun are quiet regions (e.g. see Figure 2 in Sánchez Almeida, 2004). As a result, the starting point of our study is the averaged heating rate of different mechanisms in the quiet regions.

Previous studies propose different scenarios for the chromospheric heating mechanism. However, it is difficult to compare with each other as the previous theoretical works usually use the artificial model that only one or a few mechanisms could be included. On the other hand, previous studies using realistic simulations usually focus on synthesized observation without investigating the detailed physics about the heating mechanisms or the propagation of waves.

We are motivated by quantitatively comparing the role of different heating mechanisms. For this purpose, we perform realistic simulations while challenging investigating the propagation of waves in detail. We mainly focus on the wave heating mechanism since there is plenty of observational evidence supporting wave heating theory. We also validate the simulation results from the observation and make predictions of the observations for next generation telescopes. In this study, we develop our own method in automatically identifying the mode of the waves and calculate the related shock heating rate. There are two new points in our study. The first point is that we investigate the propagation of waves, modes of waves, and heating rate by different modes of waves in detail in a realistic simulation. The other point is that our results show that the fast magnetic wave is significant for chromospheric heating in the low-beta region. The role of fast magnetic waves in heating the low-beta chromosphere has not been investigated by previous

researches.

The rest of this dissertation is organized as follows. The methods of simulation and data processing, including the numerical settings, treatment of the chromospheric radiative loss, wave identification, and calculation of heating rate are introduced in Chapter 2. Results of the two-dimensional simulation are shown in Chapter 3. Results of the three-dimensional simulation are shown in Chapter 4. Results are discussed and summarized in Chapter 5. Finally, we show the conclusion in Chapter 6.

Chapter 2

Method

We performed two-dimensional and three-dimensional MHD numerical simulations in a Cartesian box covering the range from the surface part of the convection zone to the bottom part of the corona. Essential physics for addressing the problem is all included such as gravity, radiative loss in the chromosphere, and thermal conduction. As for measuring the wave heating, we developed an automatic procedure for detecting and diagnosing shock waves in the atmosphere. The simulations are performed with the RAMENS code (Iijima & Yokoyama, 2015; Iijima, 2016; Iijima & Yokoyama, 2017). One technical advantage of RAMENS is the usage of conservative form for the energy equation. For detailed information about the numerical scheme of the code, one could refer to Iijima (2016). The simulation and related settings are briefly described from Section 2.1 to Section 2.3. After obtaining the simulation results, we identify the position of shocks and calculate the shock heating rate from the entropy jump. The method for shock identification and heating rate calculation is described in Section 2.4 and 2.5.

2.1 Basic equations

We define that z direction is the vertical direction. x and y directions are the horizontal directions. Basic equations solved in our study are MHD equations with gravity, radiative loss, and thermal conduction along magnetic field lines:

$$\frac{\partial}{\partial t}(\rho) + \nabla \cdot (\rho \mathbf{V}) = 0, \tag{2.1}$$

$$\frac{\partial}{\partial t}(\rho \mathbf{V}) + \nabla \cdot \left[\rho \mathbf{V} \otimes \mathbf{V} + (P + \frac{B^2}{8\pi})I - \frac{\mathbf{B} \otimes \mathbf{B}}{4\pi}\right] = \rho \mathbf{g}, \tag{2.2}$$

$$\begin{aligned} \frac{\partial}{\partial t}(e) + \nabla \cdot \left[(e + P + \frac{B^2}{8\pi})\mathbf{V} - \frac{1}{4\pi}\mathbf{B}(\mathbf{V} \cdot \mathbf{B})\right] \\ = \rho(\mathbf{g} \cdot \mathbf{V}) + Q_{\text{cnd}} + Q_{\text{rad}} + Q_{\text{art}}, \end{aligned} \tag{2.3}$$

$$\frac{\partial}{\partial t}(\mathbf{B}) + \nabla \cdot (\mathbf{V} \otimes \mathbf{B} - \mathbf{B} \otimes \mathbf{V}) = 0. \tag{2.4}$$

The meaning of each term in the basic equations is listed in Table 2.1.

Term	Physical meaning
t	time
ρ	density
$\mathbf{V}$	velocity vector
$\mathbf{B}$	magnetic field
P	gas pressure
$\mathbf{g}$	gravity
e	total energy density, $e = e_{\text{int}} + \frac{1}{2}\rho\mathbf{V}^2 + \frac{\mathbf{B}^2}{8\pi}$
e_{int}	internal energy
Q_{cnd}	heating rate by thermal conduction
Q_{rad}	heating rate by radiation
Q_{art}	artificial heating

Table 2.1: Meaning of each term in the basic equations.

In our model, gravity is constant where $|\mathbf{g}| = 2.74 \times 10^4$ cm s^{-2}. The direction of $\mathbf{g}$ is in the $-z$ direction. Q_{art} is the artificial heating term to prevent extremely low temperature (lower than 2000 K in this case) in the chromosphere. The effect of Q_{art} is that plasma with temperature lower than 2000 K will be heated to 2000 K in few simulation time steps. Radiative loss Q_{rad} has three components, which are the radiative loss from LTE radiative transfer Q_{LTE} calculated in optically thick condition, chromospheric approximated radiative loss Q_{chrom}, and coronal approximated radiative loss Q_{cor}. The treatment of radiative loss gradually switches from solving LTE radiative transfer equation to approximated radiative loss term by decreasing of column mass. In the regions where the column mass is small, the approximated radiative loss treatment switch from chromospheric radiative treatment to coronal radiative loss treatment with increased temperature. To be more spe-

cific, the radiative loss term is expressed as

$$Q_{\rm rad} = \epsilon(c_{\rm mass})Q_{\rm LTE} + (1-\epsilon(c_{\rm mass}))[\zeta(T)Q_{\rm chrom} + (1-\zeta(T))Q_{\rm cor}], \tag{2.5}$$

where T is the temperature and $c_{\rm mass}$ is the column mass. The $c_{\rm mass}$ as a function of z is defined as follows

$$c_{\rm mass}(z) = \int_z^{z_{\rm top}} \rho(z'){\rm d}z', \tag{2.6}$$

where $z_{\rm top}$ is the height at the top of the simulation box.

$$\epsilon(c_{\rm mass}) = \begin{cases} 1, & \log_{10} c_{\rm mass} > \log_{10} c_{\rm mass,0} \\ \dfrac{\log_{10}(c_{\rm mass,1}/c_{\rm mass})}{\log_{10}(c_{\rm mass,1}/c_{\rm mass,0})}, & \log_{10} c_{\rm mass,0} > \log_{10} c_{\rm mass} > \log_{10} c_{\rm mass,1} \\ 0, & \log_{10} c_{\rm mass} < \log_{10} c_{\rm mass,1} \end{cases} \tag{2.7}$$

where $\log_{10} c_{\rm mass,0} = -1.5$ and $\log_{10} c_{\rm mass,1} = -2$ in c.g.s. unit.

$$\zeta(T) = \begin{cases} 1, & T < T_0 \\ \dfrac{T_1 - T}{T_1 - T_0}, & T_0 < T < T_1 \\ 0, & T > T_1 \end{cases} \tag{2.8}$$

where $T_0 = 10000$ K and $T_1 = 15000$ K.

The equations of state include the LTE ionization of hydrogen (H), helium (He), carbon (C), nitrogen (N), oxygen (O), and neon (Ne). The neutral hydrogen model with two energy levels is considered. Hydrogen molecule (H_2) is included through chemical equilibrium. The equations of state are shown as follows:

$$P = \left(\sum_{\rm i=1}^{2} n_{{\rm H\,I},i} + n_{\rm H\,II} + n_{\rm H_2} + \sum_{\rm j=0}^{2} n_{s,j} + n_{\rm e} \right) k_{\rm B} T, \tag{2.9}$$

$$e_{\text{int}} = \frac{3}{2}P + \sum_{\text{i=1}}^{2} \epsilon_{\text{H I},i} n_{\text{H I},i} + \epsilon_{\text{H II}} n_{\text{H II}} + \epsilon_{\text{H}_2} n_{\text{H}_2} + \sum_{\text{j=0}}^{2} \epsilon_{s,j} n_{s,j}, \tag{2.10}$$

where $n_{\text{H I},i}$ is the number density of neutral hydrogen in the i-th energy level. $n_{\text{H II}}$ is the number density of ionized hydrogen. $n_{s,j}$ is the number density for elements s (including He, C, N, O, and Ne) in ionization state j. $\epsilon_{\text{H I},i}$ is the energy level of neutral hydrogen in the i-th energy level. $\epsilon_{\text{H II}}$ is the energy level of ionized hydrogen. $\epsilon_{s,j}$ is the energy level for elements s in ionization state j. All the number densities described above are calculated from Boltzmann relation and Saha ionization equation. n_{H_2} is the number density of the molecular hydrogen. n_{H_2} is determined by the chemical equilibrium in Kurucz (1970). ϵ_{H_2} is the internal energy of molecular hydrogen calculated from the polynomial approximation in Vardya (1965).

The Spitzer-type thermal conduction is applied as follows

$$Q_{\text{cnd}} = -\nabla \cdot \mathbf{F}_{\text{cnd}}, \tag{2.11}$$

$$\mathbf{F}_{\text{cnd}} = -\kappa(\mathbf{b} \otimes \mathbf{b}) \cdot \nabla T, \tag{2.12}$$

where we set $\kappa = \kappa_0 T^{5/2}$ and $\kappa_0 = 10^{-6}$ in c.g.s. unit. $\mathbf{b}$ is the unit vector which have the same direction as the direction of the magnetic field, $\mathbf{b} = \mathbf{B}/|\mathbf{B}|$.

2.2 Radiative loss

2.2.1 Optically thick radiative transfer

Optically thick radiative transfer is calculated by solving the radiative transfer equation (Equation 1.1) with LTE and grey assumption. The radiative heating rate is calculated as

follows

$$Q_{\rm F} = -\nabla \cdot (\int_{4\pi} \mathbf{n} I_\nu {\rm d}\mathbf{\Omega}), \tag{2.13}$$

which is similar to the radiative loss described in Equation (1.4). Or alternatively,

$$Q_{\rm J} = 4\pi\alpha_{\rm R}(J - S), \tag{2.14}$$

which is similar to the radiative loss described in Equation (1.5). The difference between the radiative loss described in this section and that in Section 1.2 is that the Equation (1.4) and Equation (1.5) in Section 1.2 are for single frequency only. The radiative loss described in Equation (2.13) and Equation (2.14) is frequency integrated. The J, S, and $\alpha_{\rm R}$ are the angular averaged intensity, source function, and the absorption coefficient integrated in frequency. For implementation, we apply $\alpha_{\rm R} = \rho\kappa_{\rm R}$ where $\kappa_{\rm R}$ is the Rosseland mean opacity which is implemented as a function of density and temperature in the OPAL opacity table (Iglesias & Rogers, 1996).

$Q_{\rm F}$ and $Q_{\rm J}$ should be theoretically identical. However, it is pointed out that $Q_{\rm F}$ is suffered from numerical errors in optically thin regions and $Q_{\rm J}$ is suffered from numerical errors in optically thick regions (Bruls et al., 1999). As a result, we combine the two expressions as follows

$$Q_{\rm LTE} = {\rm e}^{-(\tau/\tau_0)^2} Q_{\rm J} + (1 - {\rm e}^{-(\tau/\tau_0)^2}) Q_{\rm F}, \tag{2.15}$$

where τ is the optical depth. $\tau(z) = \int_z^{z_{\rm top}} \alpha_{\rm R}(\rho(z'), T(z')){\rm d}z'$. τ_0 is set to 0.1.

2.2.2 Chromospheric radiative loss

The treatment of chromospheric radiative loss is different from that used in Iijima & Yokoyama (2015), Iijima (2016) ,and Iijima & Yokoyama (2017). In our simulation, we

use approximated treatment introduced in Carlsson & Leenaarts (2012) for the chromospheric radiative loss. This treatment mimics the non-local thermodynamic equilibrium (NLTE) effect including the radiative loss from neutral hydrogen (H I), singly ionized magnesium (Mg II), and singly ionized calcium (Ca II). As introduced in Section 1.2, H, Mg II, and Ca II are the three main components of chromospheric radiative loss. In this approach, the radiative loss is described by the following expression

$$Q_{\text{rad}} = -\sum_{X_m} L_{X_m}(T) E_{X_m}(\tau) \frac{N_{X_m}}{N_X}(T) A_X N_H n_e, \tag{2.16}$$

where the subscript X_m represents element X in ionization state m. X_m includes H I, Mg II, and Ca II. T is the temperature. A_X is the abundance of the element X which is a constant for a specific element. τ is the optical depth. $L_{X_m}(T)$ and $\frac{N_{X_m}}{N_X}(T)$ are the optically thin radiative loss function and the ratio of the number density of ions in specific ionization state m to the total number density of specific element X, respectively. $L_{X_m}(T)$ and $\frac{N_{X_m}}{N_X}(T)$ are assumed as functions of temperature T. $E_{X_m}(\tau)$ is the photon escape probability. N_{H} is the number density of hydrogen element. n_e is the number density of electrons. $L_{X_m}(T)$, $E_{X_m}(\tau)$, and $\frac{N_{X_m}}{N_X}(T)$ are given as numerical tables by fitting with a detailed radiative transfer calculation.

$L_{X_m}(T)$ is the optical thin radiative loss function. It is expected to be a function of temperature. Practically, L_{X_m} is calculated by summation of all the energy released by radiative de-excitation in detailed radiative transfer calculation. The function $L_{X_m}(T)$ is obtained by fitting the relationship between temperature and L_{X_m}.

$E_{X_m}(\tau)$ is the escape probability which indicates the probability that a photon finally escapes without being reabsorbed by the plasma on its propagation path. Naturally, this relation has a negative correlation with the optical depth τ. In practice, τ is not calculated, instead, since the absorption coefficient α has a positive relation with number density, it is assumed that τ also has a positive relation with column mass or column density. As

a result, $E_{X_m}(c_{\text{mass}})$ and $E_{X_m}(c_{\text{n}_\text{H}})$ are obtained by fitting the ratio of calculated radiative loss (including both absorption and emission) to L_{X_m} (including emission only) as a function of column mass (c_{mass}, for Mg II and Ca II) or column number density of neutral hydrogen (c_{n_H}, for hydrogen).

$\frac{N_{X_m}}{N_X}(T)$ indicates the ratio of the number density of ions in specific ionization state m to the total number density of specific element X. Generally speaking, this ratio should be related to electron density, temperature, as well as the previous state of the system. It is found from the detailed calculation that the fitting between $\frac{N_{X_m}}{N_X}$ and temperature yields a relatively satisfactory result (Carlsson & Leenaarts, 2012).

2.3 Boundary condition and initial condition

At the bottom boundary, the magnetic field is assumed to be vertical. Gas pressure at the boundary is adjusted that the total pressure balance is maintained in the horizontal direction. The gas pressure of the ghost cells is determined by extrapolation in vertical direction assuming the gradient is the same as the gradient at the boundary. Ghost cells are cells at the boundary whose values are not calculated by solving MHD equations. Instead, their values are determined by boundary conditions. In the region where vertical velocity is positive, entropy maintains a constant value, the velocity field damps to a constant upward flow that is identical to the averaged upward flow at the lower boundary. Horizontal velocity damps to zero. In the region where vertical velocity is negative, the vertical gradient of entropy and velocity is zero for all the ghost cells. Density and internal energy are calculated from gas pressure and entropy.

At the top boundary, the magnetic field is assumed to be vertical. Density is extrapolated exponentially by the scale height at the boundary. In the ghost cells, the velocity field and the internal energy per unit mass are maintained as a fixed value that is the same

as the values at the boundary at each horizontal position. There are exceptions which will be introduced later. Gas pressure is determined by density and internal energy. Moreover, to improve the numerical stability, at the top boundary, if the acoustic wave of both directions is propagation upwards (i.e. $V_{z0} + C_{s0} > V_{z0} - C_{s0} > 0$, where V_{z0} and C_{s0} are the vertical velocity and sound speed at the top boundary, respectively), we do not carry on density extrapolation. Instead, the density in the ghost cells is identical to the density at the boundary for a specific horizontal position. If the acoustic wave of both directions is propagating downwards (i.e. $V_{z0} - C_{s0} < V_{z0} + C_{s0} < 0$), the velocity in the ghost cells is set to zero. As we do not self-consistently solve the coronal heating, to maintain the high-temperature corona, the temperature at the upper boundary is set to 1 MK. This condition does not apply if the temperature at the boundary is already larger than 1 MK. Periodic boundary condition is applied for side boundaries.

The initial condition of the atmosphere is a plane parallel distribution that is uniform in the horizontal direction. Stratification in the vertical direction is a combination of model S in Christensen-Dalsgaard et al. (1996) below 0.5 Mm and a hydrostatic gravity stratified atmosphere above 0.5 Mm. The initial condition does not affect the distribution of the atmospheric structure after the system reaches a statistical equilibrium state. The initial magnetic field is homogenous that has vertical components only. The intensity of the magnetic field is subject to change in different cases.

2.4 Identification of shocks

We identify shock fronts in the chromosphere using the convergence of velocity. The positions of shock fronts are identified by

$$-\nabla \cdot \mathbf{V} \geq c_{\rm th}(C_{\rm s}/\Delta x), \tag{2.17}$$

where $c_{\rm th}$ is a parameter indicating the threshold for identification. The value of $c_{\rm th}$ is subject to change in different simulations. $C_{\rm s}$ is the speed of sound. Δx is the grid size. We apply a homogeneous grid size in this study. One snapshot of the distribution of $(-\nabla \cdot \mathbf{V})$ in the two-dimensional simulation is shown in Figure 2.1. We expect that there is only one pixel at each position along the shock front. However, multiple pixels may be selected at the shock front by examining the value of $\nabla \cdot \mathbf{V}$ only (left panel of Figure 2.2). In this situation, we remove the pixel that is not the local minimum of $\nabla \cdot \mathbf{V}$ in the direction of the propagation of the wave to guarantee that the thickness of the shock front is one pixel. The direction of propagation is determined by the direction of the gradient of total pressure. The results of a comparison between the selected shock front region only by threshold value and the shock front region after filtering by local minimum are shown in Figure 2.2.

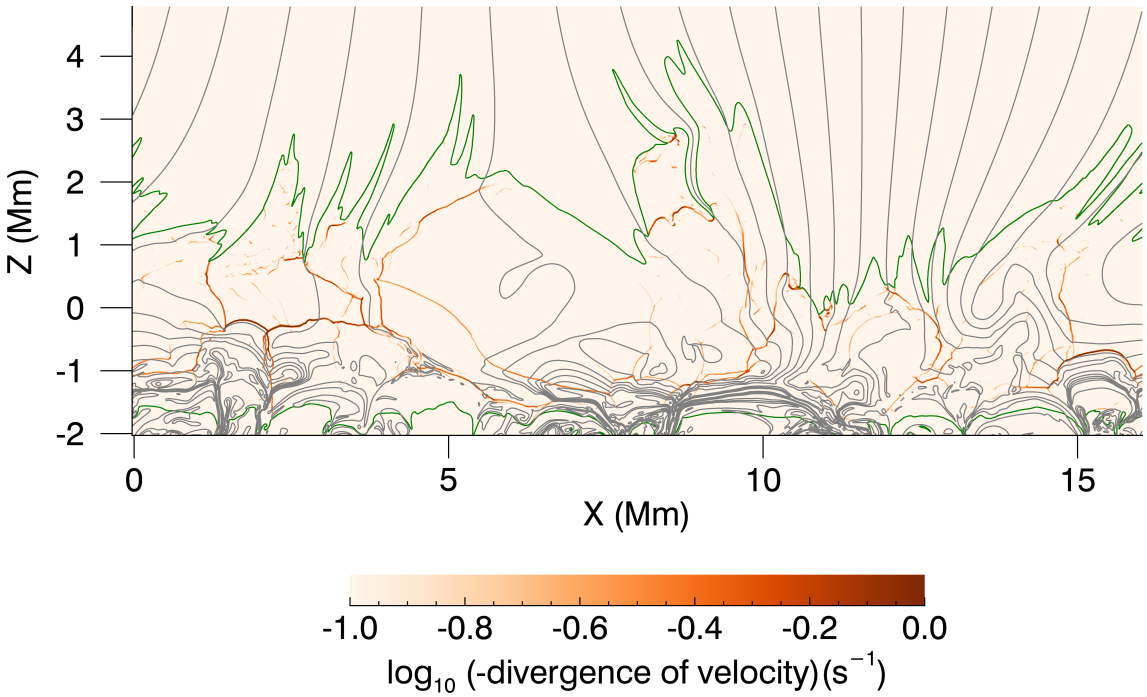

Figure 2.1: The distribution of $-\nabla \cdot \mathbf{V}$ of one snapshot in a two-dimensional simulation. The color shows $\log_{10}(-\nabla \cdot \mathbf{V})$ in unit s^{-1}. The grey lines are magnetic field lines. The green line marks the position of the transition region identified by $T = 10^4$ K.

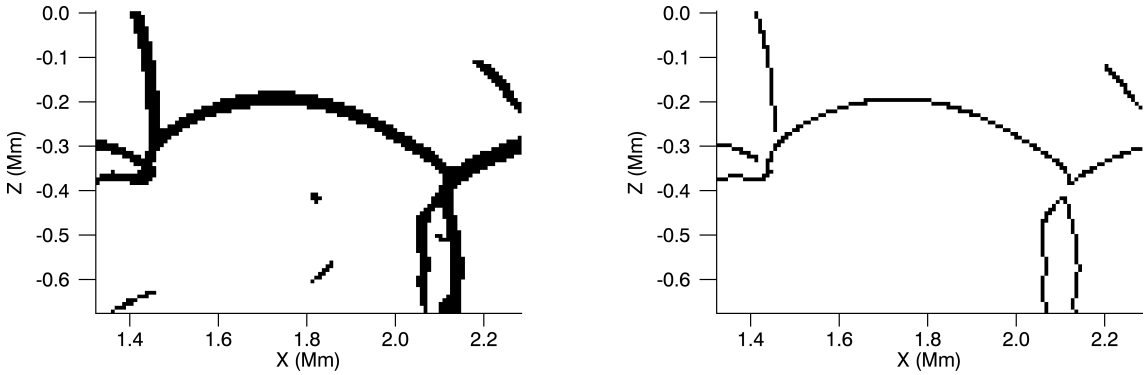

Figure 2.2: Example of the identification of shocks by only threshold value before (left panel) filtering the local minimum and after (right panel) filtering the local minimum of $\nabla \cdot \mathbf{V}$.

2.5 Heating rate at shocks

For the calculation of heating rate, we extract the density, temperature, velocity, gas pressure, and magnetic pressure at the upstream and downstream regions of the shock. Note that though the shown examples in this chapter are from two-dimensional simulation results, we also use the same method for the three-dimensional case. The sampling location of the upstream and downstream variables are at the position of the first local maximum and minimum of $\partial^2 V_l/\partial l^2$ beside $l = l_{\rm c}$, respectively, where V_l is the velocity along the direction of propagation. l is the distance along the direction of propagation. $l_{\rm c}$ corresponds to the position on the shock front. The upstream side is determined by the side with lower density. Pearson product-moment correlation coefficient between $\partial P/\partial l$ and $\partial P_{\rm m}/\partial l$ across the shock front is used to determine whether it belongs to fast shock (positive value, see panel (g) and (h) in Figure 2.3) or slow shock (negative value, see panel (g) and (h) in Figure 2.4), where P is the gas pressure and $P_{\rm m}$ is the magnetic pressure. $P_{\rm m} = (|\mathbf{B}^2|)/(8\pi)$. Pearson product-moment correlation coefficient of two variables X and Y is defined as

$$r(X,Y) = \frac{\sum_{i=1}^{n}(X_i - \overline{X})(Y_i - \overline{Y})}{\sqrt{\sum_{i=1}^{n}(X_i - \overline{X})^2 \sum_{i=1}^{n}(Y_i - \overline{Y})^2}}, \tag{2.18}$$

where $\overline{X}$ and $\overline{Y}$ is the averaged value of the variable X and Y, respectively.

The heating rate is calculated by

$$Q_{\rm s} = U_1 \rho_1 T_1 (S_{\rm m,1} - S_{\rm m,2}), \tag{2.19}$$

where subscribe 1 and 2 denote the physical parameters that are sampled or calculated at the upstream and downstream region, respectively. U is the normal velocity in shock rest frame; T is the temperature; $S_{\rm m}$ is the entropy per unit mass. U_1 is calculated by mass conservation $U_1\rho_1 = U_2\rho_2$ and the relation of velocity in different frame of reference that $V_1 - V_2 = U_1 - U_2$, where ρ is density. V is velocity in the laboratory frame. Examples of low-beta fast wave and slow wave are shown in Figure 2.3 and Figure 2.4.

Heating rate $Q_{\rm s}$ in Equation (2.19) is calculated at the shock front which describes the heating rate per unit area on the surface of the shock front. To estimate the heating rate per unit volume, we assume the heating is evenly distributed in the volume of one grid point at the shock front. As a result, the heating rate per unit volume is calculated by

$$Q_{\rm heat} = Q_{\rm s}/w_{\rm shock}, \tag{2.20}$$

where $w_{\rm shock}$ is the width of the shock wave, which is assumed to be identical to the grid size in this study. We also set $Q_{\rm heat} = 0$ outside the shock region. As a result, the spatial integration of $Q_{\rm heat}$ does not depend on $w_{\rm shock}$.

The entropy jump is calculated by solving the following equations

$$S_{\rm m,2} - S_{\rm m,1} = \int_{e_{\rm int,1}}^{e_{\rm int,2}} (\frac{\partial S_{\rm m}}{\partial e_{\rm int}})_\rho {\rm d}e_{\rm int} + \int_{\rho_1}^{\rho_2} (\frac{\partial S_{\rm m}}{\partial \rho})_{e_{\rm int}} {\rm d}\rho, \tag{2.21}$$

where

$$(\frac{\partial S_{\rm m}}{\partial e_{\rm int}})_\rho = \frac{1}{\rho T}, \tag{2.22}$$

$$(\frac{\partial S_{\mathrm{m}}}{\partial \rho})_{e_{\mathrm{int}}} = -\frac{e_{\mathrm{int}} + P}{\rho^2 T}. \tag{2.23}$$

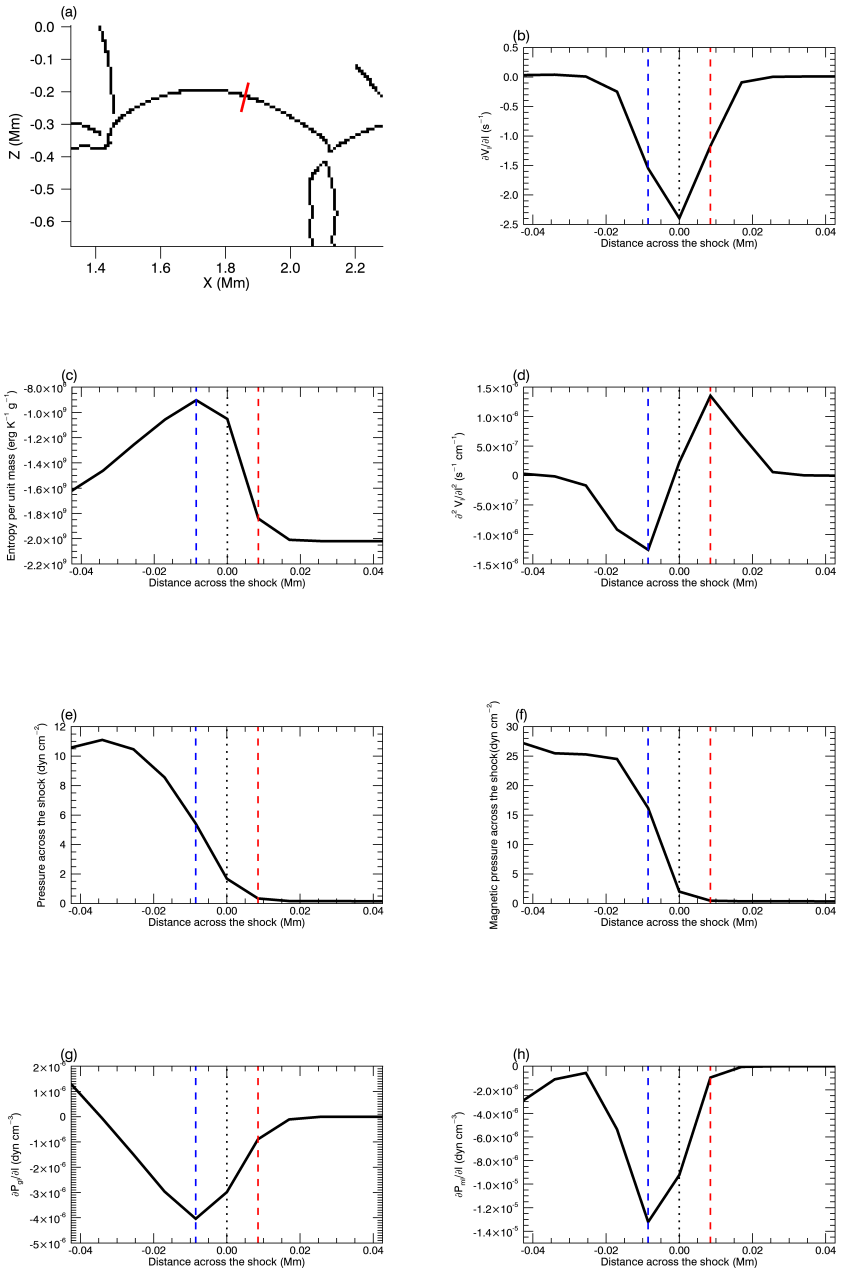

Figure 2.3: An example of identification of fast shock. (a): A binary image where the black color corresponds to shock front. The red solid line marks the direction of the propagation of the shock and the position of the slice across the shock. Other physical parameters that are plotted in panel (b) to (h) take the position along this red solid line. (b): $\nabla \cdot \mathbf{V}$. (c): Entropy per unit mass. (d): $\frac{\partial^2 V_l}{\partial l^2}$, the positions of maximum value and minimum value of this parameter determine the positions of upstream and downstream regions of the shock. The position of the upstream region is marked by the red dashed line in all panels except the panel (a). The position of the downstream region is marked by the blue dashed line in all panels except the panel (a). (e): Gas pressure. (f): Magnetic pressure. (g): $\frac{\partial P_{\rm gl}}{\partial l}$, gradient of gas pressure along the direction of propagation. (h): $\frac{\partial P_{\rm ml}}{\partial l}$, gradient of magnetic pressure along the direction of propagation. Panel (g) and (h) are used to determine whether the shock is a fast shock or slow shock.

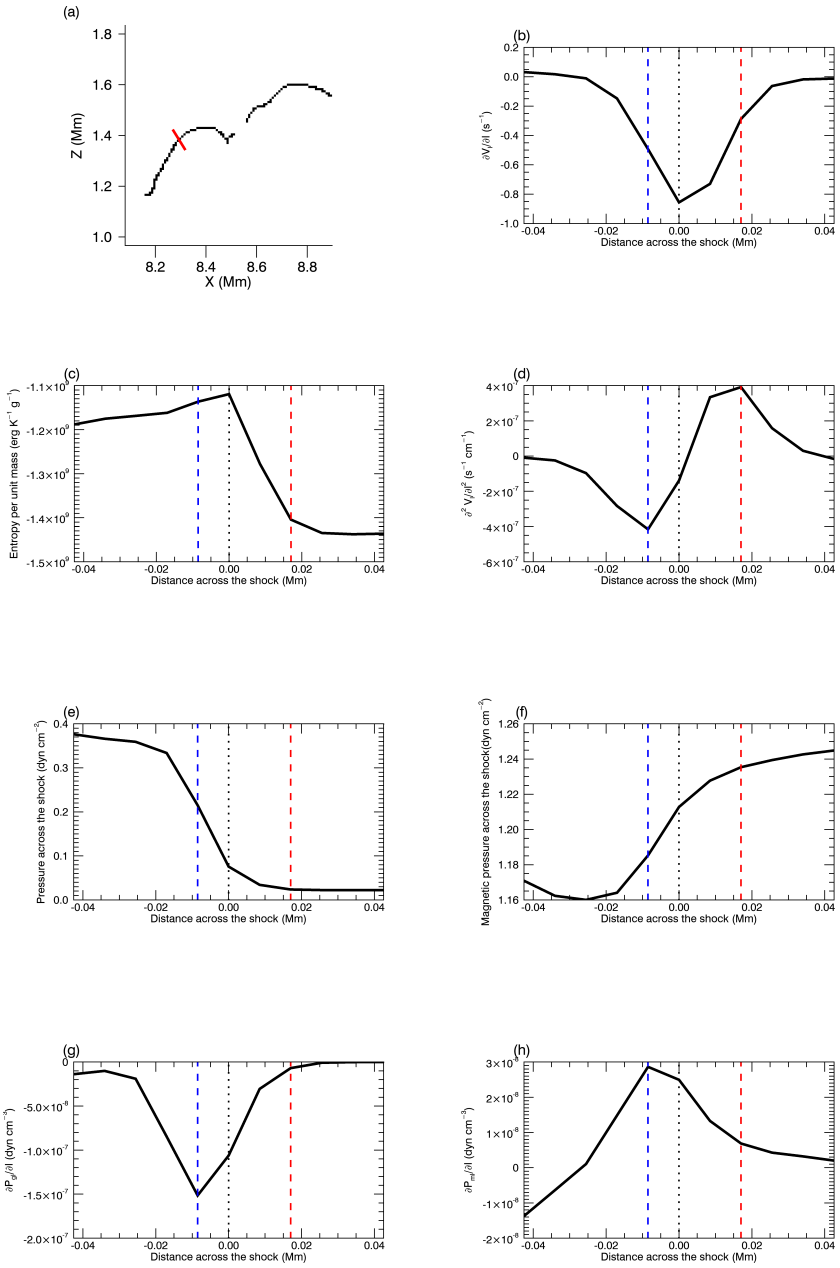

Figure 2.4: The same as Figure 2.3 but for a slow shock.

Chapter 3

Two-dimensional simulation

3.1 Introduction

In this chapter, we introduce the results of the two-dimensional simulations. The motivation for carrying on this two-dimensional study is that by taking advantage of the simple geometry, we can perform a detailed analysis of the propagation, transmission, and conversion of different wave modes. Moreover, there are comprehensive previous studies in both artificial models and realistic models for comparison. High resolution is available in the two-dimensional simulation that could be possible for discussing the ambipolar diffusion.

The propagation of MHD waves in the chromosphere has been well studied by previous researches in artificial two-dimensional models (e.g. Bogdan et al., 2003; Hasan & van Ballegooijen, 2008). Previous studies especially focus on the linear mode conversion that occurs close to the equipartition layer. Since most of the regions in the photosphere except the footpoints of flux tubes are the high-beta regions and the chromosphere close to the transition region is the low-beta region, waves that originated from the high-beta chromosphere will suffer mode conversion during their propagation in the chromosphere.

It is widely accepted that the acoustic wave (fast wave in the high-beta region and slow wave in the low-beta region) is significant for energy balance in the chromosphere. However, the role of the magnetic wave (fast wave in the low-beta region and Alfvén wave) is still unclear. The results in this chapter focus on the contribution of chromospheric heating from different modes of waves. We also estimate the potential contribution to heating from ambipolar diffusion.

3.2 Simulation settings

Basic settings have already been described in Chapter 2 and will not be repeated here. The simulation domain is a 16 Mm $\times$ 16 Mm square. We define the x direction as the horizontal direction and z direction as the vertical direction. In the z direction. the height extends from -2 Mm below the bottom of the photosphere to 14 Mm in the corona. The grid size is 8.5 km $\times$ 8.5 km. This grid size is much smaller than the typical wavelength in the chromosphere and the pressure scale height. The initial magnetic field is homogeneous with only z component. The intensity of the magnetic field is 6 G, which determines the averaged magnetic field in the corona due to flux conservation. Our analysis includes 1000 s of solar time which is one order larger than the typical dynamic timescale of the chromosphere.

3.3 Results

3.3.1 Structure of the atmosphere

One snapshot of the simulation result is shown in Figure 3.1. Results of wave mode identification and heating rate of the same snapshot are shown in Figure 3.2. The simulation

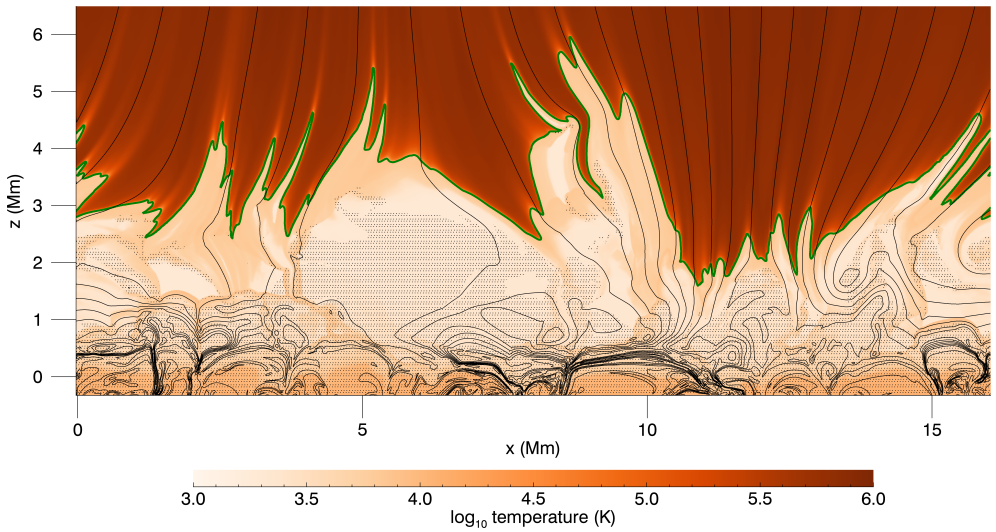

Figure 3.1: One snapshot of the simulation result. The green line marks the position of the transition region (10000 K). Grey lines are magnetic field lines. The dotted shadow marks the region where sound speed is larger than Alfvén speed. The color shows the temperature in log scale. Only part of the simulation domain in the vertical direction is shown in this figure.

results show a picture of dynamic chromosphere fulfilled with shocks. The atmospheric structure as a function of height is shown in Figure 3.3. In panel (b) of Figure 3.3, there are three horizontal plateaus (around 6000 K, 10000 K, and 22000 K). These temperatures are associated with the LTE ionization of H I, He I, and He II, which appears when using the LTE equation of state (Golding et al., 2016). The spicules lead to a drastic change in the height of the chromosphere. In order to study the averaged stratification of the chromosphere and reduce the morphological offset of spicules, we also plot the atmospheric structure as a function of column mass in Figure 3.4. One snapshot of the distribution of column mass is shown in Figure 3.5. The column mass is defined by Equation (2.6).

3.3.2 Energy balance in the chromosphere

The time and horizontal averaged radiative loss rate and the heating rate is shown in Figure 3.6. The shock heating is balanced with radiative loss below 2.5 Mm. At a location higher than 3 Mm, heating from heat conduction is larger than the shock heating. However, this

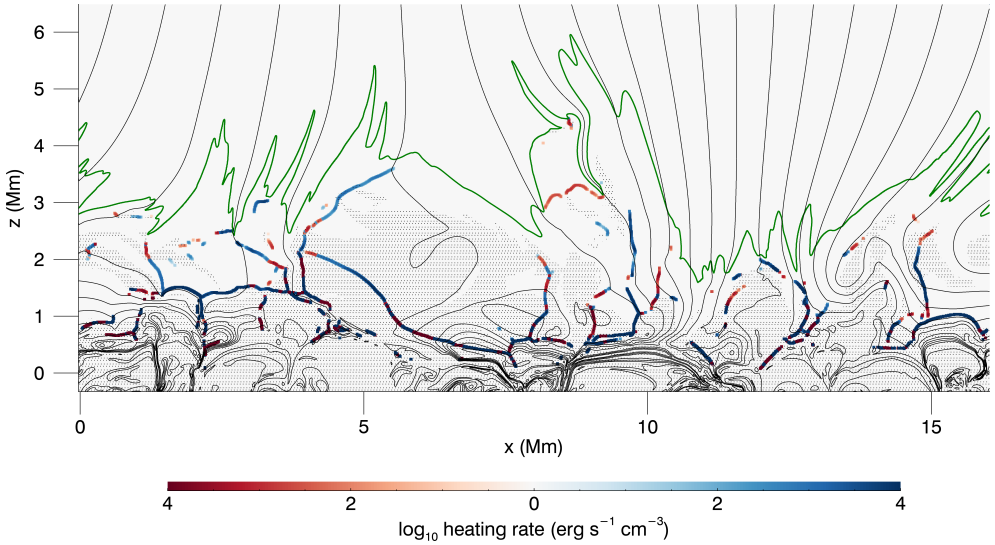

Figure 3.2: One snapshot of the simulation result. The green line marks the position of the transition region (10000 K). Grey lines are magnetic field lines. The dotted shadow marks the region where sound speed is larger than Alfvén speed. Shocks are identified and the corresponding heating rate is plotted in blue (fast shock) and red (slow shock) color. Only part of the simulation domain in the vertical direction is shown in this figure.

does not mean that the heat conduction becomes dominant over shock heating for the chromospheric plasma of this range of height. The heating from heat conduction mainly balances with radiative loss in the transition region without heating the chromospheric plasma. Since the vertical stratification of column mass will follow the up and down motion of the transition region (see Figure 3.5), we plot shock heating, conduction heating, and radiative loss in column mass scale for a clearer demonstration of the energy balance close to the transition region. The result is shown in Figure 3.7. It is shown that the heat conduction is the dominant heating term in the region where $c_{\rm mass} < 10^{-5.5}$ g cm^{-2}. One should be careful that direct comparison of the amount of heating rate and cooling rate in Figure 3.7 is not appropriate because heating and cooling do not occur at the same position spatially.

Because of the dynamic behavior of the spicule launch, the plasma around the transition region, especially in the region of 2.5 Mm $< z <$ 4 Mm consists of a mixture of cool chromospheric plasma and relatively hot coronal plasma. In order to focus only on the thermal balance of the cool chromospheric plasma, we make plots of the heating

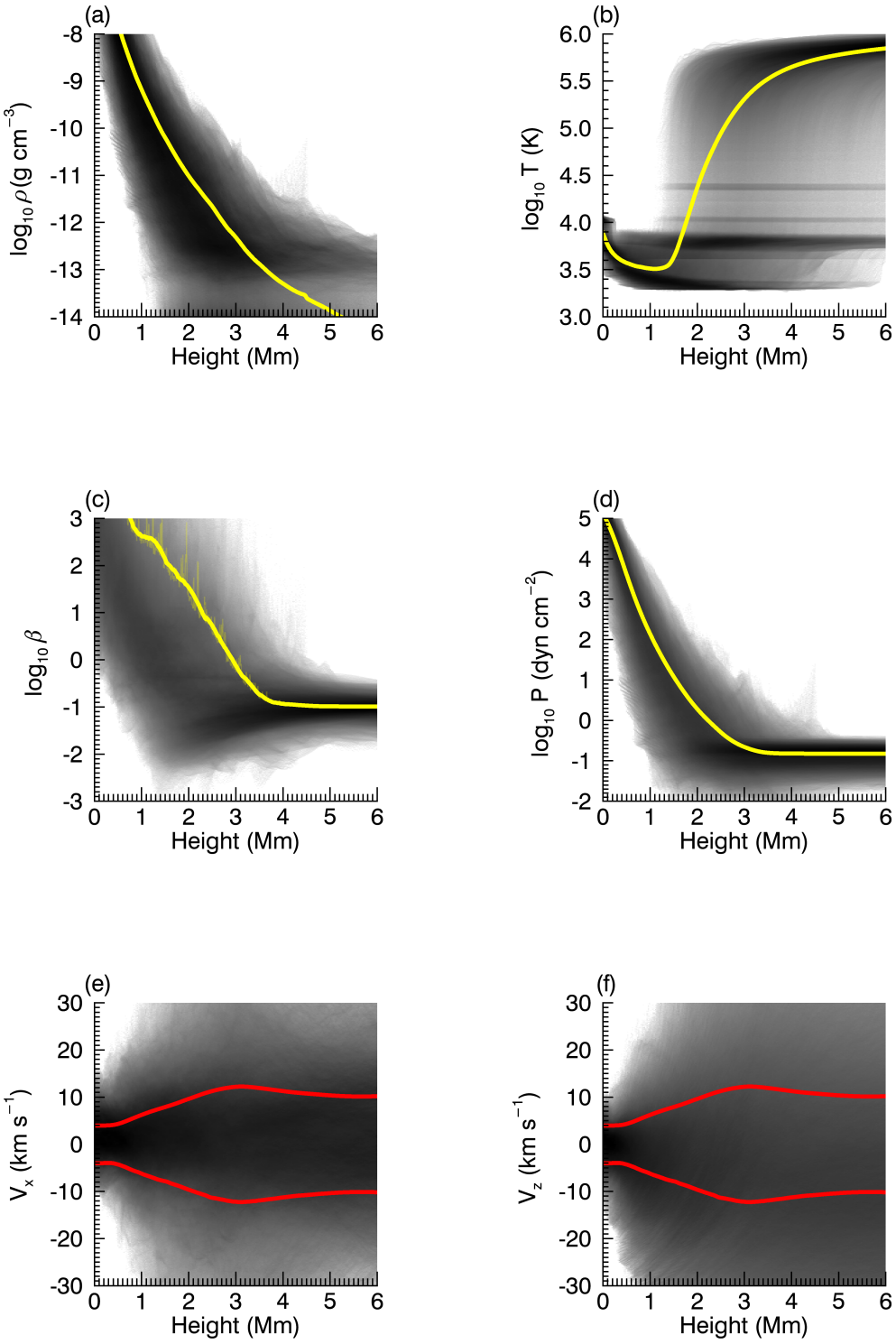

Figure 3.3: Vertical structure of the simulation in scale of height. (a): density; (b): temperature; (c): plasma beta; (d): gas pressure; (e): horizontal velocity; (f): vertical velocity. Yellow lines in panel (a) to (d) show the averaged value. Specifically, in panel (c), the thin yellow line shows the averaged value that is directly calculated from the original data, and the thick yellow line shows the result after being smoothed by a Savitsky-Golay filter. Red lines in panel (e) and (f) show the root mean square of the velocity.

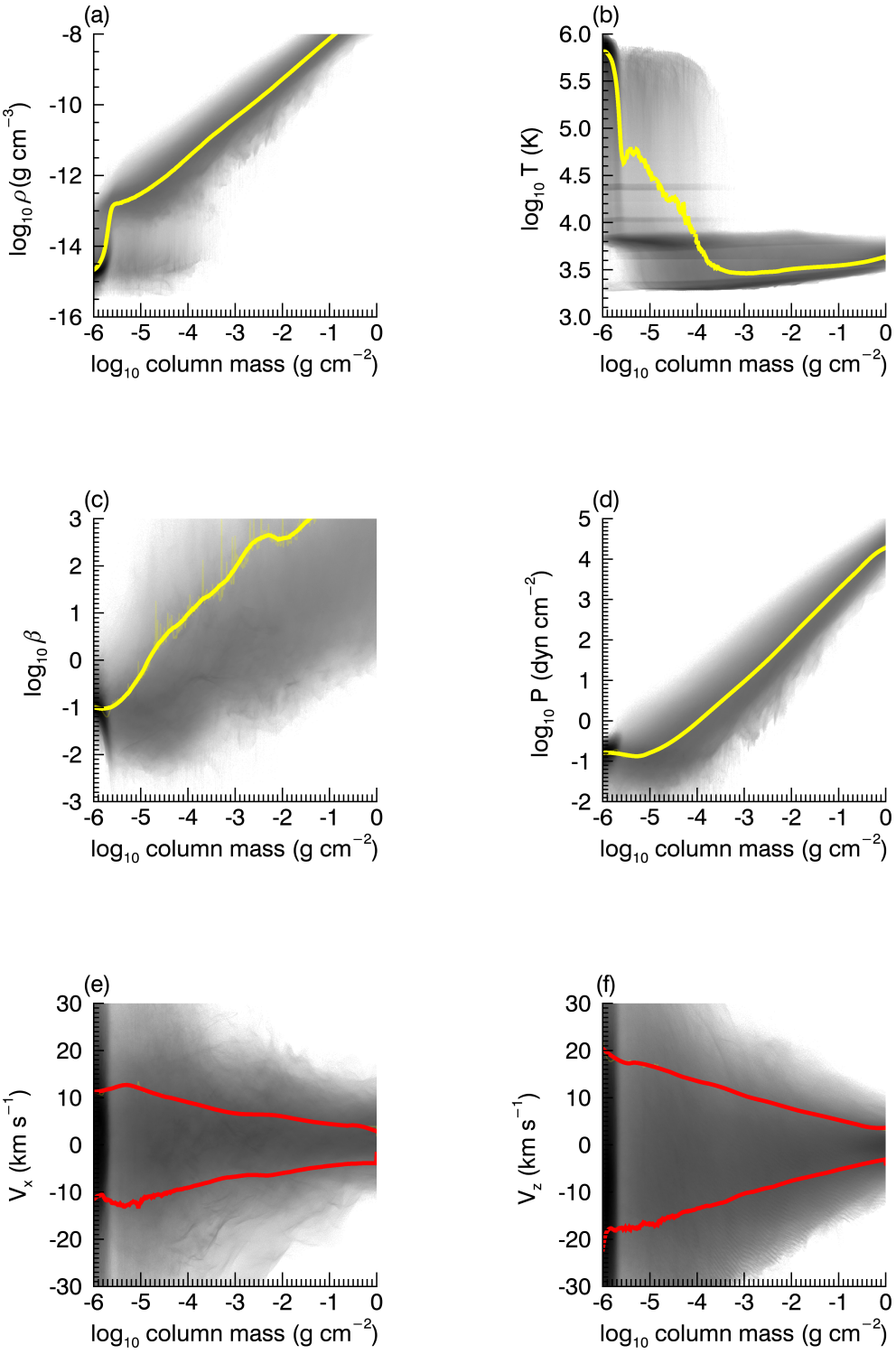

Figure 3.4: Vertical structure of the simulation in scale of column mass. (a): density; (b): temperature; (c): plasma beta; (d): gas pressure; (e): horizontal velocity; (f): vertical velocity. Yellow lines in panel (a) to (d) show the averaged value. Specifically, in panel (c), the thin yellow line shows the averaged value that is directly calculated from the original data, and the thick yellow line shows the result after being smoothed by a Savitsky-Golay filter. Red lines in panel (e) and (f) show the root mean square of the velocity.

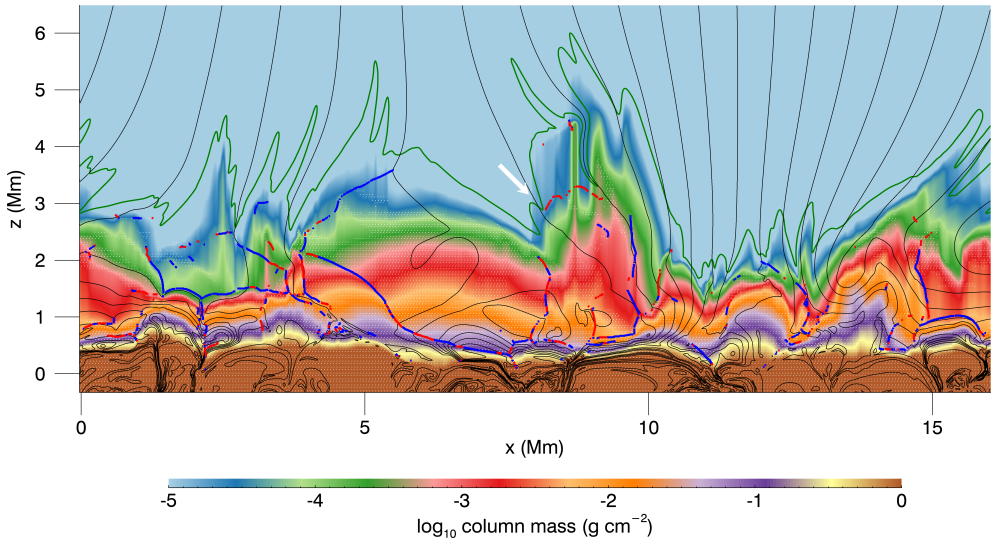

Figure 3.5: One snapshot of the simulation result. The color shows the column mass in log scale. The green line marks the position of the transition region (10000 K). Grey lines are magnetic field lines. Dotted shadow marks the region where sound speed is larger than Alfvén speed. Shocks are identified and plotted in blue (fast shock) and red (slow shock) colors. The white arrow points to the region where chromospheric plasma is located above the corona plasma, leading to abnormally large column mass in the corona. Only part of the simulation domain in the vertical direction is shown in this figure.

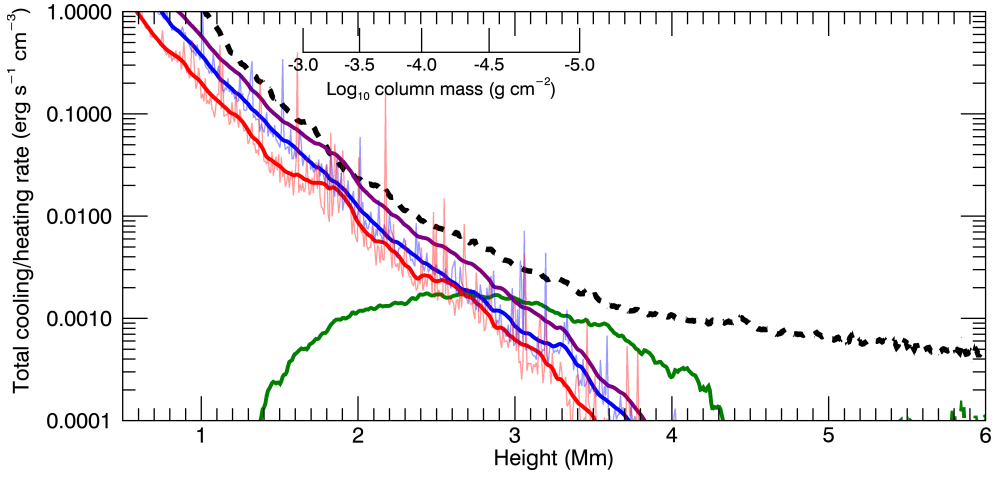

Figure 3.6: Heating and radiative loss rate as a function of height. The black dashed line is the total radiative loss rate in the simulation. The blue solid line is the fast wave heating rate. The red solid line is the slow wave heating rate. For blue and red lines, the thin lines with perturbation are the results directly calculated from the simulation while we also smooth the results by a Savitsky-Golay filter and plot them in thick lines. The purple line is the total shock heating rate after smoothing. The green line is the heating rate from heat conduction. The averaged column mass at each height is shown in the secondary axis.

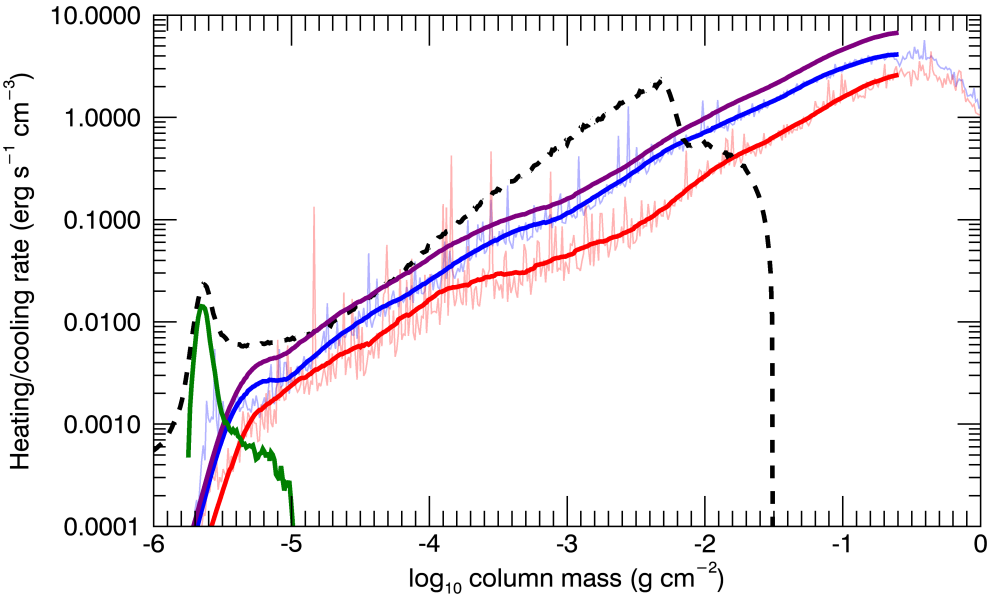

Figure 3.7: The same as Figure 3.6 but in column mass scale.

and cooling rates of the *chromospheric plasma* defined by the following criteria, i.e., (1) $T < 10^4$ K and (2) $c_{\rm mass} > 10^{-5.5}$ g cm^{-2}. The temperature threshold value is used because column mass could not identify chromospheric plasma in some specific cases when part of the chromospheric plasma is located above corona plasma. One example is shown by the white arrow in Figure 3.5. The results of energy balance are shown in Figures 3.8 and Figure 3.9. It is found that the balance between the heating and cooling rates is much improved in this analysis.

In order to investigate the energy balance in the low-beta region, we make the same plot as Figure 3.8 and Figure 3.9 in Figure 3.10 and Figure 3.11 but only for the low-beta component. Cooling and heating are set to zero for high-beta plasma. It is shown that despite the height and column mass, the fast magnetic wave plays a significant role in heating the low-beta chromosphere.

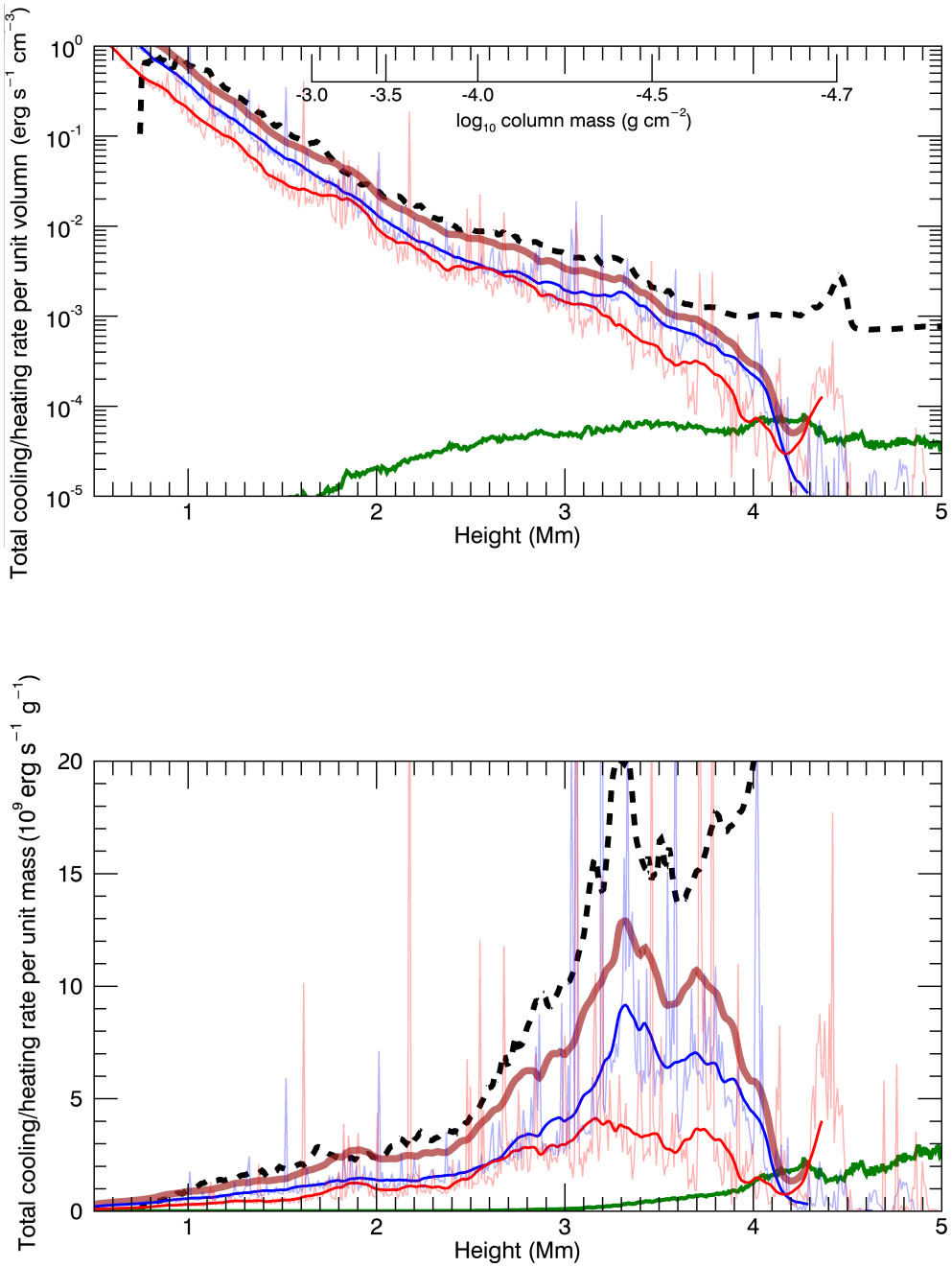

Figure 3.8: Heating and radiative loss rates as a function of height. The black dashed line is the total radiative loss rate in the simulation. The blue solid line is the fast wave heating rate. The red solid line is the slow wave heating rate. For blue and red lines, the thin lines with perturbation are the results directly calculated from the simulation while we also smooth the results by a Savitsky-Golay filter and plot them in thick lines. The brown solid line is the total heating rate that includes both fast wave and slow wave heating rate after smoothing. The green line is the heating rate from heat conduction. The averaged column mass at each height is shown in the secondary axis. In the upper panel, the heating and cooling rates are shown per unit volume. In the lower panel, the heating and cooling rates are shown per unit mass. The results in the lower panel are calculated from the results in the upper panel and are normalized by the horizontal and temporal averaged density at each height.

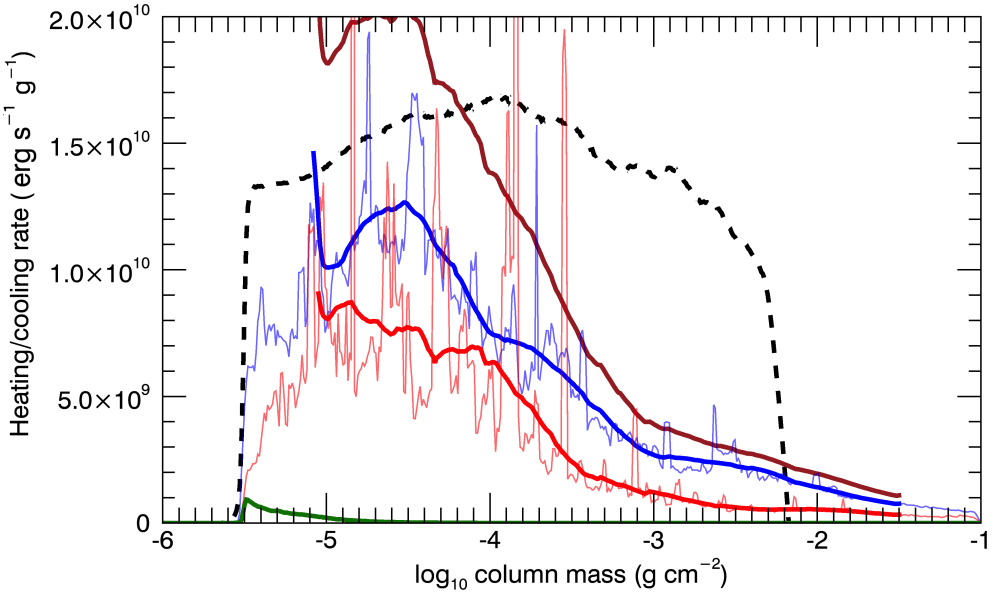

Figure 3.9: Heating and radiative loss rate per unit mass as a function of column mass. The black dashed line is the total radiative loss rate in the simulation. The blue solid line is the fast wave heating rate. The red solid line is the slow wave heating rate. For blue and red lines, the thin lines with perturbation are the results directly calculated from the simulation while we also smooth the results by a Savitsky-Golay filter and plot them in thick lines. The brown solid line is the total heating rate that includes both fast wave and slow wave heating rate after smoothing. The green line is the heating rate from heat conduction.

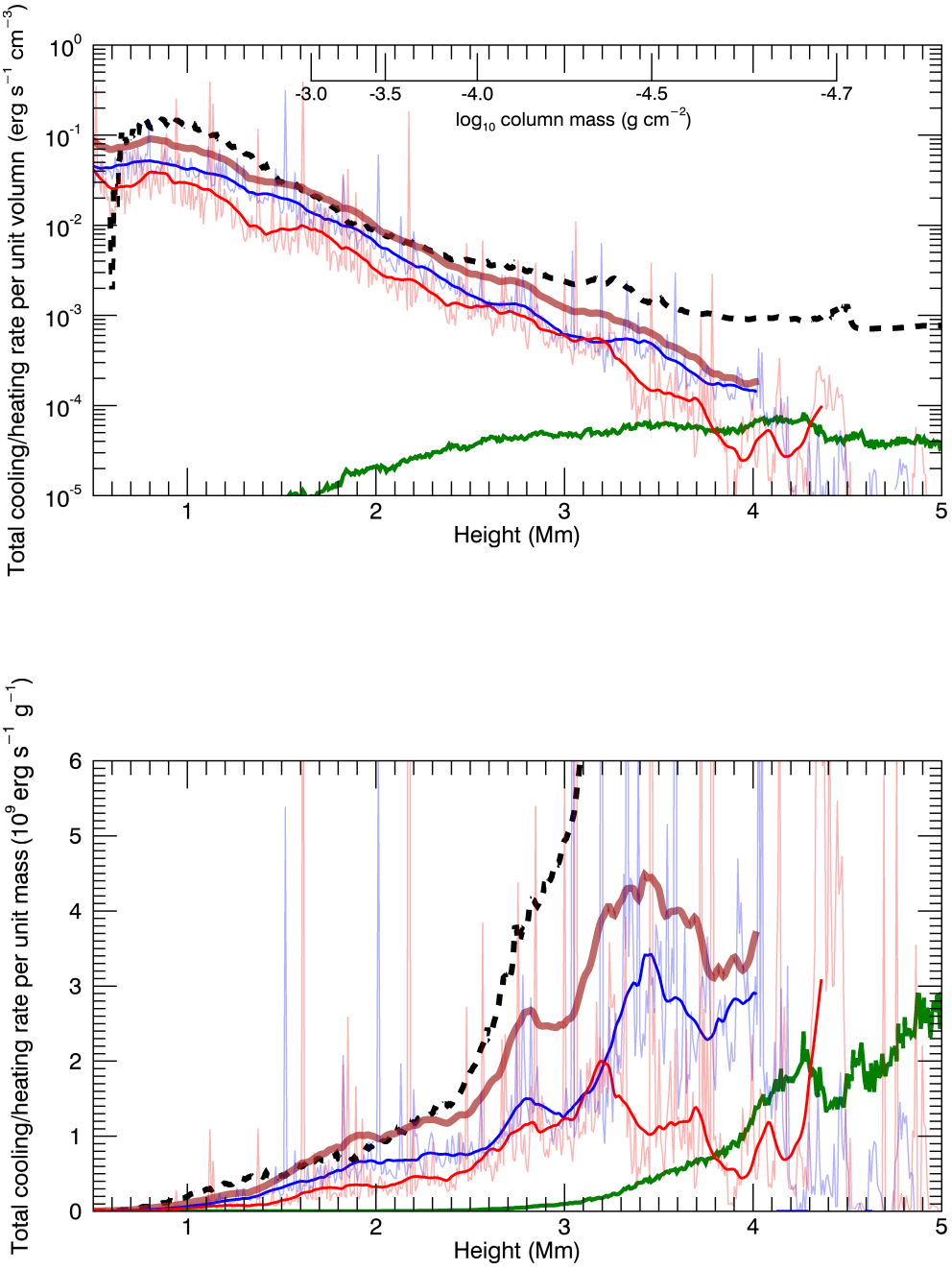

Figure 3.10: The same as Figure 3.8 but for low-beta component only.

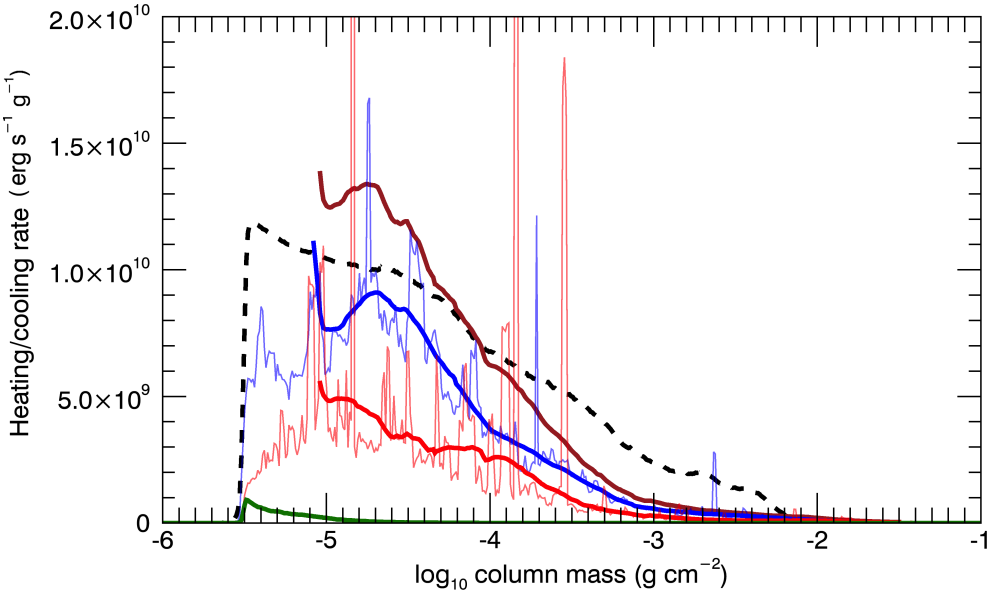

Figure 3.11: The same as Figure 3.9 but for low-beta component only.

3.3.3 Generation of waves in the low-beta regions

We further investigate the generation mechanism of the fast magnetic waves in the low-beta region. We track the propagation of fast magnetic waves and find that such waves originate from the fast acoustic waves in the high-beta regions through mode conversion (e.g. Cally, 2006, see Section 1.3.3). One example of the mode conversion event is shown in Figure 3.12. In this example, the wave vector is normal to the field lines when the wave crosses the equipartition layer. This is supposed to be a setup with efficient mode conversion according to the analytical theories (Equation 1.19). On the other hand, effective transmission occurs at a small attacking angle (Figure 3.13).

3.4 Magnetic field structure: enhanced magnetic field

The averaged magnetic field intensity varies in different regions of the sun, which changes the magnetic field structure in the chromosphere. The mode conversion and transmission are dependent on the attacking angle and relate to the structure of the magnetic field

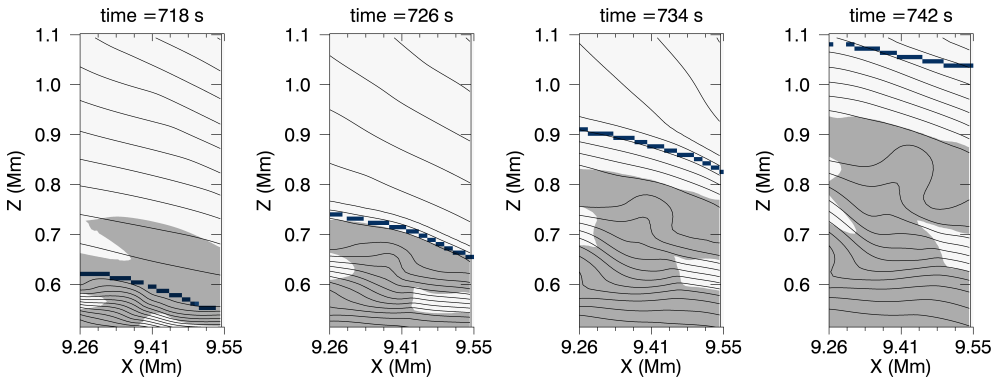

Figure 3.12: An example of a fast acoustic wave to fast magnetic wave mode conversion. Time evolution is shown from the left to right with a time interval of 8 s. In each panel, grey lines are magnetic field lines. The blue line shows the position of a fast shock. The grey shadow marks the region where sound speed is larger than Alfvén speed.

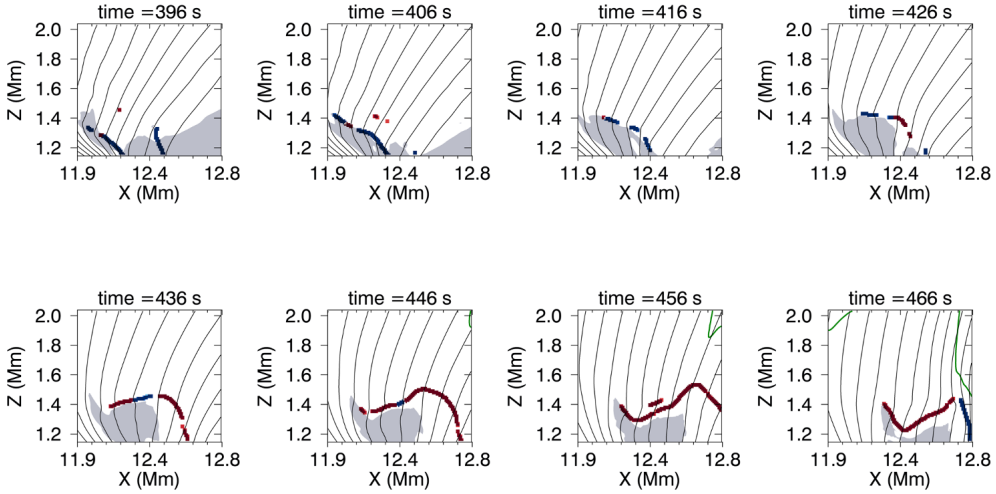

Figure 3.13: An example of a fast acoustic wave to slow acoustic wave mode transmission. Time evolution is shown in different panels with a time interval of 10 s. In each panel, grey lines are magnetic field lines. The blue line shows the position of a fast shock. The red line shows the position of a slow shock. When the shock wave crosses the equipartition layer, its color changes from blue (fast shock) to red (slow shock) but maintains its nature as an acoustic shock. The grey shadow marks the region where sound speed is larger than Alfvén speed.

in the chromosphere. For comparison, we carry on another simulation with the same setting except the only difference that the averaged vertical magnetic field increases from 6 G (hereinafter case 6) to 20 G (hereinafter case 20). The atmospheric structures as a function of height and column mass are shown in Figure 3.14 and 3.15. The atmospheric structures of case 20 are similar to that in case 6 except for the distribution of plasma beta. The plasma beta drops to 0.01 in the higher part of the chromosphere and the corona in case 20, compared with 0.1 in case 6. One snapshot of the shock identification and heating of case 20 is shown in Figure 3.16. It is found that the magnetic field is straighter and the slow wave appears more frequent in case 20 than case 6.

We plot the chromospheric energy balance for case 20 in Figure 3.17 and 3.18. The low-beta component is shown in Figure 3.19 and 3.20. The energy balance in case 20 is similar to case 6. A quite well balance between shock heating and radiative loss is achieved. There is a difference between case 6 and case 20 in heating the plasma of different column mass (e.g. compare Figure 3.9 with Figure 3.18). In case 6, the heating from the fast wave is comparable with the heating from the slow wave in all the regions. However, in case 20, in the region where column mass is smaller than $10^{-4.1}$ g cm^{-2}, the slow acoustic waves are more dominant than the fast magnetic wave.

The mode transmission from the fast acoustic wave in the high-beta region to the slow acoustic wave in the low-beta region becomes efficient if the attacking angle is small. We compare the averaged inclination angle ($\alpha_{\rm i}, \tan\alpha_{\rm i} = B_x/B_z$) of the magnetic field between the two cases (Figure 3.21). The magnetic field is more vertical in case 20 than in case 6. Consequently, the transmission is more efficient in case 20 for waves that propagate upwards.

To give a brief summary of case 20, we find that the heating contributed from the fast magnetic shock waves is still significant. On the other hand, the heating from the slow acoustic wave becomes dominant at a higher position ($c_{\rm mass} < 10^{-4.1}$ g cm^{-2}). The

dominance of slow magnetic wave does not occur in case 6.

3.5 Discussion

The new point of this study is that we emphasize the fast magnetic wave could contribute to chromospheric heating in the low-beta region. Although the propagation of MHD waves in the chromosphere has been well studied in previous researches while the heating of fast magnetic waves in the low-beta region has not been investigated carefully by previous researches.

Hasan & van Ballegooijen (2008) study the wave propagation in detail, but they mainly focus on the slow acoustic waves inside the flux tube. They mention the mechanism that the acoustic waves originated away from the flux tube will generate fast magnetic waves through mode conversion due to large attacking angles. The generation mechanism of the fast magnetic wave in our study is the same as theirs. However, they do not quantitatively study the contribution of different modes in chromospheric heating (neither by other theoretical works e.g. Bogdan et al., 2003; Fedun et al., 2011). By tracking each wavefront, we quantify the contribution by fast waves for the first time.

Brady & Arber (2016) discuss the heating rate and find that shock heating could support radiative loss in the chromosphere. However, the generation mechanism of waves is different in their study. Their work is based on a 2.5-dimensional simulation which includes the Alfvén wave. The transverse motion at the footpoint of the flux tube generates Alfvén wave. The Alfvén wave further generates slow acoustic wave in the flux tube through ponderomotive mode coupling. The acoustic waves finally steepen to shocks and contribute to chromospheric heating. Similar mechanism has also been discussed in Arber et al. (2016) and Wang & Yokoyama (2020) in 1.5-dimensional simulation. In our study, although the heating is obtained through shock dissipation, the mode of waves is different.

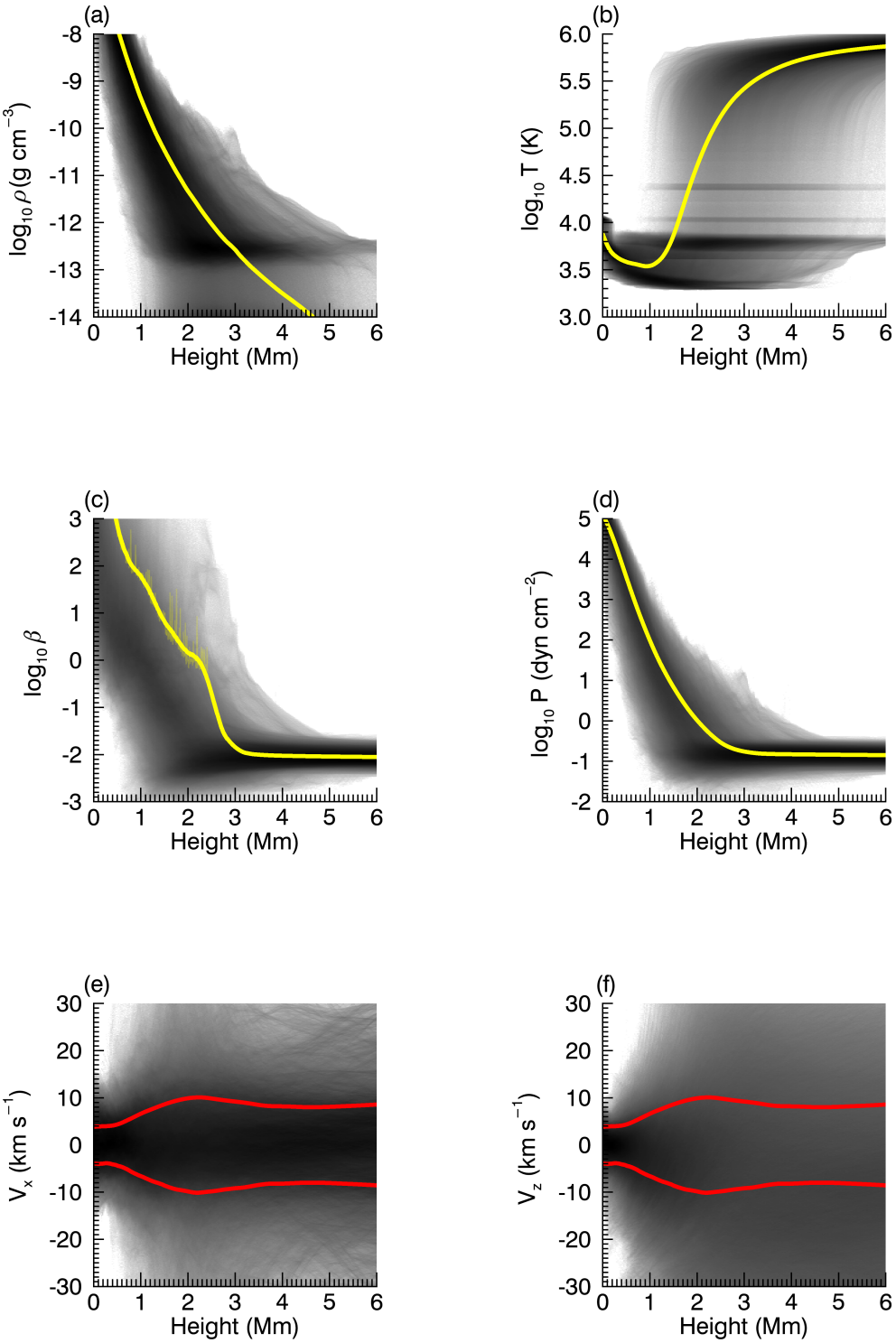

Figure 3.14: The same as Figure 3.3 but for case 20. Vertical structure of the simulation in scale of height. (a): density; (b): temperature; (c): plasma beta; (d): gas pressure; (e): horizontal velocity; (f): vertical velocity. Yellow lines in panel (a) to (d) shows the averaged value. Specifically, in panel (c), the thin yellow line shows the averaged value that is directly calculated from the original data, and the thick yellow line shows the result after being smoothed by a Savitsky-Golay filter. Red lines in panel (e) and (f) show the root mean square of the velocity.

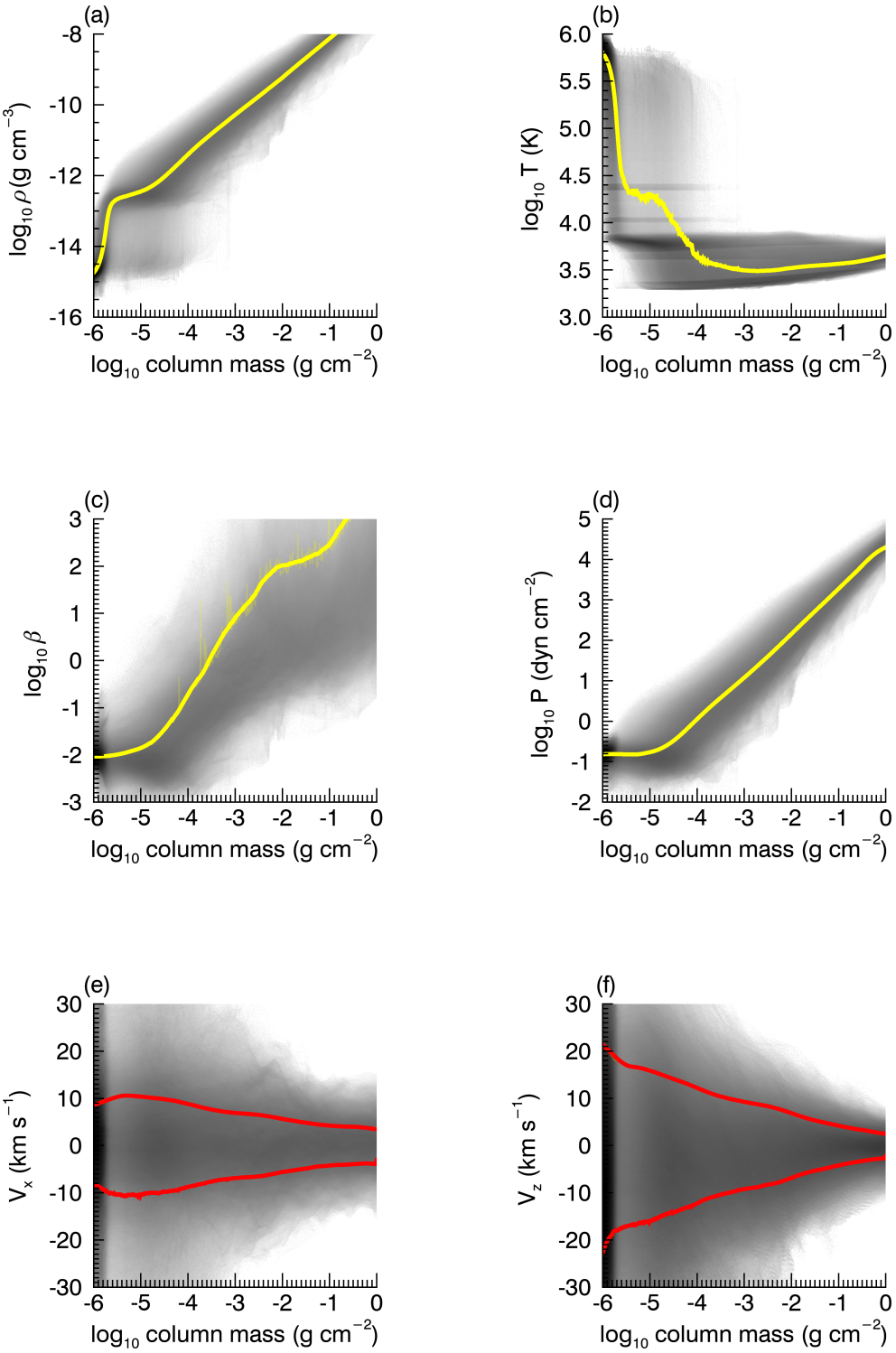

Figure 3.15: The same as Figure 3.4 but for case 20. Vertical structure of the simulation in scale of column mass. (a): density; (b): temperature; (c): plasma beta; (d): gas pressure; (e): horizontal velocity; (f): vertical velocity. Yellow lines in panel (a) to (d) shows the averaged value. Specifically, in panel (c), the thin yellow line shows the averaged value that is directly calculated from the original data, and the thick yellow line shows the result after being smoothed by a Savitsky-Golay filter. Red lines in panel (e) and (f) show the root mean square of the velocity.

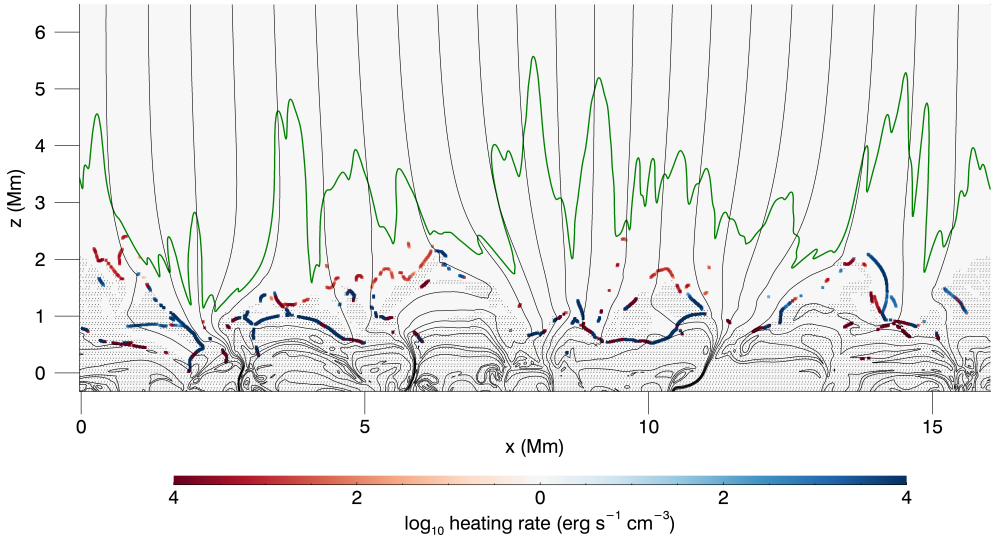

Figure 3.16: The same as Figure 3.2 but for one snapshot of case 20. The green line marks the position of the transition region ($T = 10000$ K). Grey lines are magnetic field lines. The dotted shadow marks the region where sound speed is larger than Alfvén speed. Shocks are identified and the corresponding heating rate is plotted in blue (fast shock) and red (slow shock) color. Only part of the simulation domain in the vertical direction is shown in this figure.

We specifically find the quantitative importance of heating from the fast magnetic wave, which has not been investigated by previous studies.

There are also simulations using two-dimensional realistic setup. However, wave heating is not carefully studied. Martínez-Sykora et al. (2012, 2017) carry on the simulations by using Bifrost code (Gudiksen et al., 2011). Their advantage is that they solve the dynamic hydrogen ionization to include the effect of ambipolar diffusion. They show an example of generation of spicules related to ambipolar diffusion which indicates that ambipolar diffusion is significant in affecting the chromospheric dynamics. We also discuss the ambipolar diffusion in Section 3.5.1.

Our study is limited by the two-dimensional geometry. Transverse Alfvén wave vanishes in the two-dimensional geometry. As a result, we can not evaluate the heating mechanism related to Alfvén waves, including the mode coupling from Alfvén wave to slow acoustic wave scenario. Moreover, Ohmic dissipation could work efficiently at small structures generated by phase mixing (Soler et al., 2019) or turbulence (van Ballegooijen

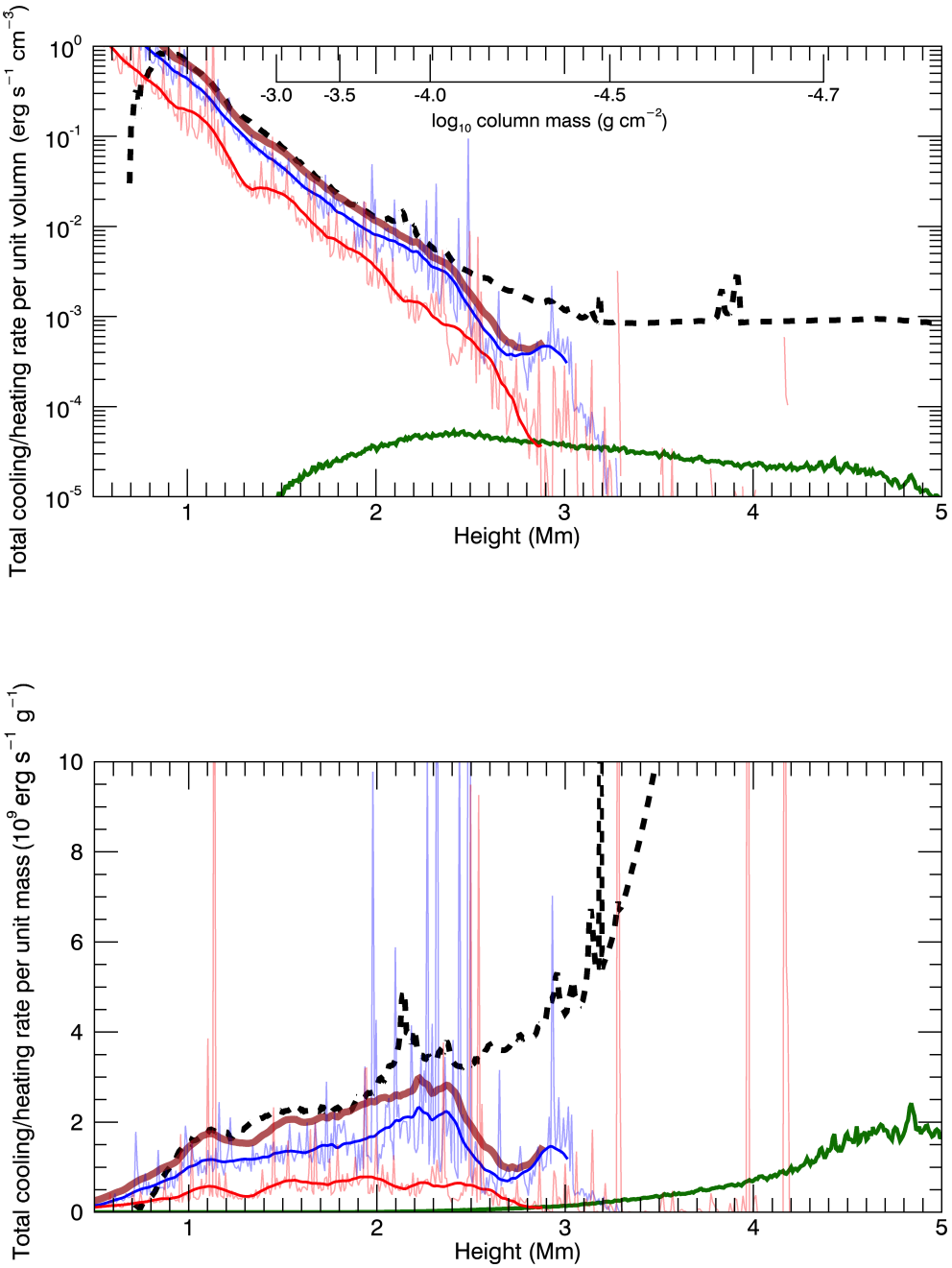

Figure 3.17: The same as Figure 3.8 but for case 20. Heating and radiative loss rates as a function of height. The black dashed line is the total radiative loss rate in the simulation. The blue solid line is the fast wave heating rate. The red solid line is the slow wave heating rate. For blue and red lines, the thin lines with perturbation are the results directly calculated from the simulation while we also smooth the results by a Savitsky-Golay filter and plot them in thick lines. The brown solid line is the total heating rate that includes both fast wave and slow wave heating rate after smoothing. The averaged column mass at each height is shown in the secondary axis. In the upper panel, the heating and cooling rates are shown per unit volume. In the lower panel, the heating and cooling rates are shown per unit mass. The results in the lower panel are calculated from the results in the upper panel and is normalized by the horizontal and temporal averaged density at each height.

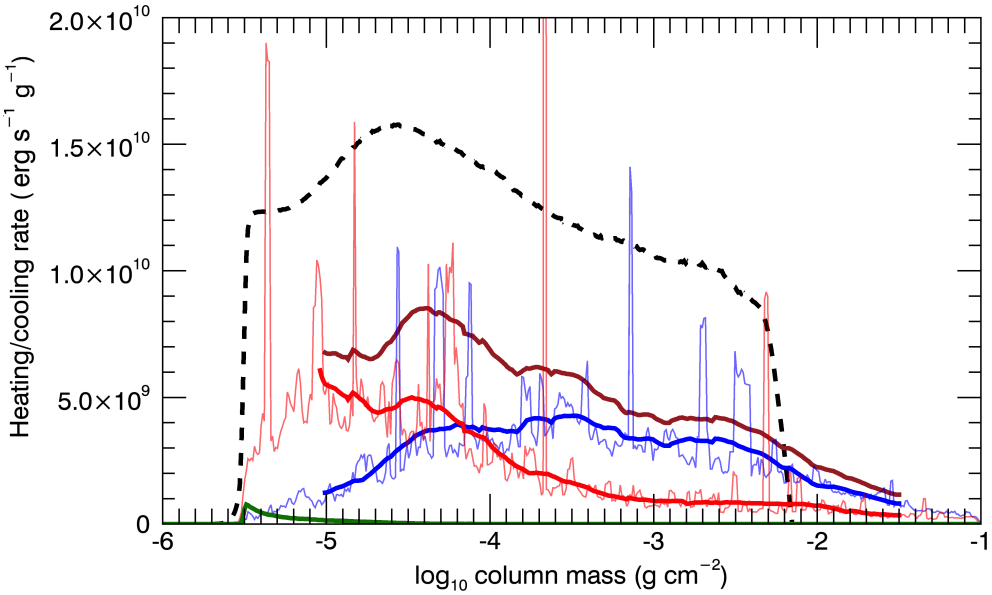

Figure 3.18: The same as Figure 3.9 but for case 20. Heating and radiative loss rate per unit mass as a function of column mass. The black dashed line is the total radiative loss rate in the simulation. The blue solid line is the fast wave heating rate. The red solid line is the slow wave heating rate. For blue and red lines, the thin lines with perturbation are the results directly calculated from the simulation while we also smooth the results by a Savitsky-Golay filter and plot them in thick lines. The brown solid line is the total heating rate that includes both fast wave and slow wave heating rate after smoothing.

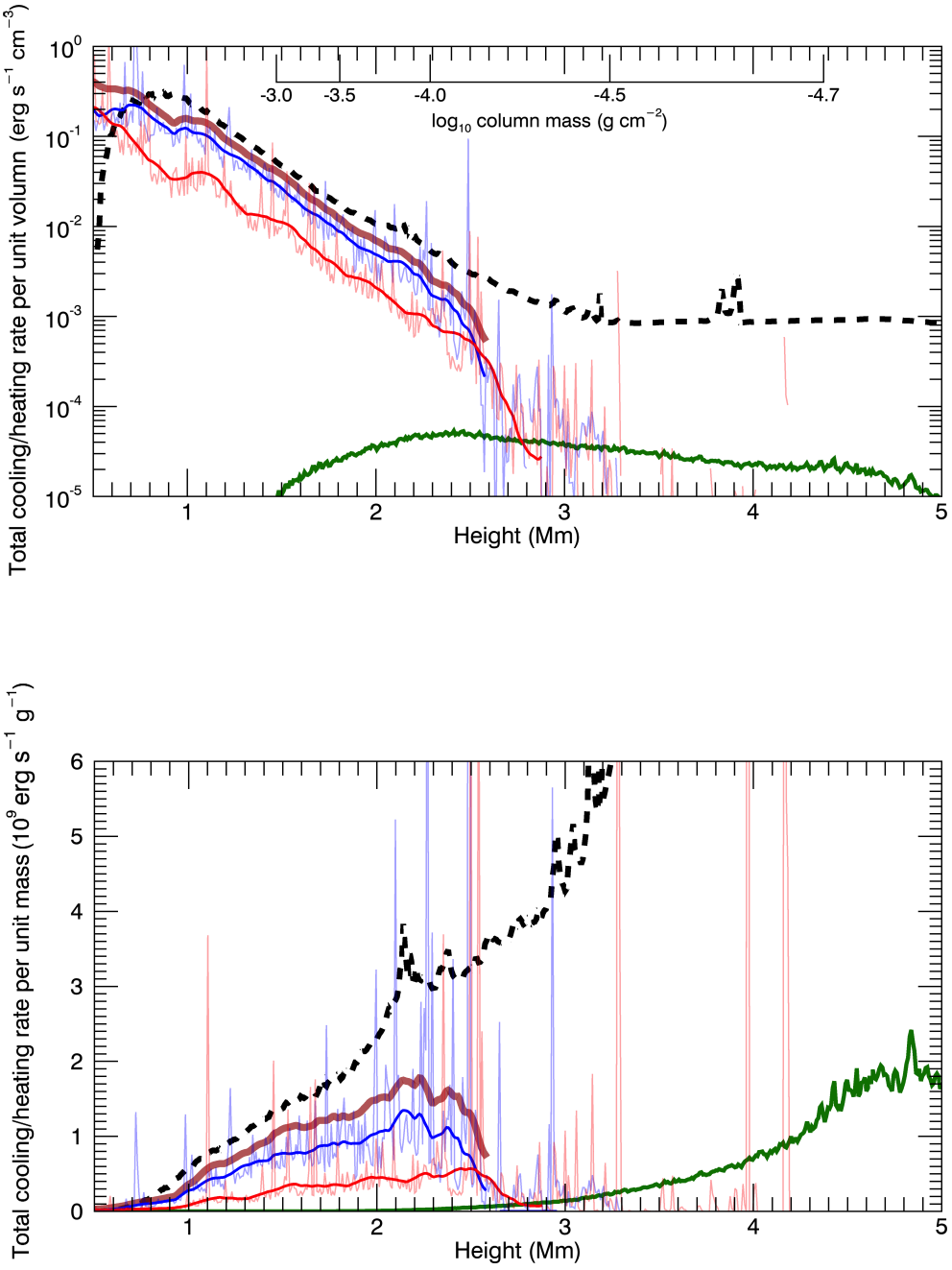

Figure 3.19: The same as Figure 3.17 but for low-beta components only.

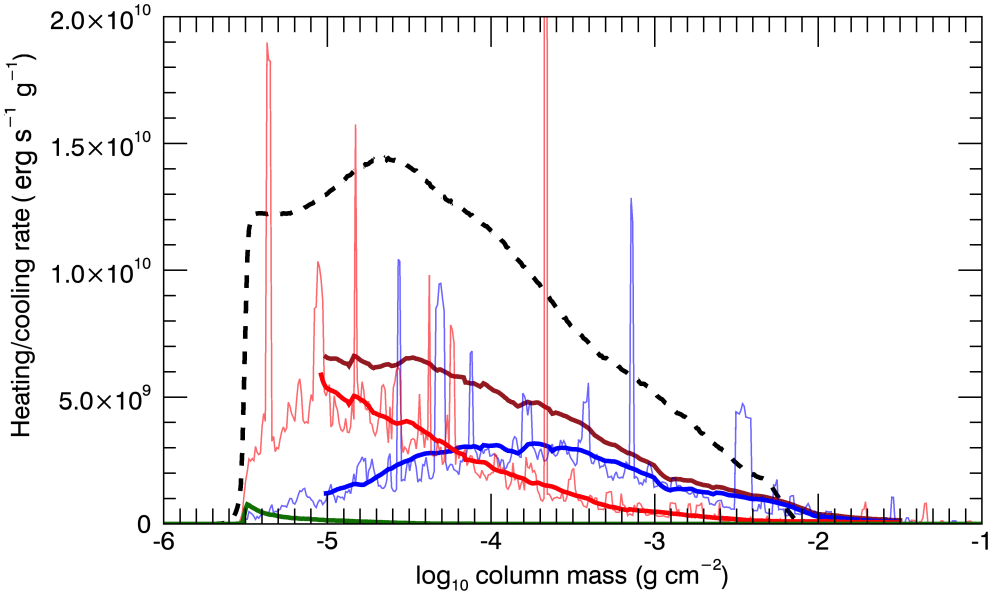

Figure 3.20: The same as Figure 3.18 but for low-beta components only.

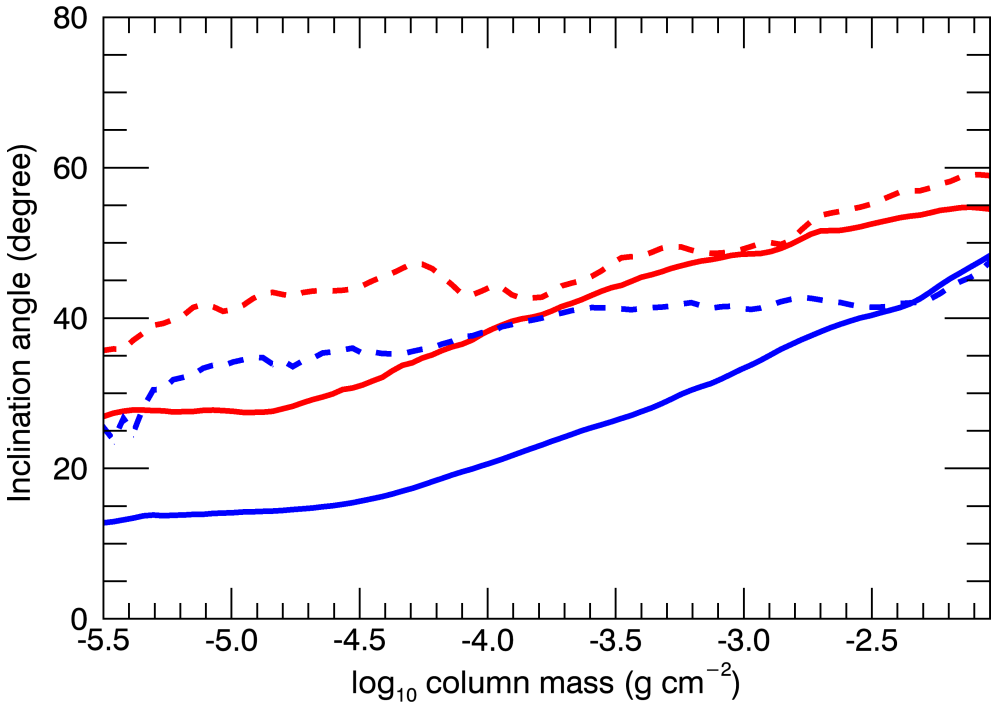

Figure 3.21: Inclination angle of the magnetic field in case 6 (red) and case 20 (blue) as a function of column mass. Dashed lines show the inclination angle selected by the condition that the plasma beta is between 0.5 and 2.

et al., 2011) of Alfveń wave.

3.5.1 Ambipolar diffusion

Our simulation does not include ambipolar diffusion explicitly. However, we could also estimate the potential contribution by ambipolar diffusion to heating as follows. Note that, since the magnetic field is not really dissipated, it is reasonable to assume the following treatment will lead to an overestimation of the ambipolar diffusion heating rate.

The diffusivity of ambipolar diffusion $\eta_{\rm amb}$ is calculated following Khomenko & Collados (2012)

$$\eta_{\rm amb} = \frac{(\rho_{\rm n}/\rho)^2|\mathbf{B}^2|}{(\rho_{\rm i}\nu_{\rm in} + \rho_{\rm e}\nu_{\rm en})4\pi}, \tag{3.1}$$

where $\rho_{\rm i}$, $\rho_{\rm e}$, and $\rho_{\rm n}$ are ion density, electron density, and neutral density, respectively. $\nu_{\rm in}$ is the collision frequency between ion and neutral,

$$\nu_{\rm in} = n_{\rm n}\sqrt{(8k_BT)/(\pi m_{\rm in})}\sigma_{\rm in}. \tag{3.2}$$

$\nu_{\rm en}$ is the collision frequency between electron and neutral,

$$\nu_{\rm en} = n_{\rm n}\sqrt{(8k_BT)/(\pi m_{\rm en})}\sigma_{\rm en}. \tag{3.3}$$

σ is the cross section where $\sigma_{\rm in} = 5 \times 10^{-16}$ cm^2 and $\sigma_{\rm en} = 1 \times 10^{-16}$ cm^2. $n_{\rm n}$ is the number density of neutrals. The heating rate by ambipolar diffusion $Q_{\rm amb}$ is calculated by

$$Q_{\rm amb} = \frac{4\pi}{c^2}\eta_{\rm amb}\mathbf{J}^2. \tag{3.4}$$

We also estimate the ambipolar diffusion heating timescale by

$$t_{\rm amb} = e_{\rm int}/Q_{\rm amb}. \tag{3.5}$$

The ionization degree is critical for calculating the diffusivity of ambipolar diffusion. LTE approximation will lead to a severe underestimation of ionization degree, especially for the low-temperature regions behind the shock fronts that are affected by adiabatic cooling. The plasma ionizes efficiently when the shock front passes. However, the time cadence between two successive shocks is not long enough for recombination to complete, leading to the result that the ionization degree is much higher than the ionization degree calculated from LTE assumption (see Figure 8 in Carlsson & Stein, 2002). As a result, we do not use LTE ionization degree in this estimation. Instead, the ionization degree is determined by the empirical fitting function, which is the same treatment as that used in chromospheric radiative loss (see Section 2.2). Moreover, since the empirical fitting function does not extend to the low temperature region, we set floor values for the ionization degree. We choose the floor value as a function of column mass (see the solid line in Figure 3.22). This floor value is determined from simulation including the dynamic ionization (Carlsson et al., 2016). From the simulation result of Carlsson et al. (2016), we sort the ionization degree at a fixed column mass. The ionization degree at the position of lowest 10 percent is used as our floor value. For comparison, the floor value and the averaged ionization degree in the simulation result of Carlsson et al. (2016) as a function of column mass are shown in Figure 3.22.

The result of diffusivity, heating rate, and heating timescale is shown in Figure 3.23. We also plot the time and horizontal averaged ambipolar diffusion heating rate in Figure 3.24. It is shown that although the ambipolar diffusion has the potential to heat the chromospheric plasma near the transition region (Figure 3.23), the spatial and time averaged heating rate is much smaller for supporting chromospheric radiative loss (Figure 3.24). In most of the regions in the chromosphere, the ambipolar diffusion heating time scale is longer than 1000 s (shown in the red color in the middle panel of Figure 3.23), which is one order larger than the typical radiative loss time scale ($\sim$100 s).

We also compare our result of ambipolar diffusion heating rate with the result in

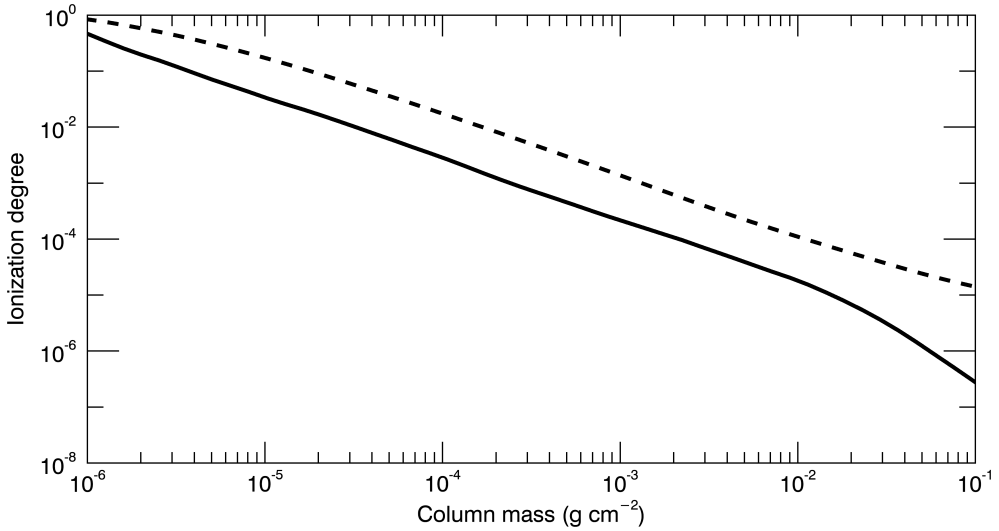

Figure 3.22: Solid line shows the floor value used in evaluation of the ionization degree as a function of column mass. The dashed line shows the averaged ionization degree. Data derived from the simulation introduced in Carlsson et al. (2016).

Martínez-Sykora et al. (2017) who perform a two-dimensional simulation with ambipolar diffusion explicitly included. Their minimum grid size is 14 km, which is larger than that used in our simulation (8.5 km). They focus on the role of ambipolar diffusion in the generation of spicules. Although the contribution of ambipolar diffusion to chromospheric heating is not specifically discussed in this study, it shows that the heating rate could reach to 10^{10} erg s^{-1}g^{-1} locally. Recall that the typical required heating rate is 4.9×10^{9} erg s^{-1}g^{-1}. The effect of ambipolar diffusion is large enough to affect the chromospheric dynamics locally. However, if averaged over time, the averaged ambipolar diffusion heating rate is smaller than the typical radiative loss rate (shown in the orange line in Figure 3.24).

3.5.2 Discussion on the shock detection procedure

As described in Section 2.3, we identify the shock regions by

$$\nabla \cdot \mathbf{V} \leq -c_{\rm th}(C_{\rm s}/\Delta x). \tag{3.6}$$

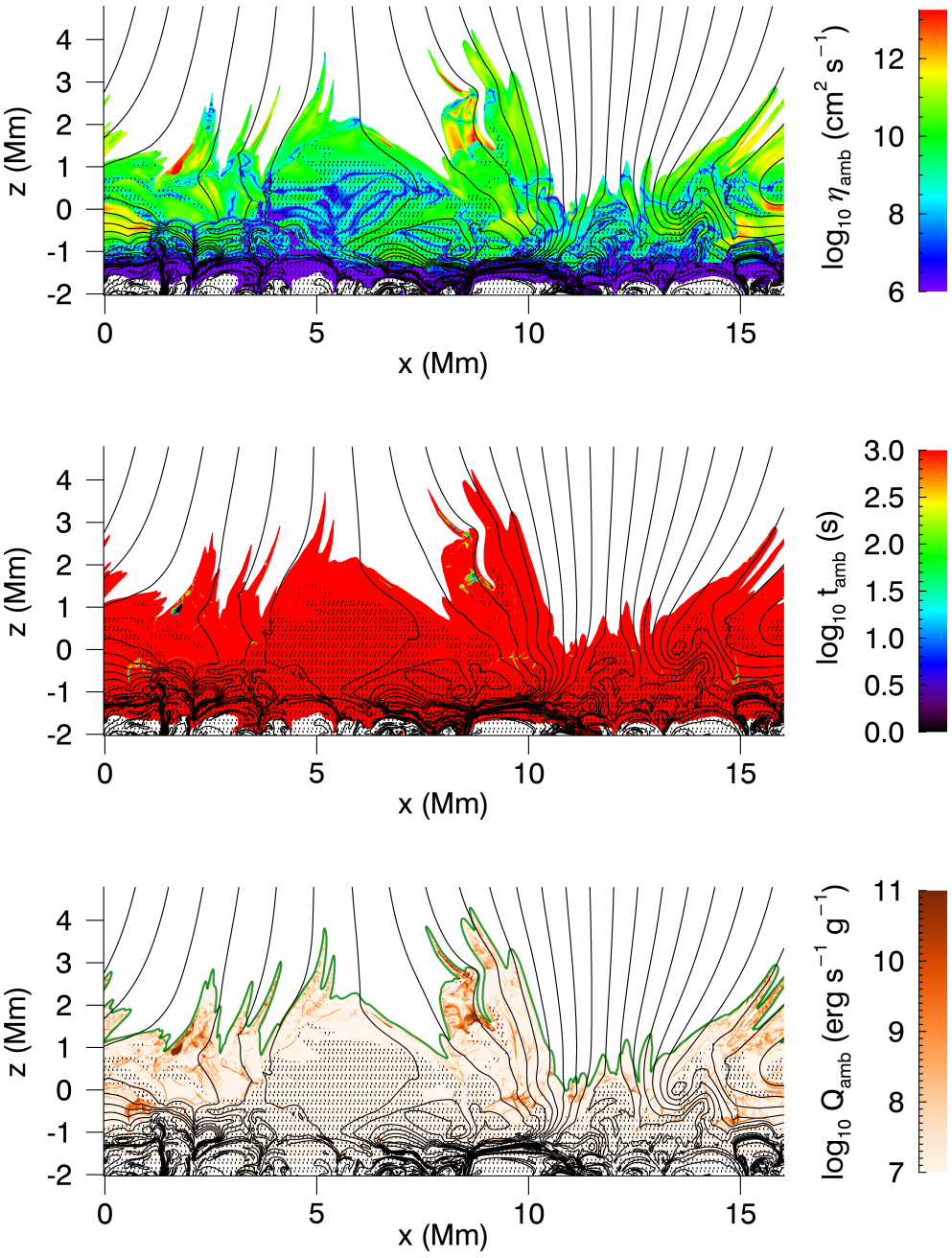

Figure 3.23: Upper panel: ambipolar diffusion diffusivity. Middle panel: ambipolar diffusion heating timescale. Lower panel: ambipolar diffusion heating rate. In all panels, grey lines are magnetic field lines. Dotted shadows mark the region where sound speed is larger than Alfvén speed. Green line in the lower panel marks the position of the transition region.

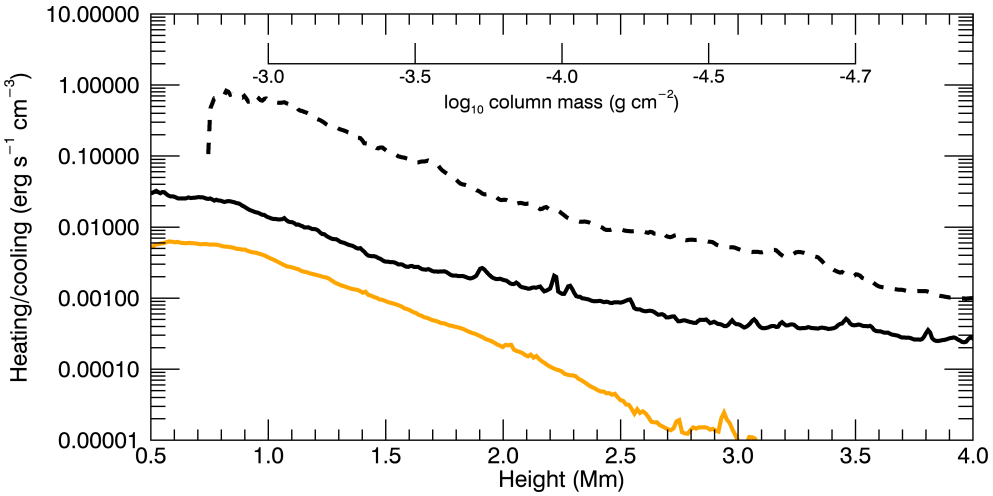

Figure 3.24: Comparison between radiative loss rate and the potential ambipolar diffusion heating rate. Dashed line shows the radiative loss rate. The thick solid black line shows the potential ambipolar diffusion heating rate. Averaged column mass as a function of height is shown in the secondary axis. As a comparison, the averaged ambipolar diffusion heating rate in Martínez-Sykora et al. (2017) is shown in the orange line.

The non-dimensional value for $c_{\rm th}$ is required to be small enough for including weaker shocks while large enough to exclude compression from linear propagation of waves. For this purpose, we plot the occurrence frequency distribution of $\nabla \cdot \mathbf{V}/(C_{\rm s}/\Delta x)$ in Figure 3.25. For linear propagating waves, $\nabla \cdot \mathbf{V}/(C_{\rm s}/\Delta x)$ is expected to be symmetric in the positive and negative sides. The actual distribution is asymmetric due to the formation of shocks. This enhancement can be captured by comparison with the turn-up of the positive part to the negative side (dotted line). From this comparison, we find that the threshold used in our study ($c_{\rm th} = 1/4$) is large enough to exclude the compression from the linear propagation of waves. A softer threshold will include weaker shocks as well as the possibility of overestimation of heating rate because compression in linear propagating waves may be included. On the contrary, a stricter threshold will underestimate the heating rate because weak shocks are not included. The comparison between heating rate with different thresholds and the radiative loss rate is shown in Figure 3.26. It is shown that a stricter threshold ($c_{\rm th} = 1/3$) do not considerably affect the energy balance between shock heating and radiative loss.

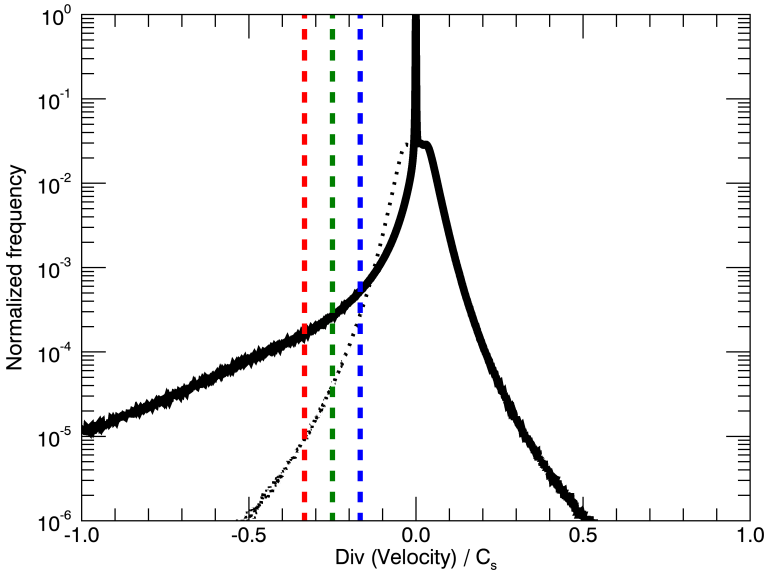

Figure 3.25: The thick black line is the distribution of normalized occurrence frequency of $\nabla \cdot \mathbf{V}/(C_{\rm s}/\Delta x)$. The dotted black line is the turn-up of the positive part to the negative side. Vertical dashed red, green, and blue lines mark the threshold values with $c_{\rm th} = \frac{1}{3}$, $\frac{1}{4}$, and $\frac{1}{6}$ respectively.

3.6 Predicting the observation

Previous observational researches use the Doppler shift as an indicator of the velocity perturbation in the chromosphere. However, it is difficult to determine the mode of the waves because current observation can not provide information about the perturbation of the magnetic field in the chromosphere. Observation of the chromospheric magnetic field is one of the targets of the next generation telescopes such as the Daniel K. Inouye Solar Telescope (DKIST; Rimmele et al., 2020) and the Chinese Giant Solar Telescope (CGST; Deng & CGST Group, 2011). For example, the characteristic sensitivity of the vertical magnetic field measurement in the chromosphere is designed to reach 1 G with a time resolution of 10 s (Deng & CGST Group, 2011). We plot the time slice of the vertical velocity field and the vertical magnetic field with detected fast shock waves in Figure 3.27. The perturbation of magnetic field and vertical velocity in the range from $x = 3.5$ Mm to $x = 4.5$ Mm is also shown in Figure 3.28, where the height is fixed at $z = 1.37$ Mm. For the time slice, a filter is applied to mimic the observation with a spatial resolution of 85

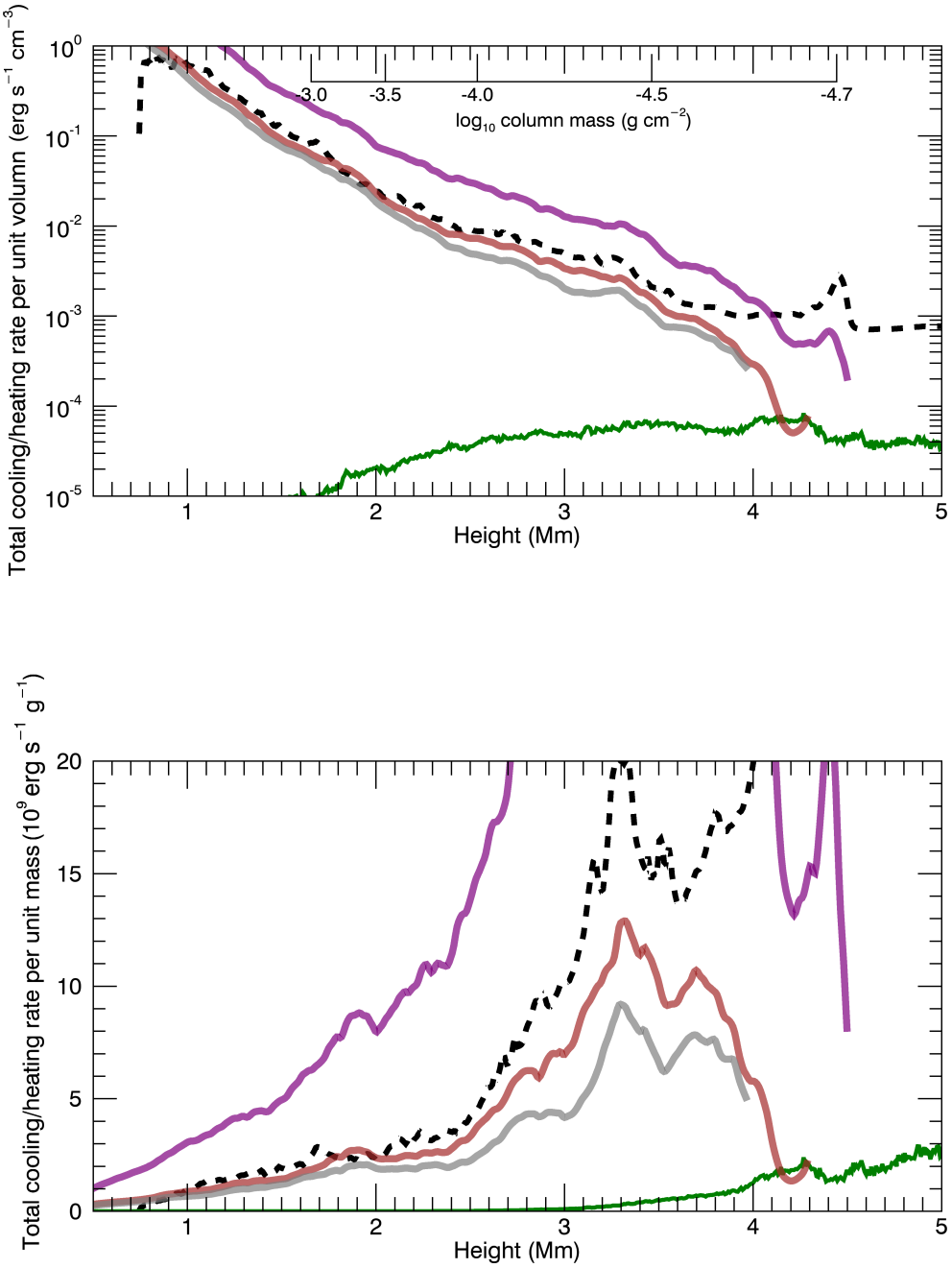

Figure 3.26: Comparison between the shock heating rates (solid lines) and radiative loss rate (dashed line) per unit volume (upper panel) and per unit mass (lower panel) among different threshold values $c_{\rm th}$. Grey, brown, and purple lines are shock heating rates for $c_{\rm th} = 1/3$, $1/4$, and $1/6$, respectively. The green line is the heating rate from heat conduction.

Km and a time resolution of 40 s. We choose to plot the vertical velocity and the vertical magnetic field because the vertical velocity could be directly observed from the Doppler shift of the spectral lines. The sensitivity of vertical magnetic field is also higher than that of the horizontal magnetic field.

In the velocity panels, the structure of horizontal stripes is shown. As the fast waves propagate in a manner of expanding arcades, the strongest perturbation of the vertical velocity appears at the top of the arcade. The horizontal stripes reflect the perturbation of vertical velocity that is close to the top of the arcade. However, in the vertical magnetic field panel, the structure of vertical stripes appeared. This is because the magnetic field close to the top of the arcade is in the horizontal direction. On the contrary, compression of vertical magnetic field appears at the sides of the arcade.

In the filtered plot of the vertical magnetic field (lower-right panel of Figure 3.27), it is shown that the structure of vertical stripes is still detectable. The intensity of the magnetic field perturbation could be as large as 10–20 G. It is suggested that such signal of fast wave is hopefully to be detected by next generation solar telescopes. Finally, we have to emphasize that the formation of spectral lines in the chromosphere is complicated. For example, the existence of shocks will affect the formation heights of spectral lines, which need to be taken into consideration when comparing with observations. We plan to carry on spectral line synthesizing study to provide a better prediction of observation in the future works.

3.7 Summary

We carry on two-dimensional simulations for estimating the heating rate of different modes of waves. The results show that the shock heating is well balanced with the radiative loss in the chromosphere. Fast magnetic wave is significant in heating the low-

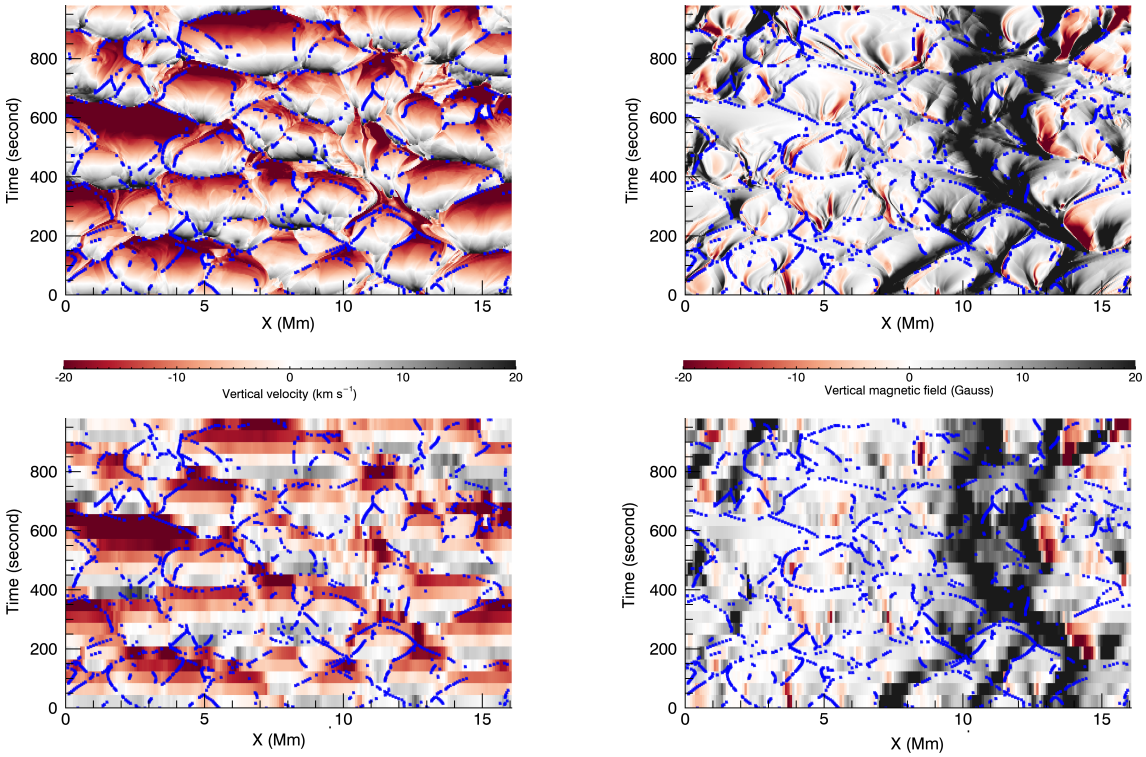

Figure 3.27: Upper-left: the time slice of the vertical velocity of the simulation results. Upper-right: the time slice of the vertical magnetic field of the simulation results. Lower-left: the time slice of the vertical velocity of the simulation results after applying the filter. Lower-right: the time slice of the vertical magnetic field of the simulation results after applying the filter. The filter mimics the observation with a spatial resolution of 85 km and a time resolution of 40 s. In all the panels, detected fast shocks are shown in blue color. For all the panels, the height is fixed at 1.37 Mm.

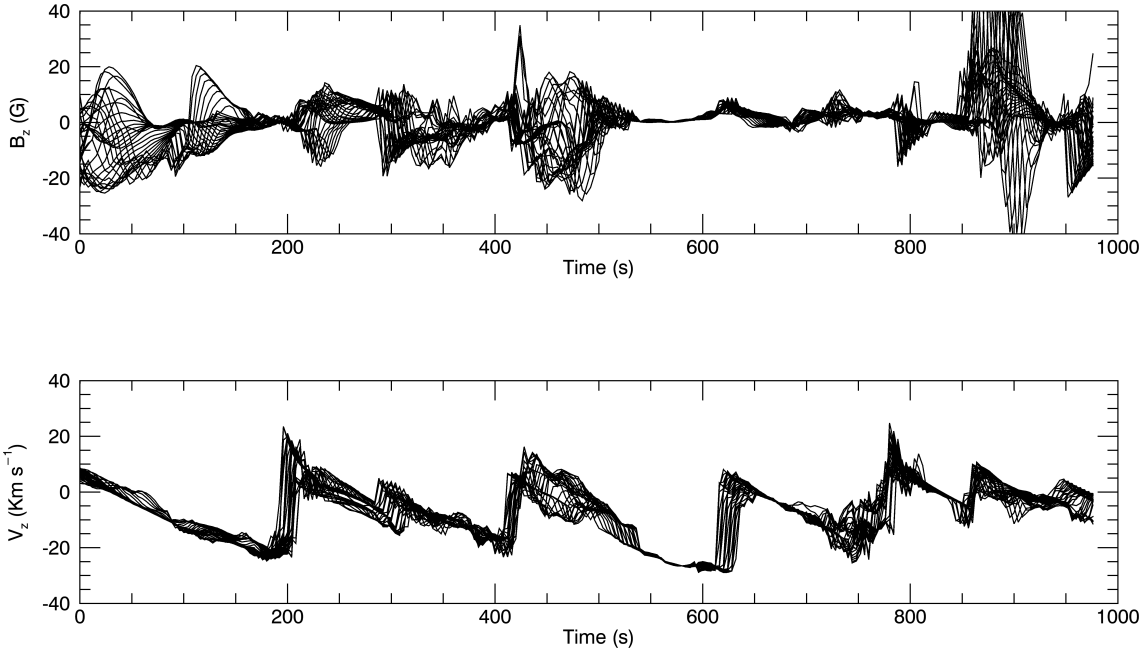

Figure 3.28: Upper panel: vertical magnetic field B_z. Lower panel: vertical velocity V_z. The plot range is from $x = 3.5$ Mm to $x = 4.5$ Mm with a fixed height $z = 1.37$ Mm.

beta region of the chromosphere. The low-beta fast magnetic wave comes from mode conversion of the fast acoustic wave in the high-beta region. It is expected that the ambipolar diffusion does not considerably heat the chromosphere in this model. Magnetic field structure affects the role of different modes in heating the low-beta chromosphere. For a stronger magnetic field, a smaller attacking angle is in favor of mode transmission, which leads to a larger heating rate from the slow acoustic wave than the fast magnetic wave. We made prediction plots of the chromospheric magnetic field. It is expected that the structure of vertical stripes will appear in the time slice plot of the observation of the vertical magnetic field. Such signal of fast wave is hopefully to be detected by next generation solar telescopes.

Chapter 4

Three-dimensional simulation

4.1 Introduction

Our two-dimensional model helps understanding the physics of the waves, especially the mode conversion and transmission but there are some disadvantages. For example, the amplitude of waves can be overestimated in two-dimensional simulation especially for the fast waves as they propagate as an expanding sphere in the nature of three-dimensional geometry. Moreover, Alfvén wave vanishes in the two-dimensional simulation and it could have two effects. The first one is that there is no presence of mode coupling from Alfvén wave to slow acoustic wave in flux tubes, which could lead to an underestimate of the contribution of heating by the slow acoustic wave. The other effect is that the role of turbulence and phase mixing of Alfvén waves are not taken into account. It is expected that the presence of non-linear mode coupling, as well as the Alfvén wave turbulence, could reduce the percentage of heating contributed from fast magnetic shock wave in the three-dimensional model compared with the two-dimensional model. We are motivated by examining the validity of our main conclusion in the three-dimensional geometry. Our main conclusion is that fast magnetic wave is significant in heating the low-beta chro-

mosphere. This conclusion is obtained by the two-dimensional studies in the previous chapter.

4.2 Simulation settings

Basic settings have already been described in Chapter 2 and will not be repeated here. The three-dimensional simulation domain is a 9 Mm $\times$ 9 Mm $\times$ 15 Mm cube. We define the x and y directions are the horizontal directions and the z direction is the vertical direction. In the z direction, the height extends from -2 Mm below the bottom of the photosphere to 13 Mm in the corona. The grid size is 25 km $\times$ 25 km $\times$ 25 km. This grid size is not as fine as that in the two-dimensional simulation but it is still much smaller than the typical wavelength in the chromosphere and the pressure scale height. The initial magnetic field is homogeneous with only z component and its intensity is 6 G, which is the same as the typical case in the two-dimensional simulation. Our analysis includes 1000 s of solar time which is one order larger than the typical dynamic timescale of the chromosphere. Threshold value $c_{\rm th}$ is chosen to be 0.4 in the three-dimensional simulation based on the same method described in Section 3.5.2.

4.3 Results

4.3.1 Structure of the atmosphere

We plot the vertical atmospheric structure as a function of height and column mass in Figure 4.1 and Figure 4.2. In the chromosphere both horizontal velocity and vertical velocity is smaller than that in the two-dimensional simulation (see the lowest two panels of Figure 4.2 and 3.4). The difference from the two-dimensional simulations is probably caused by

a combination of effects of the reduction of radiative damping with the weaker strength of shock waves and the three-dimensional dispersion of waves (Iijima, 2016). The geometry effect makes the waves weaker in three-dimensional geometry. On the other hand, radiative damping works to close the gap as the weaker wave in three-dimensional geometry suffers less from radiative damping. The combination of these two effects determines the difference of velocity distribution between two-dimensional and three-dimensional geometry.

A quick look of one snapshot of the simulation results is shown in Figure 4.3. It is shown that a strong magnetic flux tube is formed. Tall spicules form in the flux tube (Figure 4.4). At the photosphere, the magnetic field intensity in the flux tube could reach larger than 1000 G. Starting from the bottom, we display the distribution of temperature, velocity, and magnetic field in the horizontal planes at the bottom of the photosphere (Rosseland mean opacity equals unity, Figure 4.5), lower chromosphere ($z = 0.66$ Mm, Figure 4.6), middle chromosphere ($z = 1.0$ Mm, Figure 4.7), higher chromosphere ($z = 2.0$ Mm, Figure 4.8), and tall spicules ($z = 4.0$ Mm, Figure 4.9). At the bottom of the photosphere (Figure 4.5), convection cells can be clearly seen by the hotter upflow in the center of cells and cooler downflow at the boundary of cells. In the lower chromosphere ($z = 0.66$ Mm, Figure 4.6), shocks start to develop. At $z = 1.0$ Mm (Figure 4.7), the shock fronts can be identified by the temperature structure. Compression of magnetic field close to the shock front could also be observed. At $z = 2.0$ Mm (Figure 4.8), part of regions at this height have been occupied by the coronal plasma. Signal of shock waves becomes obscure. On the other hand, chromospheric plasma shows a pattern of torsional motion. At $z = 4.0$ Mm (Figure 4.9), most of the regions at this height belong to the corona. Chromospheric plasma only exist in the tall spicules.

A flux tube forms at $(x, y) = (2.5, 5.5)$ Mm, which is indicated by the stronger vertical magnetic field that is visible at different heights. This flux tube is associated with tall spicules. The tall spicules are driven by the Lorentz force of the strongly entangled

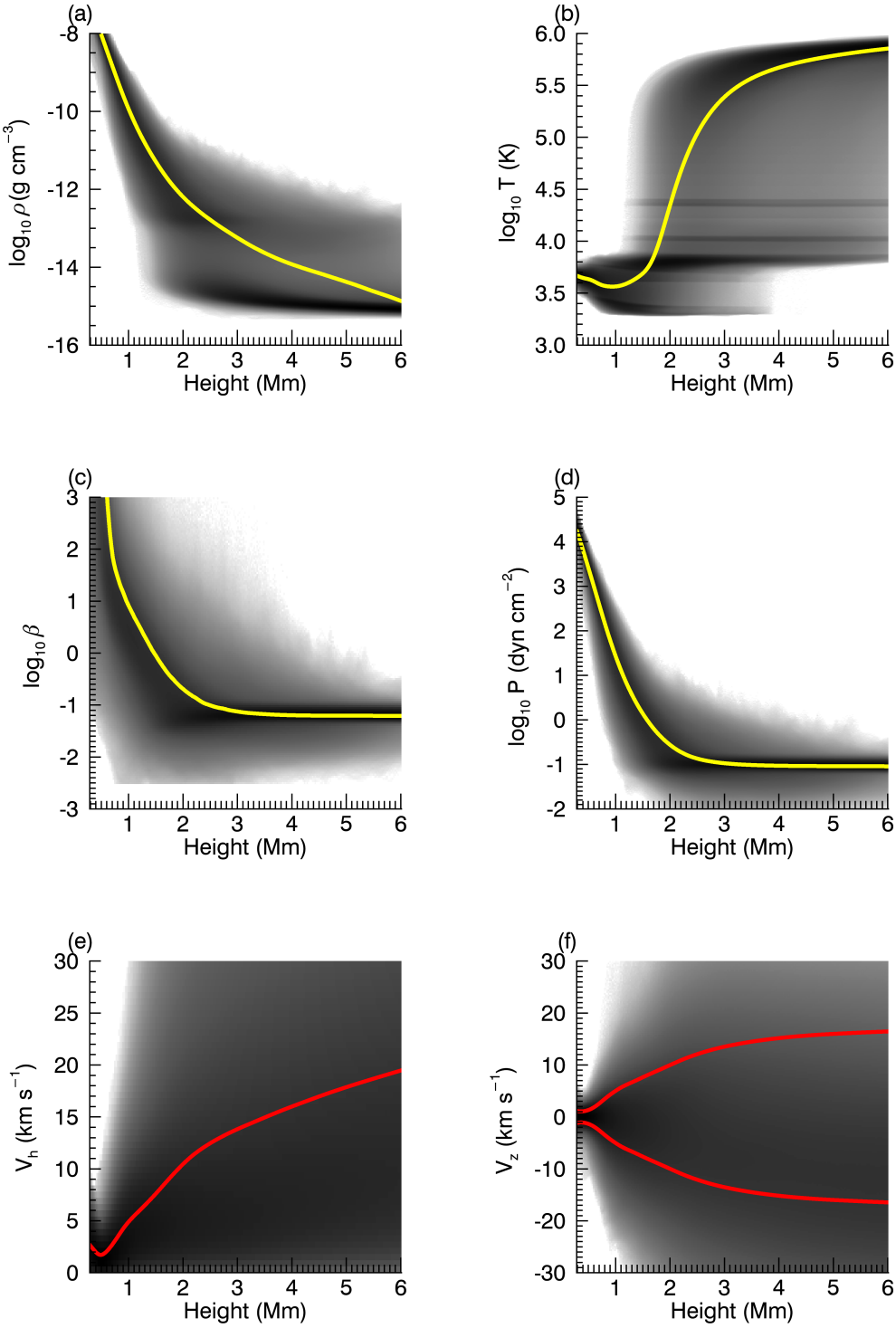

Figure 4.1: Vertical structure of the simulation in the scale of height. (a): density; (b): temperature; (c): plasma beta; (d): gas pressure; (e): horizontal velocity; (f): vertical velocity. Yellow lines in panel (a) to (d) show the averaged value. Red lines in panel (e) and (f) show the root mean square of the velocity.

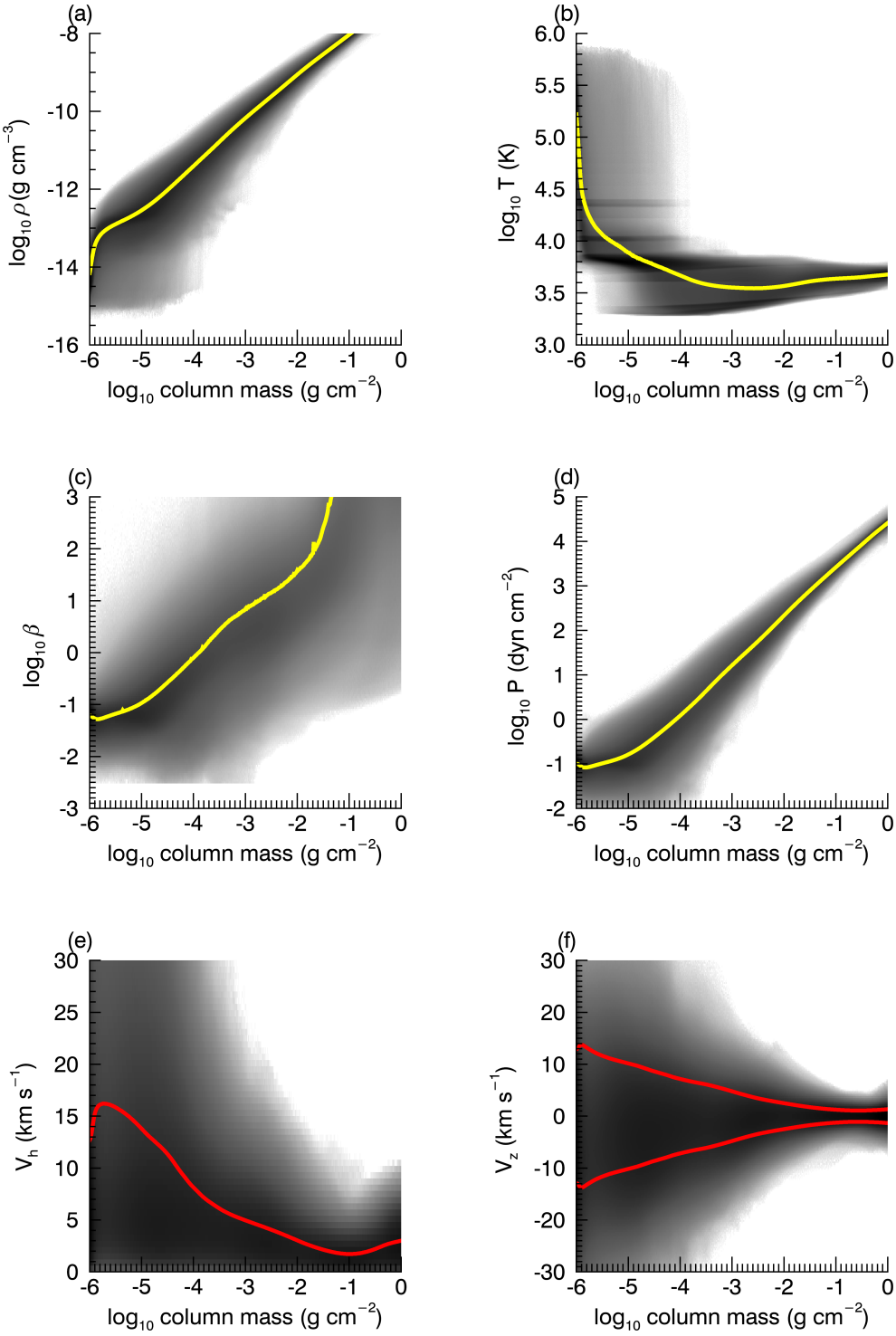

Figure 4.2: Vertical structure of the simulation in the scale of column mass. (a): density; (b): temperature; (c): plasma beta; (d): gas pressure; (e): horizontal velocity; (f): vertical velocity. Yellow lines in panel (a) to (d) show the averaged value. Red lines in panel (e) and (f) show the root mean square of the velocity.

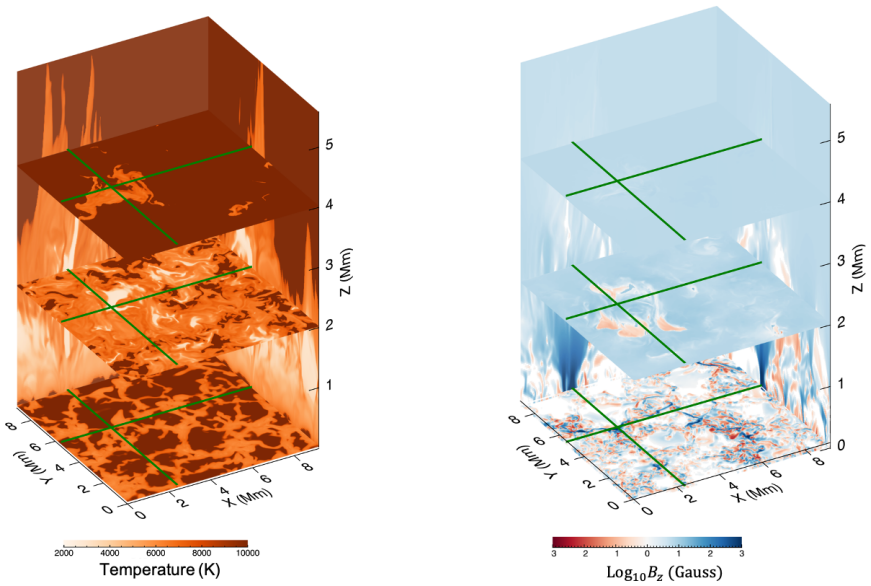

Figure 4.3: Overview of one snapshot of the simulation results. Left panel: temperature. Right panel: vertical magnetic field in log scale. Red color shows negative value. Blue color shows positive value. Green lines on both panels mark the position of the vertical slices.

chromospheric magnetic field. One evidence is the negative magnetic patches (panel (d) in Figure 4.8) associated with strong horizontal magnetic field (Panel (c) in Figure 4.8). As the magnetic field lines drag the chromospheric plasma upwards, the dragged heavy plasma deforms the magnetic field lines, which produces negative magnetic patches and strong horizontal fields. The formation mechanism of tall spicules inside a flux tube has been well discussed in Iijima (2016) and Iijima & Yokoyama (2017).

4.3.2 Shock identification and heating in the chromosphere

Snapshots of the shock identification results are shown from Figure 4.10 to Figure 4.12. The shock structures behave more fragmented than two-dimensional case. The reason for more fragmented detected shocks is technical. The three-dimensional simulation has a

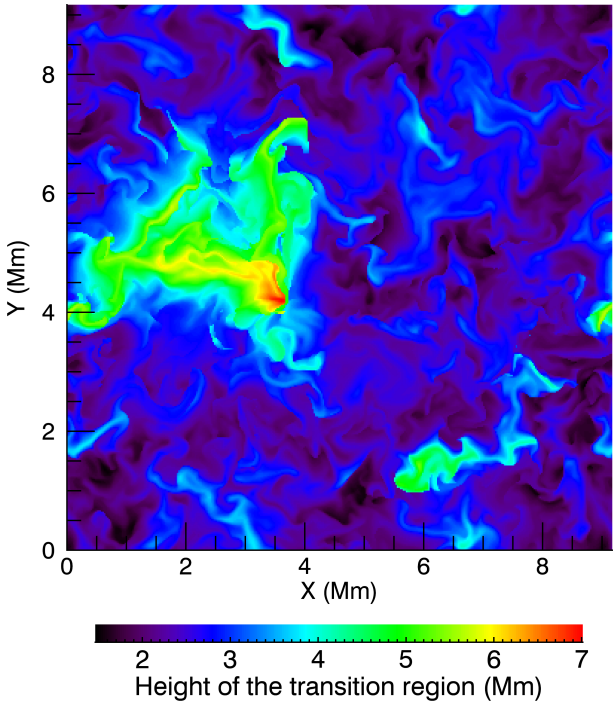

Figure 4.4: One snapshot of the height of the transition region identified by $T = 10000$ K.

lower resolution and the thickness of shocks in the simulation is larger. Weaker shocks can be filtered out by using the threshold value. On the other hand, the amplitude of waves is smaller in three-dimensional case. As a result, a larger number of weaker shocks can not be detected, leading to a more fragmented structure in three-dimensional case.

The energy balance for the low-beta chromospheric plasma is shown in Figure 4.13. Figure 4.13 shows that our previous result (Figure 3.10) that fast magnetic wave is significant for heating the low-beta chromosphere is still valid in the three-dimensional simulation. Especially, below $z = 1.6$ Mm, fast magnetic wave heating is larger than slow acoustic wave heating. What is different from the results of our two-dimensional simulation is that the 3D result shows that fast magnetic wave heating is larger than slow acoustic wave heating only in a limited range while in two-dimensional simulation, fast magnetic wave heating is always larger than slow acoustic wave heating. We will briefly discuss this difference in Section 4.4. At a higher position (higher than $z = 3$ Mm), the energy balance between heating and cooling does not satisfy. Probably this is because of

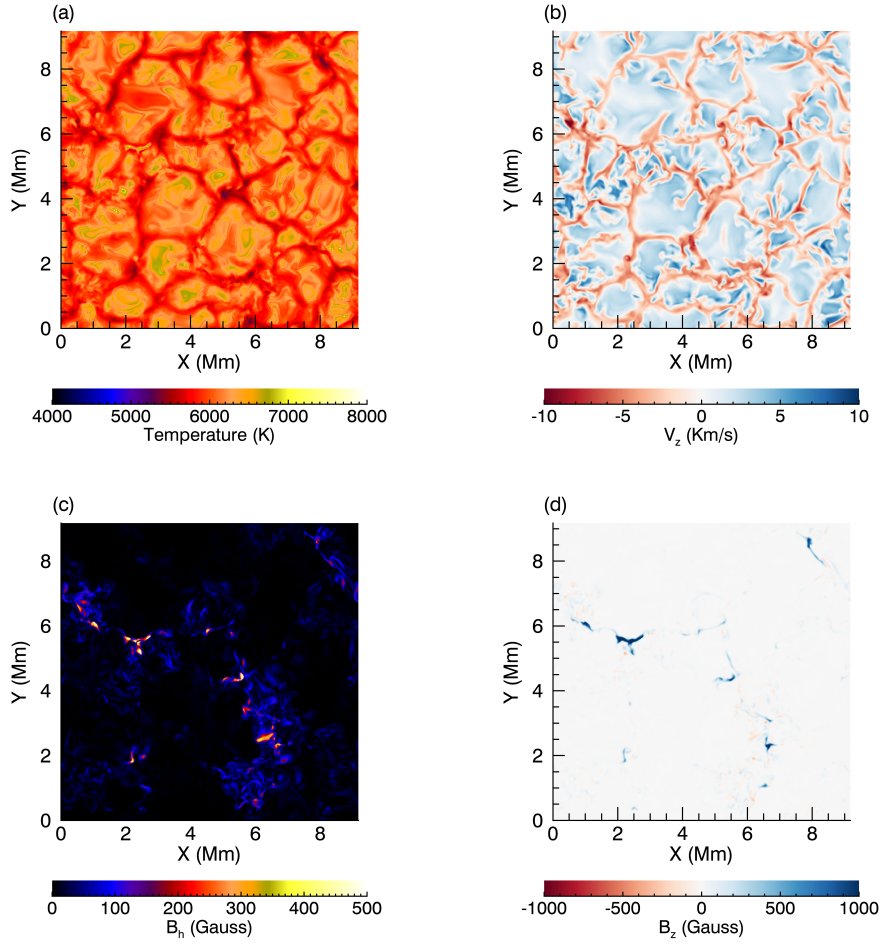

Figure 4.5: One snapshot of the distribution of (a): temperature, (b): vertical velocity, (c): horizontal magnetic field, and (d): vertical magnetic field at the height where Rosseland mean opacity equals unity.

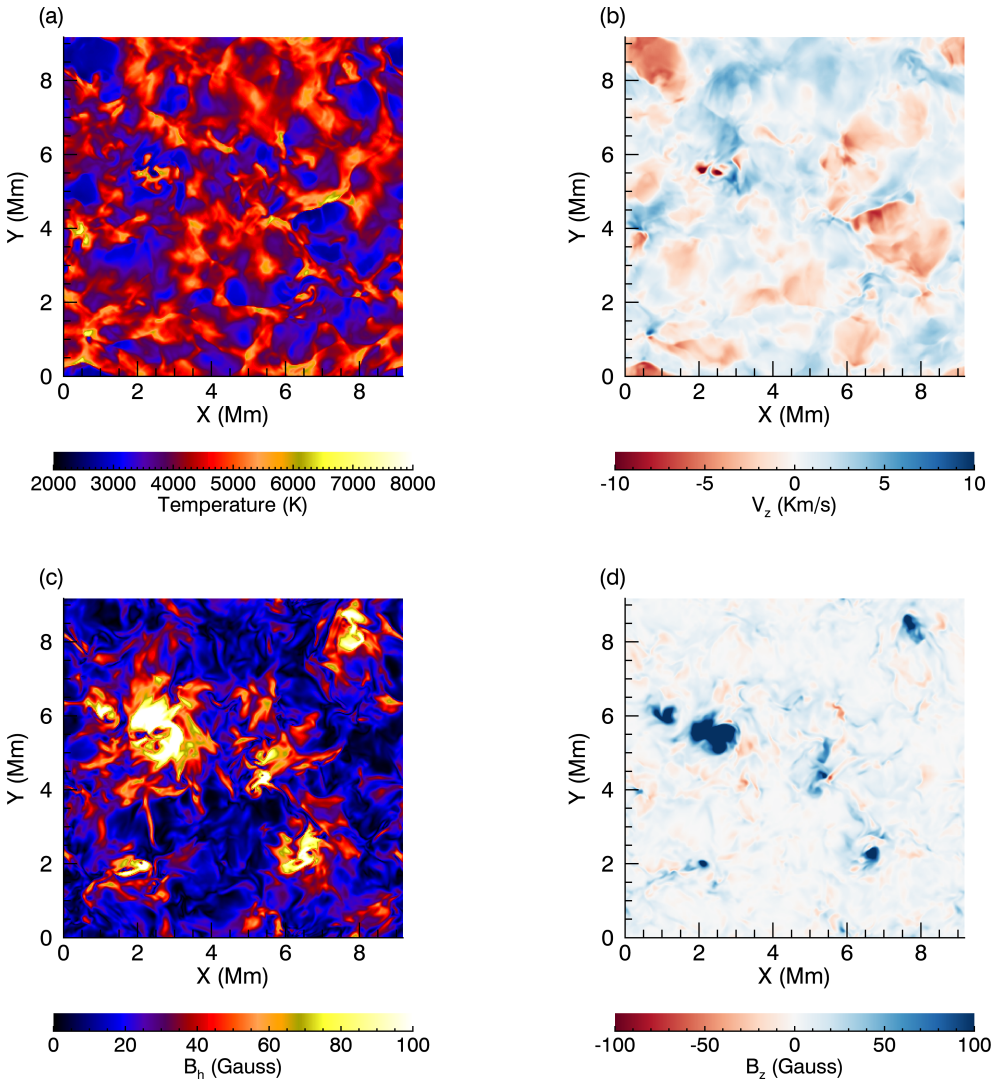

Figure 4.6: One snapshot of the distribution of (a): temperature, (b): vertical velocity, (c): horizontal magnetic field, and (d): vertical magnetic field at $z = 0.66$ Mm.

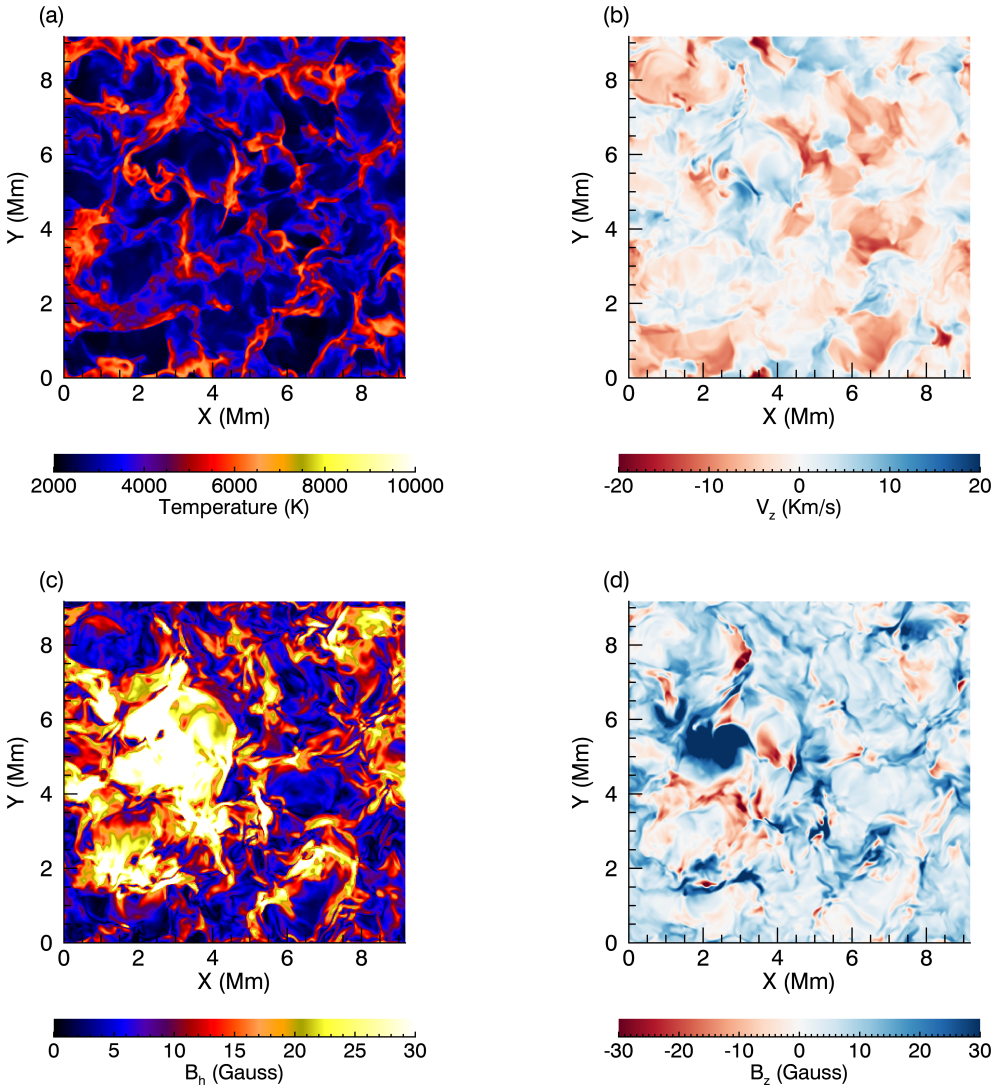

Figure 4.7: One snapshot of the distribution of (a): temperature, (b): vertical velocity, (c): horizontal magnetic field, and (d): vertical magnetic field at $z = 1.0$ Mm.

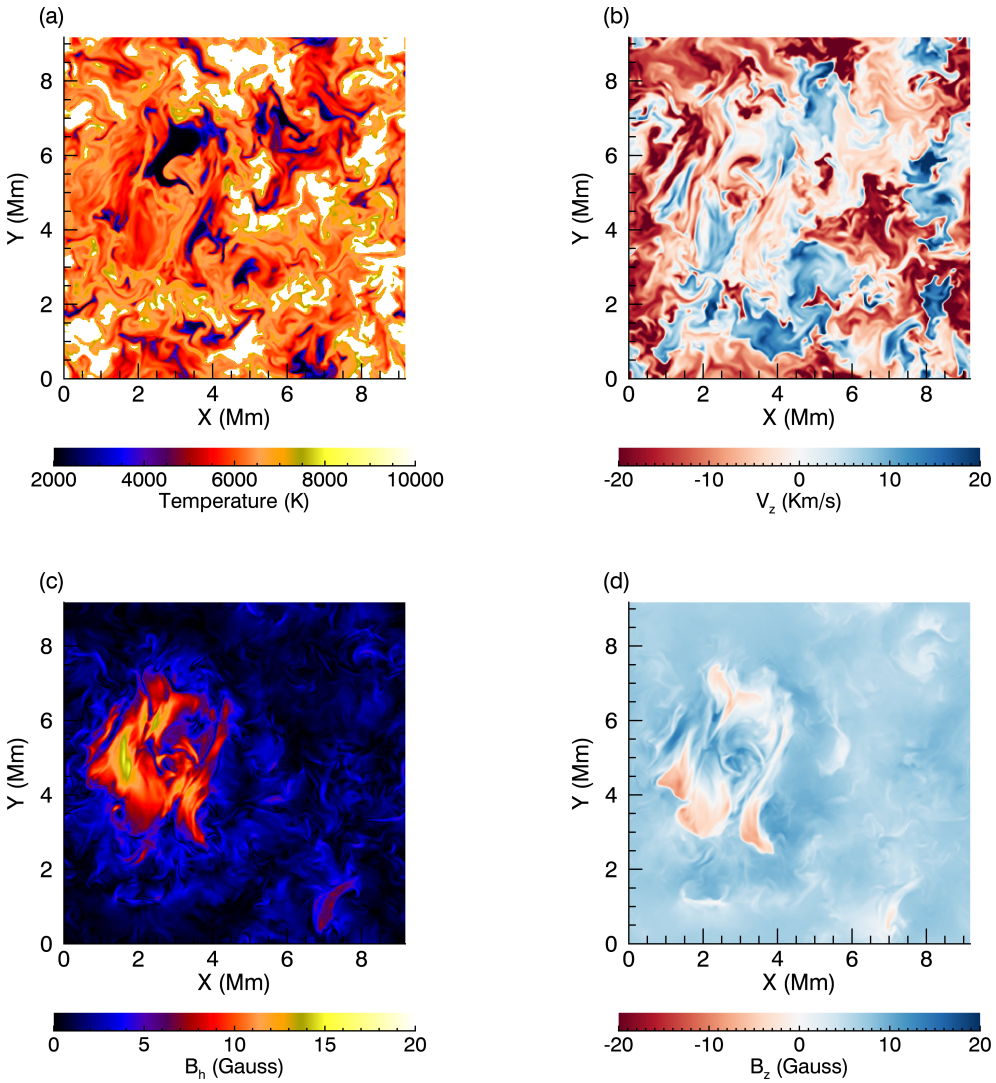

Figure 4.8: One snapshot of the distribution of (a): temperature, (b): vertical velocity, (c): horizontal magnetic field, and (d): vertical magnetic field at $z = 2.0$ Mm.

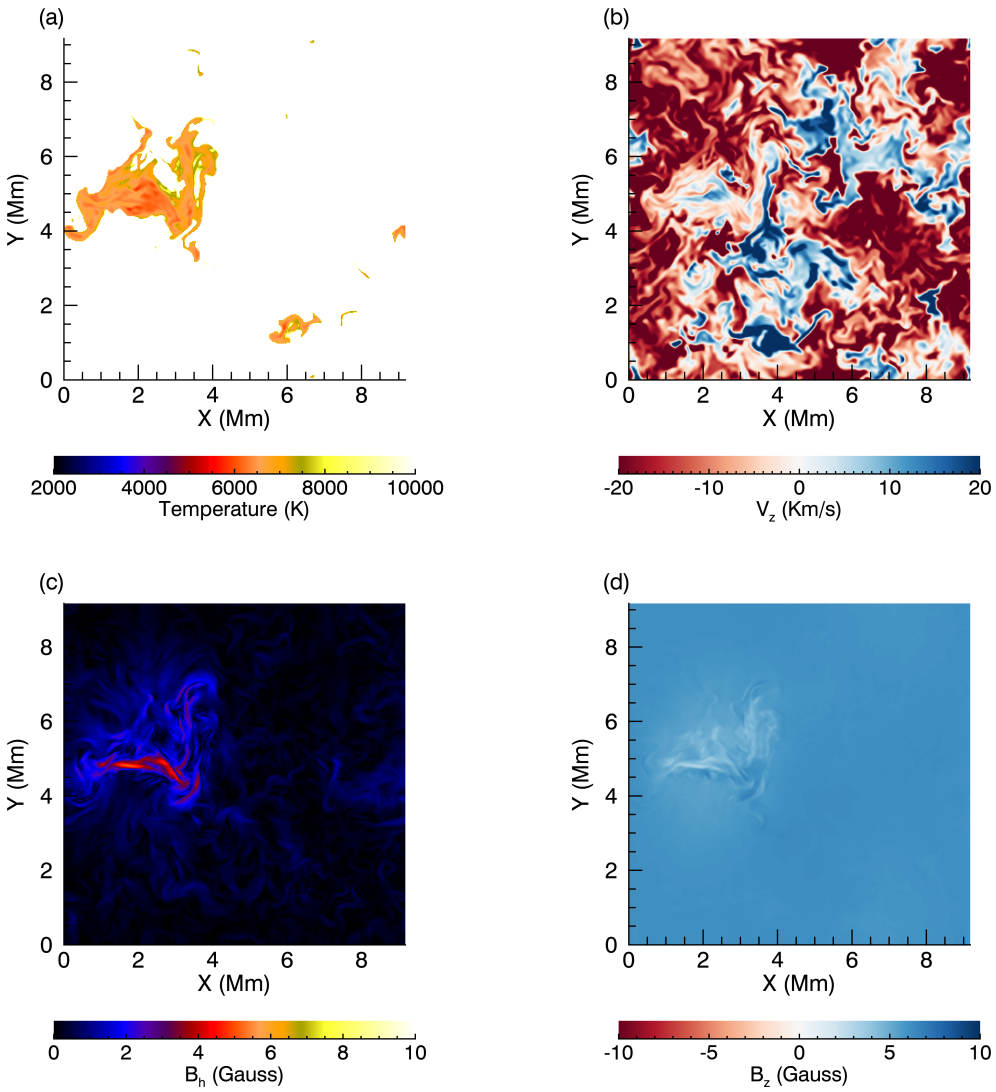

Figure 4.9: One snapshot of the distribution of (a): temperature, (b): vertical velocity, (c): horizontal magnetic field, and (d): vertical magnetic field at $z = 4.0$ Mm.

the vertical motion of spicules. If observed at a fixed position of this height, the dominant term in energy balance is the entropy term determined by the motion of spicules. As a result, we should not focus on the energy balance between heating and cooling at this height.

4.4 Discussion

First, we validate the simulation results by comparing our simulation with other observational and numerical studies. The distribution of vertical velocity of photospheric convection is shown by the solid line in Figure 4.14, where we compare our result with the result of MURaM (Vögler et al., 2005) simulation in Beeck et al. (2012) (dotted line in Figure 4.14). The difference between upflow and downflow can be clearly seen. The upflow in our study is weaker than that in MURaM simulation. We suggest that this difference could be caused by the position of measurement. In our simulation, the vertical velocity is picked up at the position where Rosseland mean opacity equals unity while in Beeck et al. (2012), the vertical velocity is picked up at the position where continuum opacity of 500 nm equals unity. As a result, the velocity of our study is picked up at a slightly higher position than that in MURaM simulation. This difference in position of measurement leads to a weaker upflow in our simulation. We also compare the distribution of root mean square of vertical velocity (Figure 4.15). The result shows a similar distribution between our study and MURaM simulation. The difference at a position higher than 0.5 Mm could be caused by the boundary effect of MURaM simulation since the top boundary of MURaM simulation is 1 Mm and the vertical velocity at the top boundary is zero.

Oba (2018) compares the MURaM simulation and observation. It is shown that the velocity histogram derived from synthesized spectra is consistent with that derived from Hinode observation (Figure 4.16). On the other hand, these histograms are different from

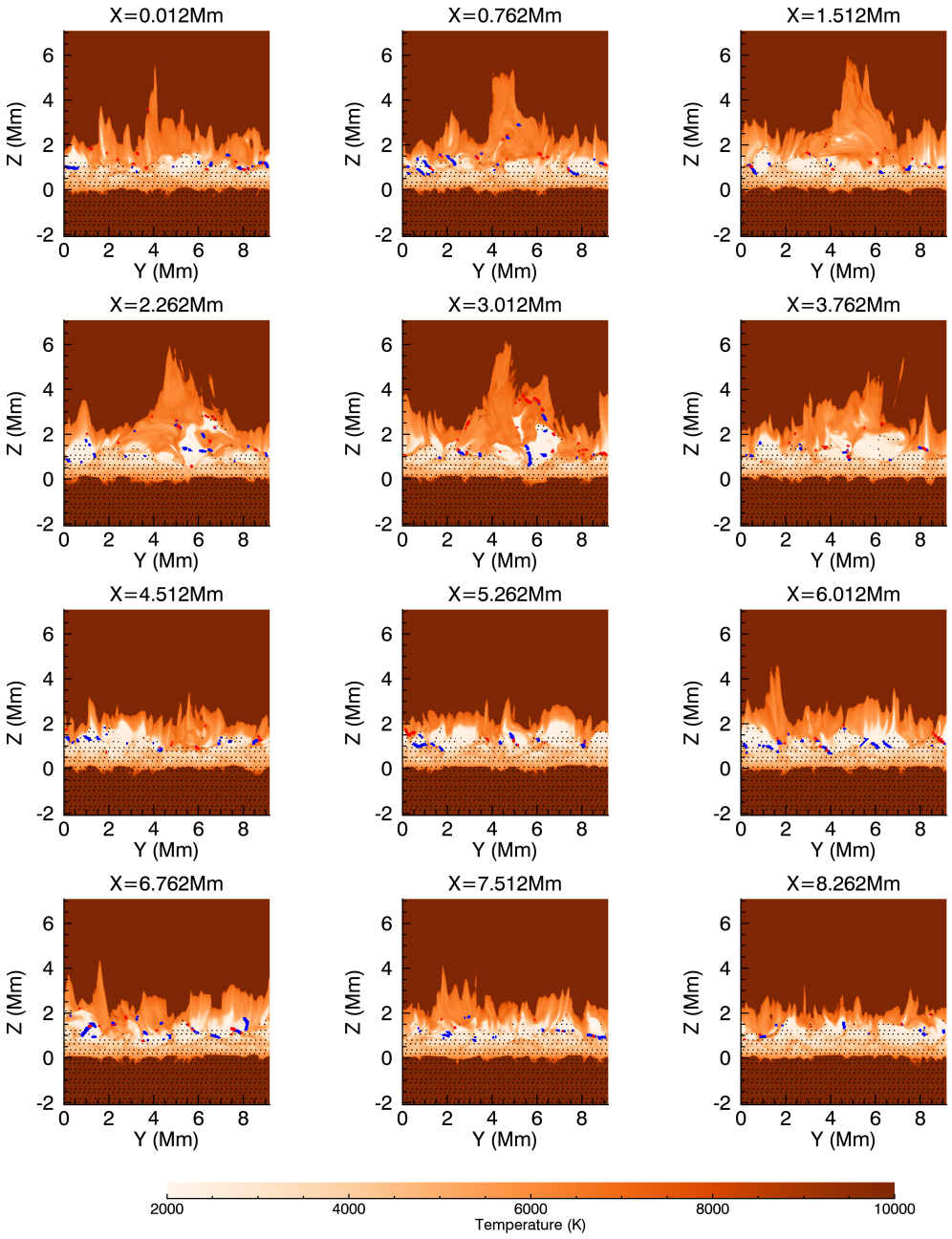

Figure 4.10: Snapshots of the simulation result of the y-z plane. The dotted shadow marks the region where sound speed is larger than Alfvén speed. The color shows the temperature. Fast and slow shocks are shown in blue and red color.

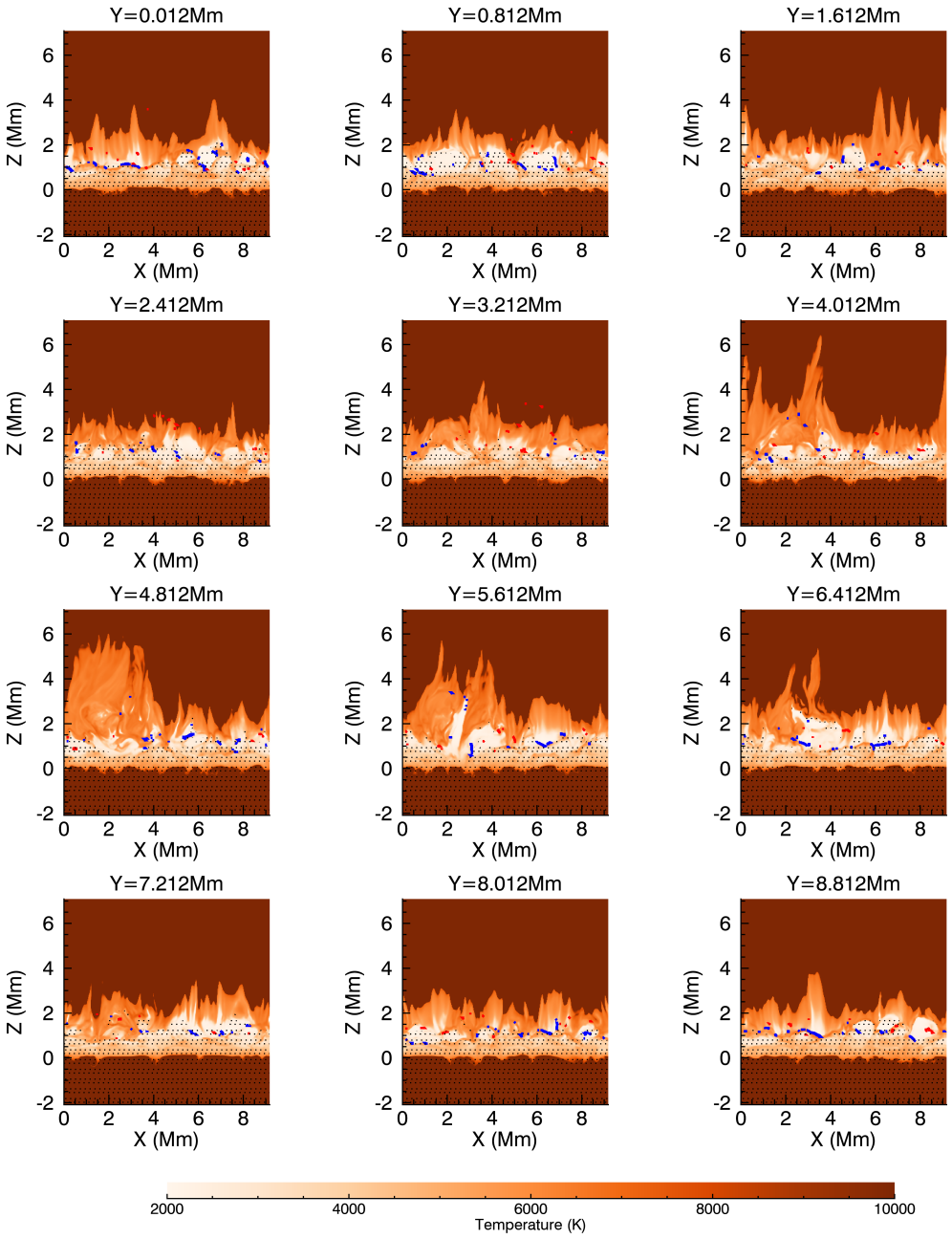

Figure 4.11: Snapshots of the simulation result of the x-z plane. The dotted shadow marks the region where sound speed is larger than Alfvén speed. The color shows the temperature. Fast and slow shocks are shown in blue and red color.

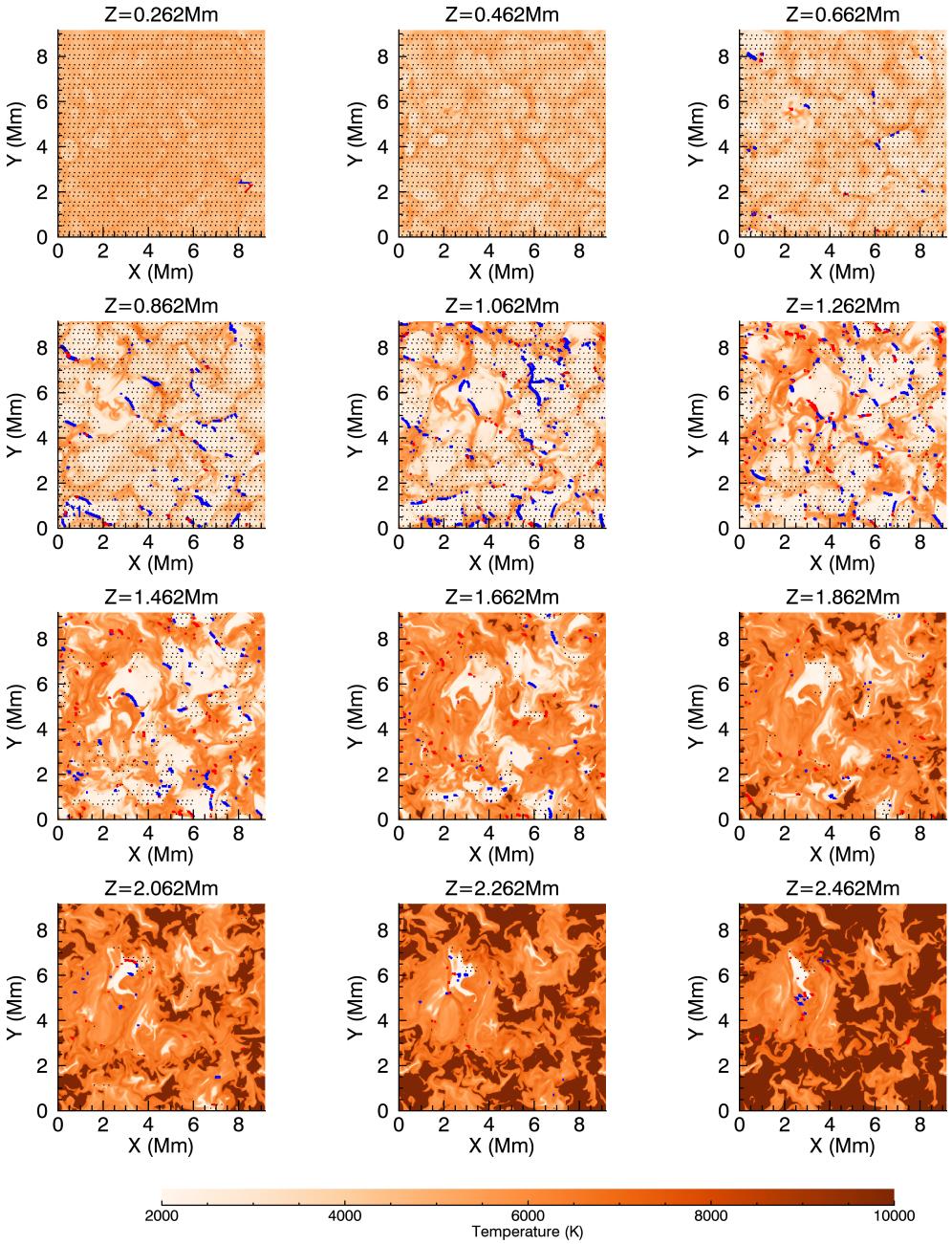

Figure 4.12: Snapshots of the simulation result of the x-y plane. The dotted shadow marks the region where sound speed is larger than Alfvén speed. The color shows the temperature. Fast and slow shocks are shown in blue and red color.

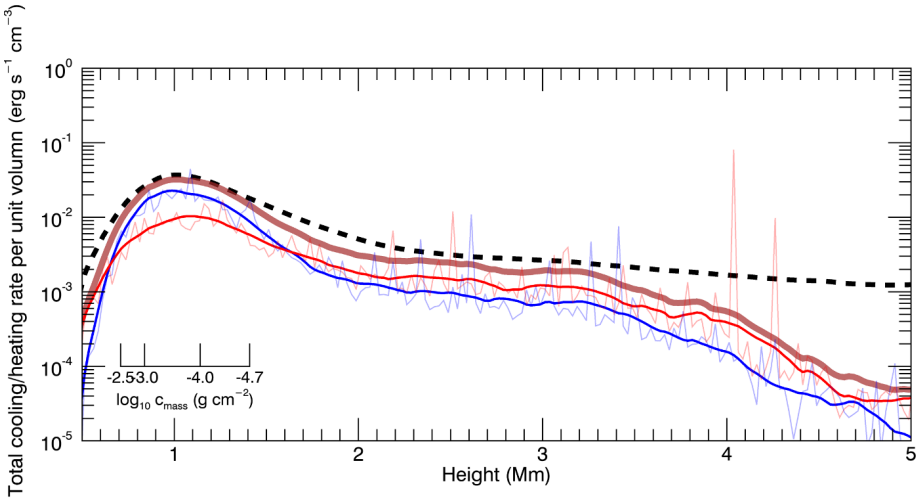

Figure 4.13: Heating and radiative loss rates of the low-beta chromospheric plasma as a function of height. The black dashed line is the total radiative loss rate in the simulation. The blue solid line is the fast wave heating rate in the low-beta region. The red solid line is the slow wave heating rate in the low-beta region. For blue and red lines, the thin lines with perturbation are the result directly calculated from the simulation while we also smooth the results by a Savitsky-Golay filter and plot them in thick lines. The brown solid line is the total heating rate that includes both fast wave and slow wave heating rate after smoothing. The averaged column mass at each height is shown in the secondary axis.

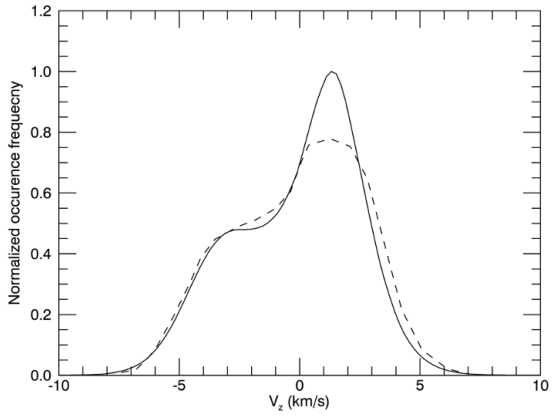

Figure 4.14: Solid line is the histogram of the vertical velocity of the photospheric convection in our study at the level where Rosseland mean opacity equals unity. Dotted line is the histogram of the vertical velocity in MURaM simulation (Beeck et al., 2012) at the level where continuum opacity of 500 nm equals unity.

those directly from the simulations without any synthesize procedure (Figure 4.14). Reasons for explaining this discrepancy are that the position of observation is higher than the level of Rosseland mean opacity (or continuum opacity) equals unity and the limited spatial resolution. As our simulation also has a similar velocity distribution with MURaM simulation, the consistency between our simulation and observation is also achieved.

As we are focusing on the wave heating mechanism, the frequency of the waves is crucial as it could affect the mode conversion, mode coupling, and the steepening of waves in the chromosphere. The waves are generated self-consistently by the convection motion through Lighthill mechanism (Lighthill, 1952). There is no guarantee that the spectra of waves generated in our simulation could reflect the real situation of the sun. Due to the limited range of the simulation box, current simulations can never self-consistently generate p-modes.

To evaluate the consistency of the frequency of the generated waves between our simulation and the observation, we plot the power spectra of the vertical velocity in Figure 4.17 with observed cut off frequency (Wiśniewska et al., 2016). The tendency that the fre-

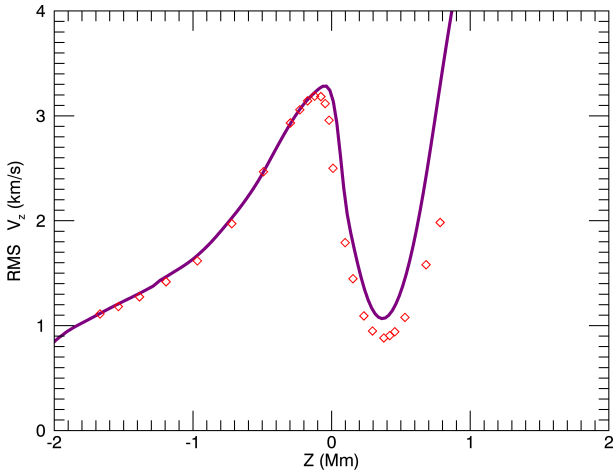

Figure 4.15: Solid purple line is root mean square of vertical velocity as a function of height in our simulation. Red diamonds mark the corresponding values in MURaM simulation (Beeck et al., 2012).

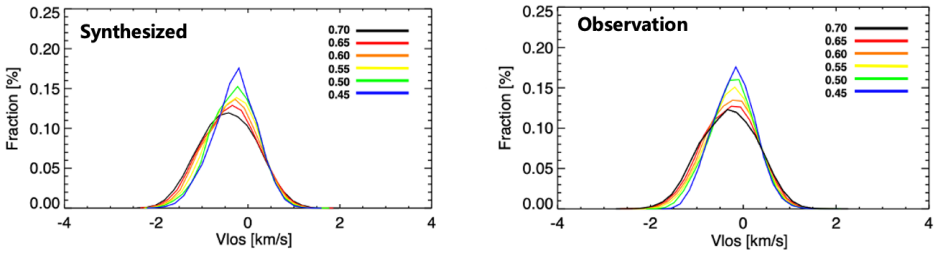

Figure 4.16: Histogram of the line of sight velocity derived from synthesized observation (left panel) and Hinode observation (right panel). Different colors represent different bisector levels that approximately correspond to different heights (from black to blue: 49 km, 62 km, 77 km, 92 km, 112 km, and 135 km). Modified from Figure 4.3 and 4.5 in Oba (2018).

quency of waves increases with height is consistent with the observation. Nevertheless, the frequency below the observed cut off frequency still has a significant part of power (50 percent). This could be caused by the inclined magnetic field lines. The vertical velocity spectra in the chromosphere observed by Mg II line (Kayshap et al., 2018) are also compared with the simulation. It is shown that the observed chromospheric velocity spectra are consistent with that in the simulation.

We also compare the vertical velocity power spectra at 237 km with Hinode Ca II H (approximately 247 km) observation (Carlsson et al., 2007). The result is shown in Figure 4.18. The observation is the intensity fluctuation which can not be directly compared with the velocity amplitude. Nevertheless, we can still qualitatively compare the power spectra. In observation, it is shown that the maximum power is at low frequencies, decreasing to 2.5 mHz and then increasing through a local maximum at 4-5 mHz before decreasing again. The simulation shows the same pattern.

On the other hand, the amplitude of the waves in the simulation is larger than observation. For example, the root mean square of the vertical velocity of the simulation at around 1.4 Mm (approximated formation height of Hα line core according to Vernazza et al., 1981) is around 6 km s^{-1}, which is larger than the observed Doppler shifts of Hα lines in the chromosphere of 0.8 - 2.3 km s^{-1} (Abbasvand et al., 2020b). It is reasonable that the observed Doppler shift is smaller than the velocity in the model because the emerging intensity includes the information along the line of sight. Although most of the photons come from the region where optical depth is close to unity, this region includes a considerable range of height. This effect has been discussed in Bello González et al. (2010) when measuring the photospheric acoustic flux. In the chromosphere, quantitative discussion requires synthesized observation, including the complicated treatment in solving NLTE radiative transfer equation, which is left as a future perspective.

The result of the three-dimensional simulation confirms our conclusion that the fast

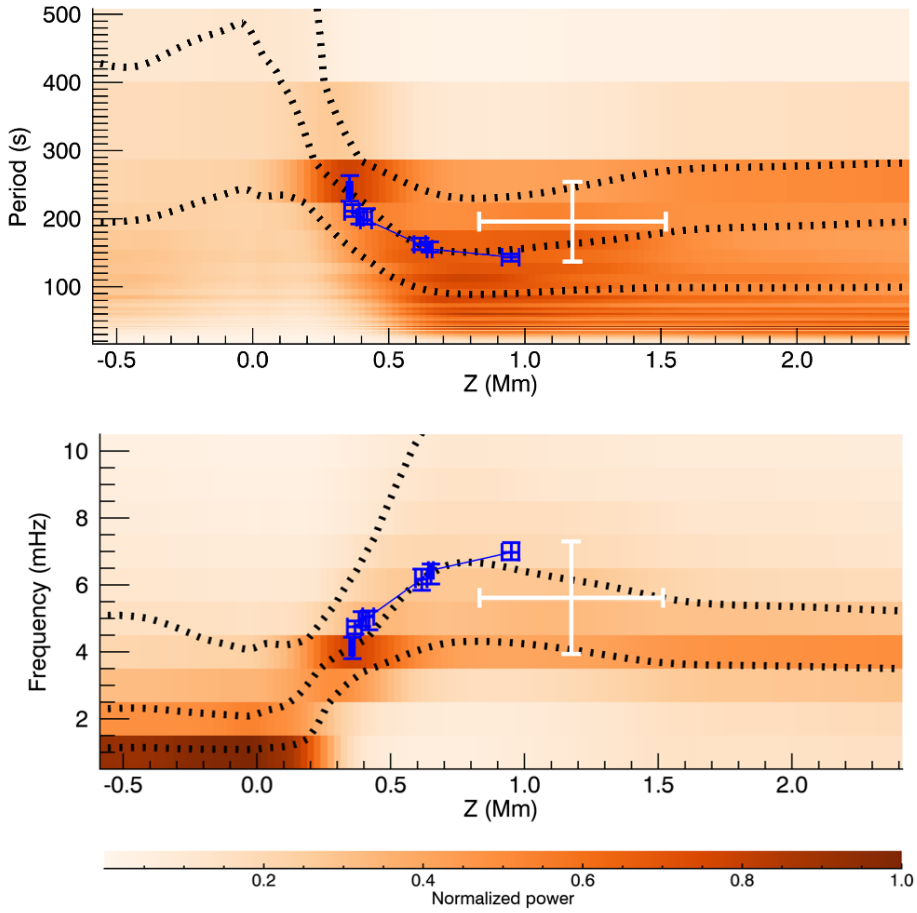

Figure 4.17: Power spectra of vertical velocity normalized at each height. The power spectra are displayed as a function of period (upper panel) and frequency (lower panel). The blue lines show the minimum detected height of different periods of waves by Wiśniewska et al. (2016). The chromospheric velocity power spectra observed by Mg II line (Kayshap et al., 2018) is also shown by the white color. Three dotted lines correspond to the level of 25 percent, 50 percent and 75 percent of total power, respectively, at each height.

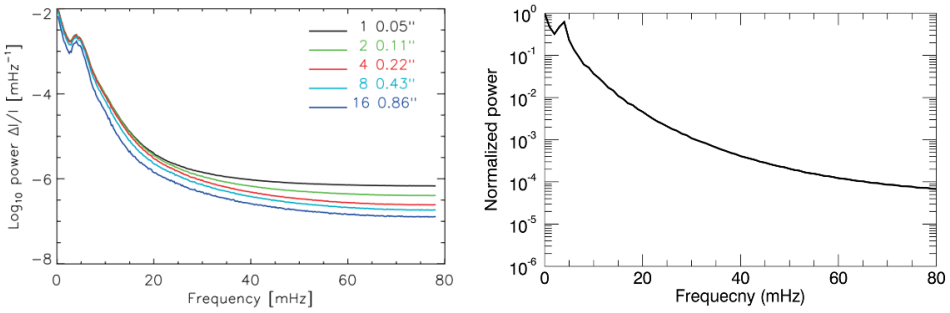

Figure 4.18: Left panel: power of intensity fluctuations as function of frequency observed by SOT/Broadband Filter Imager Ca II H filter time series at various spatial binnings (color code in the legend). The left panel is extracted from Figure 3 of Carlsson et al. (2007). Right panel: vertical velocity power spectra at 237 km in our study.

magnetic wave is significant in heating the low-beta chromosphere is still valid. There still remains a difference. In the three-dimensional simulation, the slow wave heating becomes larger than fast wave heating at the position where the height is larger than 1.6 Mm (Figure 4.13), which does not occur in the two-dimensional simulation (Figure 3.8). A stable flux tube forms at $(x, y) = (2.5, 5.5)$ Mm. The flux tube includes straighter magnetic field lines, which is in favor of mode transmission for the generation of the slow acoustic waves. Mode coupling from Alfvén wave to slow acoustic wave also plays a role in the flux tubes for the generation of slow acoustic waves. Moreover, according to the previous research (Iijima & Yokoyama, 2017), flux tube is associated with tall spicules in the three-dimensional simulation. As the fast wave propagates as an expanding sphere, only a small part of the fast magnetic wave could enter the spicules. As a result, the heating from slow waves has a larger share inside the tall spicules associated with the flux tube.

Compared with other studies of three-dimensional chromospheric simulation, our study focuses on analysing the modes of waves in detail in realistic three-dimensional simulation. Recent three-dimensional study in Matsumoto (2021) analyses the heating rate from different modes of waves by estimating the implicit numerical dissipation. However, as this study is focusing on the coronal region, the estimation of heating rate could

be less reliable because the total heating rate is approximately four times smaller than the radiative loss in the chromosphere, due to the numerical limitation of the reconstruction method. Besides, the generation of waves in Matsumoto (2021) is realized by including artificial volumetric force, which is different from our simulation.

Our simulation does not include the dynamic ionization of hydrogen and ambipolar diffusion. However, as discussed in Section 3.5.1, on average, the ambipolar diffusion does not significantly heat the chromosphere, especially in the region of our interest where the fast magnetic wave plays an important role in heating.

Chapter 5

Summary and general discussion

5.1 Summary of the results

We performed numerical simulations in studying the chromospheric heating mechanism. Our study focuses on shock heating. Shocks are identified by the threshold value of $\nabla \cdot \mathbf{V}$. The heating rate is calculated by the entropy jump between the upstream and the downstream regions of the shock. The mode of shock is identified by the relation between the gas pressure and the magnetic pressure across the shock front.

In Chapter 3, we introduce the results of the two-dimensional simulation. We find that the shock heating rate is balanced with the radiative cooling rate. The fast magnetic wave is significant in heating the low-beta chromosphere. We further investigate the generation mechanism and successfully identify the mode conversion from the fast acoustic wave to the fast magnetic wave at the region close to equipartition layer where the attacking angle is large. We also identify the mode transmission from fast acoustic wave to slow acoustic wave where the attacking angle is small. We investigate the result in an enhanced background magnetic field. The importance of fast magnetic wave in heating remains unchanged. However, the percentage of heating from slow acoustic wave becomes larger

at a higher position close to the transition region as the straighter magnetic field leads to a smaller attacking angle for waves propagating upwards, which is in favor of mode transmission and generation of the slow acoustic waves. Finally, we find that the fast wave could be possibly observed by the next generation solar telescopes indicated by the pattern of vertical stripes in the time slice of the vertical magnetic field.

In Chapter 4, we validate the result in the three-dimensional simulation. The fast magnetic wave still plays a significant role in heating the chromosphere. On the other hand, the difference from the two-dimensional simulation is that the slow wave becomes dominant in heating at a higher position. This is interpreted as a consequence of the magnetic structure: A stable magnetic flux tube forms in the three-dimensional simulation. Tall spicules form in the flux tube. The effect of spicules and the straighter magnetic field lines in the flux tube are in favor of mode transmission for the generation of slow acoustic waves. In addition, non-linear mode coupling from Alfvén wave to slow acoustic wave also presences in the three-dimensional geometry, which is in favor of generation of the slow acoustic wave in the flux tube. To investigate the consistency between the simulation and observation, we calculate the power spectra of the vertical velocity. It is suggested that the power spectra of the vertical velocity in the simulation are consistent with the observation.

5.2 General discussion

5.2.1 Uniqueness of this study

There are two new points in our study. The first point is that we study the propagation of waves in detail by identification of different modes of waves and calculate the shock heating rate in realistic simulation. The other point is that we propose that fast magnetic wave

is important for heating the low-beta chromospheric plasma. Although the generation of the fast wave in the low-beta region has been well discussed in the previous studies (e.g. Hasan & van Ballegooijen, 2008), they do not investigate the contribution to heating by fast magnetic waves quantitatively.

5.2.2 Proposed picture on heating mechanisms in the chromosphere

Combining the results in our study and previous studies, the current understanding of chromospheric heating is shown in the cartoon in Figure 5.1. From the last century, the acoustic shock is considered to heat the chromosphere (e.g. Schwarzschild, 1948; Osterbrock, 1961; Anderson & Athay, 1989b; Jordan, 1993), which is further confirmed by the consistency between the observation and synthesized observation from the simulation results (Carlsson & Stein, 1997). Inside the low-beta flux tube, slow acoustic wave generated from mode coupling could contribute to heating, which has been studied by recent numerical simulations (e.g. Arber et al., 2016; Brady & Arber, 2016; Wang & Yokoyama, 2020). There are also observational attempts trying to catch the signal of mode coupling (McAteer et al., 2003; Bloomfield et al., 2004). At the top part of the chromosphere that is close to the transition region, inside the spicules, or in the strong flux tube, the role of magnetic field becomes more important with decreasing of plasma beta. In these regions, dissipation of small structures, generated from Alfvén wave turbulence (van Ballegooijen et al., 2011) or phase mixing (Soler et al., 2019) could contribute to heating, where ambipolar diffusion (Khomenko et al., 2018, 2020) could play an important role in dissipation of the magnetic energy. The contribution of our study is the chromospheric heating in the medium part of the chromosphere, which includes the low-beta plasma above the magnetic canopy but not so close to the transition region (typically 10^{-5} g cm$^{-2} < c_{\rm mass} < 10^{-3}$ g cm^{-2}). In this region, the fast magnetic wave is significant to heating.

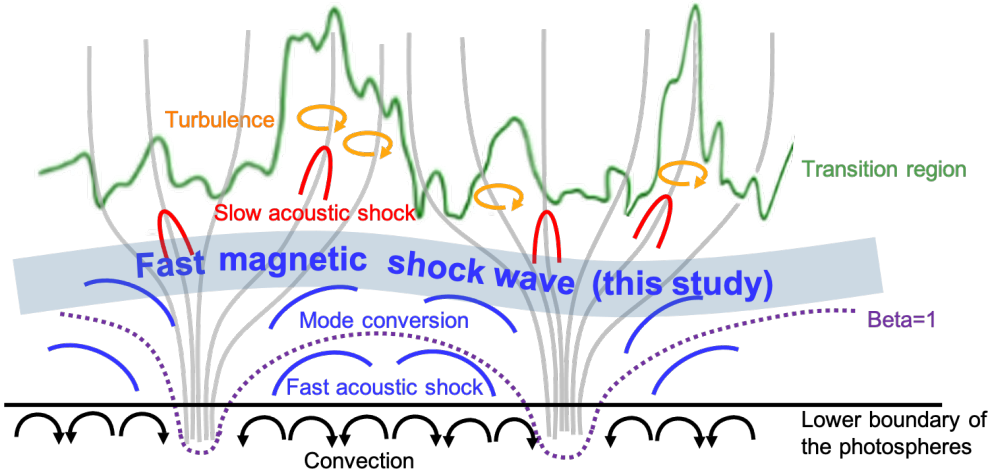

Figure 5.1: Schematic plot of the chromospheric heating mechanisms.

5.2.3 Limitation of the simulations in this study

Dynamic ionization of hydrogen and ambipolar diffusion are not explicitly included in both two-dimensional and three-dimensional simulations. Leenaarts et al. (2007) compare simulations with LTE assumption and dynamic ionization. It is shown that shock temperatures with dynamic ionization are higher and the intershock temperatures are lower than the simulation with LTE assumption. This effect could affect the measurement of entropy jump. In addition, dynamic ionization is important to determine the electron and the ion number density. The diffusivity of ambipolar diffusion is sensitive to the number density of ions, especially when the ionization degree is low. It is shown in the two-dimensional simulation that on average, the ambipolar diffusion does not considerably heat the chromosphere. However, the diffusivity changes drastically in the chromosphere depending on the dynamic change of the magnetic fields and ionization degrees. The ambipolar diffusion could become effective and affect the chromospheric dynamics locally. The ambipolar diffusion works effectively in two typical regions. The first one is the cool bubble after the shock fronts and the other is at a higher position close to the transition region or inside the spicules. One example of the ambipolar diffusion related generation of spicules

is shown in Martínez-Sykora et al. (2017). Our model can not reproduce the dynamics of the regions where the ambipolar diffusion is effective.

5.3 Future perspective

The magnetic field is critical in the chromospheric dynamics by affecting the mode conversion, non-linear mode coupling, and ambipolar diffusion. It could be interesting to compare the heating rate in regions with different magnetic field structures. This could be done by extending the simulation box to include more flux tubes and more complicated magnetic field structures as well as by changing the intensity of the background magnetic field.

Ambipolar diffusion is not explicitly included in the current study. One important next step for the development of the simulation code is to implement the non-equilibrium ionization of hydrogen ionization and the ambipolar diffusion. After the implementation, we could quantitatively discuss the heating rate of ambipolar diffusion.

It is interesting to connect the chromosphere and the corona to self-consistently solve the atmospheric heating problem. The influence from the chromosphere to the corona is obvious because waves that propagate in the corona come from the lower part of the atmosphere. On the other hand, there is feedback from the corona to the chromospheric dynamics. For example, Iijima & Yokoyama (2015) show that the corona temperature determines the heights of the spicules.

Chapter 6

Concluding remarks

We perform two-dimensional and three-dimensional realistic MHD simulations from the convection zone to the corona with local thermodynamic equilibrium radiative transfer in the photosphere and approximated chromospheric and coronal radiative loss. From the simulation results, we identify the shocks by filtering the regions with large negative divergence of velocity. After the identification of shocks, we separate fast and slow MHD waves by identifying the relation between magnetic pressure and gas pressure across the shock front. We further calculate the contribution to chromospheric heating through the measurement of entropy jump. Our results of both two-dimensional and three-dimensional simulations show that the shock heating rate is consistent with the radiative loss rate in the chromosphere. Fast magnetic waves play an important role in heating the low-beta chromosphere.

References

Abbasvand, V., Sobotka, M., Heinzel, P., et al. 2020a, ApJ, 890, 22, doi: 10.3847/1538-4357/ab665f

Abbasvand, V., Sobotka, M., Švanda, M., et al. 2020b, A&A, 642, A52, doi: 10.1051/0004-6361/202038559

Anderson, L. S., & Athay, R. G. 1989a, ApJ, 346, 1010, doi: 10.1086/168083

—. 1989b, ApJ, 336, 1089, doi: 10.1086/167078

Arber, T. D., Brady, C. S., & Shelyag, S. 2016, ApJ, 817, 94, doi: 10.3847/0004-637X/817/2/94

Avrett, E. H. 1965, SAO Special Report, 174, 101

Avrett, E. H. 1981, in NATO Advanced Science Institutes (ASI) Series C, Vol. 68, NATO Advanced Science Institutes (ASI) Series C, ed. R. M. Bonnet & A. K. Dupree, 173–198

Beeck, B., Collet, R., Steffen, M., et al. 2012, A&A, 539, A121, doi: 10.1051/0004-6361/201118252

Bello González, N., Franz, M., Martínez Pillet, V., et al. 2010, ApJL, 723, L134, doi: 10.1088/2041-8205/723/2/L134

Bellot Rubio, L., & Orozco Suárez, D. 2019, Living Reviews in Solar Physics, 16, 1, doi: 10.1007/s41116-018-0017-1

Bloomfield, D. S., McAteer, R. T. J., Mathioudakis, M., Williams, D. R., & Keenan, F. P. 2004, ApJ, 604, 936, doi: 10.1086/382062

Bogdan, T. J., Carlsson, M., Hansteen, V. H., et al. 2003, ApJ, 599, 626, doi: 10.1086/378512

Brady, C. S., & Arber, T. D. 2016, ApJ, 829, 80, doi: 10.3847/0004-637X/829/2/80

Bruls, J. H. M. J., Vollmöller, P., & Schüssler, M. 1999, A&A, 348, 233

Cally, P. S. 2006, Philosophical Transactions of the Royal Society of London Series A, 364, 333, doi: 10.1098/rsta.2005.1702

—. 2009, SoPh, 254, 241, doi: 10.1007/s11207-008-9290-9

Carlsson, M., De Pontieu, B., & Hansteen, V. H. 2019, ARA&A, 57, 189, doi: 10.1146/annurev-astro-081817-052044

Carlsson, M., Hansteen, V. H., Gudiksen, B. V., Leenaarts, J., & De Pontieu, B. 2016, A&A, 585, A4, doi: 10.1051/0004-6361/201527226

Carlsson, M., & Leenaarts, J. 2012, A&A, 539, A39, doi: 10.1051/0004-6361/201118366

Carlsson, M., & Stein, R. F. 1994, in Chromospheric Dynamics, ed. M. Carlsson, 47

Carlsson, M., & Stein, R. F. 1995, ApJL, 440, L29, doi: 10.1086/187753

—. 1997, ApJ, 481, 500, doi: 10.1086/304043

—. 2002, ApJ, 572, 626, doi: 10.1086/340293

Carlsson, M., Hansteen, V. H., de Pontieu, B., et al. 2007, PASJ, 59, S663, doi: 10.1093/pasj/59.sp3.S663

Cavallini, F. 2006, SoPh, 236, 415, doi: 10.1007/s11207-006-0103-8

Christensen-Dalsgaard, J., Dappen, W., Ajukov, S. V., et al. 1996, Science, 272, 1286, doi: 10.1126/science.272.5266.1286

de la Cruz Rodríguez, J., De Pontieu, B., Carlsson, M., & Rouppe van der Voort, L. H. M. 2013, ApJL, 764, L11, doi: 10.1088/2041-8205/764/1/L11

De Pontieu, B., McIntosh, S. W., Carlsson, M., et al. 2007, Science, 318, 1574, doi: 10.1126/science.1151747

De Pontieu, B., Title, A. M., Lemen, J. R., et al. 2014, SoPh, 289, 2733, doi: 10.1007/s11207-014-0485-y

Deng, Y., Liu, Z., & CGST Group. 2012, in Astronomical Society of the Pacific Conference Series, Vol. 463, Second ATST-EAST Meeting: Magnetic Fields from the Photosphere to the Corona., ed. T. R. Rimmele, A. Tritschler, F. Wöger, M. Collados Vera, H. Socas-Navarro, R. Schlichenmaier, M. Carlsson, T. Berger, A. Cadavid, P. R. Gilbert, P. R. Goode, & M. Knölker, 405

Deng, Y. Y., & CGST Group. 2011, in Astronomical Society of India Conference Series, Vol. 2, Astronomical Society of India Conference Series, 31–36

Domingo, V., Fleck, B., & Poland, A. I. 1995, SoPh, 162, 1, doi: 10.1007/BF00733425

Fawzy, D. E. 2010, NewA, 15, 717, doi: 10.1016/j.newast.2010.05.007

Fawzy, D. E., Ulmschneider, P., & Cuntz, M. 1998, A&A, 336, 1029

Fedun, V., Shelyag, S., & Erdélyi, R. 2011, ApJ, 727, 17, doi: 10.1088/0004-637X/727/1/17

Fossum, A., & Carlsson, M. 2005, Nature, 435, 919, doi: 10.1038/nature03695

Gabriel, A. H. 1976, Philosophical Transactions of the Royal Society of London Series A, 281, 339, doi: 10.1098/rsta.1976.0031

Golding, T. P., Leenaarts, J., & Carlsson, M. 2016, ApJ, 817, 125, doi: 10.3847/0004-637X/817/2/125

Gošić, M., de la Cruz Rodríguez, J., De Pontieu, B., et al. 2018, ApJ, 857, 48, doi: 10.3847/1538-4357/aab1f0

Gudiksen, B. V., Carlsson, M., Hansteen, V. H., et al. 2011, A&A, 531, A154, doi: 10.1051/0004-6361/201116520

Handy, B. N., Acton, L. W., Kankelborg, C. C., et al. 1999, SoPh, 187, 229, doi: 10.1023/A:1005166902804

Hasan, S. S., & van Ballegooijen, A. A. 2008, ApJ, 680, 1542, doi: 10.1086/587773

Hollweg, J. V., Jackson, S., & Galloway, D. 1982, SoPh, 75, 35, doi: 10.1007/BF00153458

Iglesias, C. A., & Rogers, F. J. 1996, ApJ, 464, 943, doi: 10.1086/177381

Iijima, H. 2016, PhD thesis, Department of Earth and Planetary Science, School of Science, The University of Tokyo, Japan, doi: 10.5281/zenodo.55411

Iijima, H., & Yokoyama, T. 2015, ApJL, 812, L30, doi: 10.1088/2041-8205/812/2/L30

—. 2017, ApJ, 848, 38, doi: 10.3847/1538-4357/aa8ad1

Jess, D. B., Mathioudakis, M., Erdélyi, R., et al. 2009, Science, 323, 1582, doi: 10.1126/science.1168680

Jordan, S. D. 1993, ApJ, 414, 337, doi: 10.1086/173080

Kayshap, P., Murawski, K., Srivastava, A. K., Musielak, Z. E., & Dwivedi, B. N. 2018, MNRAS, 479, 5512, doi: 10.1093/mnras/sty1861

Khomenko, E., & Collados, M. 2012, ApJ, 747, 87, doi: 10.1088/0004-637X/747/2/87

Khomenko, E., Collados, M., Vitas, N., & Gonzalez-Morales, P. A. 2020, arXiv e-prints, arXiv:2009.09753. https://arxiv.org/abs/2009.09753

Khomenko, E., Vitas, N., Collados, M., & de Vicente, A. 2018, A&A, 618, A87, doi: 10.1051/0004-6361/201833048

Kosugi, T., Matsuzaki, K., Sakao, T., et al. 2007, SoPh, 243, 3, doi: 10.1007/s11207-007-9014-6

Kurucz, R. L. 1970, SAO Special Report, 309

Landi, E., & Landini, M. 1999, A&A, 347, 401

Leenaarts, J., Carlsson, M., Hansteen, V., & Rutten, R. J. 2007, A&A, 473, 625, doi: 10.1051/0004-6361:20078161

Leenaarts, J., Pereira, T. M. D., Carlsson, M., Uitenbroek, H., & De Pontieu, B. 2013, ApJ, 772, 90, doi: 10.1088/0004-637X/772/2/90

Lemen, J. R., Title, A. M., Akin, D. J., et al. 2012, SoPh, 275, 17, doi: 10.1007/s11207-011-9776-8

Lighthill, M. J. 1952, Proceedings of the Royal Society of London Series A, 211, 564, doi: 10.1098/rspa.1952.0060

Lin, H.-H., & Carlsson, M. 2015, ApJ, 813, 34, doi: 10.1088/0004-637X/813/1/34

Martínez Pillet, V., Del Toro Iniesta, J. C., Álvarez-Herrero, A., et al. 2011, SoPh, 268, 57, doi: 10.1007/s11207-010-9644-y

Martínez-Sykora, J., De Pontieu, B., & Hansteen, V. 2012, ApJ, 753, 161, doi: 10.1088/0004-637X/753/2/161

Martínez-Sykora, J., De Pontieu, B., Hansteen, V. H., et al. 2017, Science, 356, 1269, doi: 10.1126/science.aah5412

Matsumoto, T. 2021, MNRAS, 500, 4779, doi: 10.1093/mnras/staa3533

Matsumoto, T., & Shibata, K. 2010, ApJ, 710, 1857, doi: 10.1088/0004-637X/710/2/1857

Matthews, S. A., Collados, M., Mathioudakis, M., & Erdelyi, R. 2016, in procspie, Vol. 9908, Ground-based and Airborne Instrumentation for Astronomy VI, 990809, doi: 10.1117/12.2234145

McAteer, R. T. J., Gallagher, P. T., Williams, D. R., et al. 2003, ApJ, 587, 806, doi: 10.1086/368304

McIntosh, S. W., de Pontieu, B., Carlsson, M., et al. 2011, Nature Communications, 475, 477, doi: 10.1038/nature10235

Morton, R. J., Verth, G., Jess, D. B., et al. 2012, Nature Communications, 3, 1315, doi: 10.1038/ncomms2324

Oba, T. 2018, PhD thesis, Department of Space and Astronautical Science, School of Physical sciences, SOKENDAI (The Graduate University for Advanced Studies), Japan

Osterbrock, D. E. 1961, ApJ, 134, 347, doi: 10.1086/147165

Pennicott, J. D., & Cally, P. S. 2019, ApJL, 881, L21, doi: 10.3847/2041-8213/ab3423

Pesnell, W. D., Thompson, B. J., & Chamberlin, P. C. 2012, SoPh, 275, 3, doi: 10.1007/s11207-011-9841-3

Rathore, B., Carlsson, M., Leenaarts, J., & De Pontieu, B. 2015, ApJ, 811, 81, doi: 10.1088/0004-637X/811/2/81

Rimmele, T. R., Warner, M., Keil, S. L., et al. 2020, SoPh, 295, 172, doi: 10.1007/s11207-020-01736-7

Roberts, W. O. 1945, ApJ, 101, 136, doi: 10.1086/144699

Sadykov, V. M., Kitiashvili, I. N., Kosovichev, A. G., & Wray, A. A. 2020, arXiv e-prints, arXiv:2008.05995. https://arxiv.org/abs/2008.05995

Sánchez Almeida, J. 2004, in Astronomical Society of the Pacific Conference Series, Vol. 325, The Solar-B Mission and the Forefront of Solar Physics, ed. T. Sakurai & T. Sekii, 115. https://arxiv.org/abs/astro-ph/0404053

Scherrer, P. H., Bogart, R. S., Bush, R. I., et al. 1995, SoPh, 162, 129, doi: 10.1007/BF00733429

Scherrer, P. H., Schou, J., Bush, R. I., et al. 2012, SoPh, 275, 207, doi: 10.1007/s11207-011-9834-2

Schwarzschild, M. 1948, ApJ, 107, 1, doi: 10.1086/144983

Sobotka, M., Heinzel, P., Švanda, M., et al. 2016, ApJ, 826, 49, doi: 10.3847/0004-637X/826/1/49

Soler, R., Terradas, J., Oliver, R., & Ballester, J. L. 2019, ApJ, 871, 3, doi: 10.3847/1538-4357/aaf64c

Sterling, A. C. 2000, SoPh, 196, 79, doi: 10.1023/A:1005213923962

Tian, H., DeLuca, E. E., Cranmer, S. R., et al. 2014, Science, 346, 1255711, doi: 10.1126/science.1255711

Tritschler, A., Rimmele, T. R., Berukoff, S., et al. 2015, in Cambridge Workshop on Cool Stars, Stellar Systems, and the Sun, Vol. 18, 18th Cambridge Workshop on Cool Stars, Stellar Systems, and the Sun, ed. G. T. van Belle & H. C. Harris, 933–944

Tsiropoula, G., Tziotziou, K., Kontogiannis, I., et al. 2012, Space Sci. Rev., 169, 181, doi: 10.1007/s11214-012-9920-2

Tsuneta, S., Ichimoto, K., Katsukawa, Y., et al. 2008, SoPh, 249, 167, doi: 10.1007/s11207-008-9174-z

Ulmschneider, P., & Kalkofen, W. 2003, Heating of the solar chromosphere, ed. B. N. Dwivedi & F. b. E. N. Parker, 181–195

Ulmschneider, P., & Stein, R. F. 1982, A&A, 106, 9

Ulmschneider, P., Zaehringer, K., & Musielak, Z. E. 1991, A&A, 241, 625

van Ballegooijen, A. A., Asgari-Targhi, M., Cranmer, S. R., & DeLuca, E. E. 2011, ApJ, 736, 3, doi: 10.1088/0004-637X/736/1/3

Vardya, M. S. 1965, MNRAS, 129, 205, doi: 10.1093/mnras/129.2.205

Vernazza, J. E., Avrett, E. H., & Loeser, R. 1981, ApJS, 45, 635, doi: 10.1086/190731

Vögler, A., Shelyag, S., Schüssler, M., et al. 2005, A&A, 429, 335, doi: 10.1051/0004-6361:20041507

Wang, Y., & Yokoyama, T. 2020, ApJ, 891, 110, doi: 10.3847/1538-4357/ab70b2

Wiegelmann, T., Thalmann, J. K., & Solanki, S. K. 2014, A&A Rv, 22, 78, doi: 10.1007/s00159-014-0078-7

Wiśniewska, A., Musielak, Z. E., Staiger, J., & Roth, M. 2016, ApJL, 819, L23, doi: 10.3847/2041-8205/819/2/L23

Withbroe, G. L., & Noyes, R. W. 1977, ARA&A, 15, 363, doi: 10.1146/annurev.aa.15.090177.002051